UC San Diego
UC San Diego Electronic Theses and Dissertations

Title
Strongly correlated electron systems in uranium-based compounds

Permalink
https://escholarship.org/uc/item/95w4q8tw

Author
Kanchanavatee, Noravee

Publication Date
2012

Peer reviewed|Thesis/dissertation

eScholarship.org Powered by the California Digital Library
University of California

UNIVERSITY OF CALIFORNIA, SAN DIEGO

Strongly Correlated Electron Systems in Uranium-based Compounds

A dissertation submitted in partial satisfaction of the
requirements for the degree
Doctor of Philosophy

in

Physics

by

Noravee Kanchanavatee

Committee in charge:

Professor M. Brian Maple, Chair
Professor Renkun Chen
Professor Sunil Sinha
Professor William Trogler
Professor Congjun Wu

2012

Copyright
Noravee Kanchanavatee, 2012
All rights reserved.

The dissertation of Noravee Kanchanavatee is approved, and it is acceptable in quality and form for publication on microfilm and electronically:

Chair

University of California, San Diego

2012

DEDICATION

To my parents, who always support me no matter what.

TABLE OF CONTENTS

LIST OF FIGURES

ACKNOWLEDGEMENTS

Many people have contributed to my Ph.D. dissertation. First and foremost, I am grateful to my advisor, prof. Brian Maple for his suggestions and supports throughout my academic program. I really appreciate the assistance from every member in the group. I would like to thank: Marc Janochek for teaching me about x-ray diffraction, specific heat measurements, helping me write my first paper; James Hamlin for teaching me to use the SQUID magnetometer and Cpt. America, and how to do data analysis; Ryan Bambauch for helping me start up in the lab and for useful discussions about research; Diego Zocco for teaching me about resistivity measurements; Lei Shu for conducting specific heat measurements with the Dynacool; Ben White for performing resistivity and specific heat measurements with the Dynacool; Ben Taylor for advice on the SQUID; Kevin Huang for teaching me how to use the arc furnace, which became very useful for my project; Ivy Lum for helping me in sample preparation; Colin McElroy for running Cpt. America; Duygu, Sooyoung and Yoonho for always cheering me up; Eileen for giving me training on quartz bench. I also would like to thank all of my Thai friends in San Diego for their friendship.

A portion of the text and data presented in chapter 3 are reprints of material that appears in “Evolution of the magnetic and superconducting states in UCoGe With Fe and Ni substitution”, J. J. Hamlin, R. E. Baumbach, K. Huang, M. Janoschek, N. Kanchanavatee, D. A. Zocco, and M. B. Maple, Mater. Res. Soc. Symp. Proc. 1264, 1264-Z12-04 (2010). The dissertation author was a co-author of the article.

A portion of the text and data presented in chapter 4 are reprints of material that appears in “Two-fold enhancement of the “hidden order”/large moment antiferromagnetic phase boundary in the $URu_{2-x}Fe_xSi_2$ system”, N. Kanchanavatee, M. Janoschek, R. E. Baumbach, J. J. Hamlin, D. A. Zocco, K. Huang, and M. B. Maple, Phys. Rev. B 84, 245122 (2011). The dissertation author was the first author of the article.

A portion of the text and data presented in chapter 5 are reprints of material that appears in “Enhancement of hidden order transition temperature in the $URu_{2-x}Os_xSi_2$ system”, N. Kanchanavatee and M. B. Maple in preparation. The dissertation author is the first author of the article.

VITA

2006	B. S. in Physics *cum laude*, Chulalongkorn University, Bangkok, Thailand
2007-2011	Teaching Assistant, Department of Physics, University of California, San Diego
2011-2012	Research Assistant, Department of Physics, University of California, San Diego
2012	Ph. D. in Physics, University of California, San Diego

PUBLICATIONS

J. J. Hamlin, R. E. Baumbach, K. Huang, M. Janoschek, N. Kanchanavatee, D. A. Zocco, and M. B. Maple, “Evolution of the magnetic and superconducting states in UCoGe with Fe and Ni substitution”, Mater. Res. Soc. Symp. Proc. 1264, 1264-Z12-04 (2010).

N. Kanchanavatee, M. Janoschek, R. E. Baumbach, J. J. Hamlin, D. A. Zocco, K. Huang, and M. B. Maple, “Two-fold enhancement of the “hidden order”/large moment antiferromagnetic phase boundary in the $URu_{2-x}Fe_xSi_2$ system”, Phys. Rev. B 84, 245122 (2011).

FIELDS OF STUDY

Major Field: Physics

Studies in strongly correlated electron materials

M. Brian Maple, Bernd T. Matthias Professor of Physics,

University of California, San Diego

ABSTRACT OF THE DISSERTATION

Strongly Correlated Electron Systems in Uranium-based Compounds

by

Noravee Kanchanavatee

Doctor of Philosophy in Physics

University of California, San Diego, 2012

Professor M. Brian Maple, Chair

The properties of UCoGe and $\mathrm{URu_2Si_2}$ have been investigated by substitution of Ni into the Co site and Fe and Os into the Ru site. Polycrystalline samples of $\mathrm{UCo_{1-x}Ni_xGe}$ $(0 \leq x \leq 1)$, $\mathrm{URu_{2-x}Fe_xSi_2}$ $(0 \leq x \leq 2)$, and $\mathrm{URu_{2-x}Os_xSi_2}$ $(0 \leq x \leq 1.2)$ were prepared by arc-melting and studied by x-ray diffraction, energy dispersive x-ray spectroscopy, electrical resistivity, specific heat, and magnetization measurements. In the $\mathrm{UCo_{1-x}Ni_xGe}$ system, the material evolves from the ferromagnetic state to the antiferromagnetic state with increasing Ni concentration. The superconducting state is destroyed by small amounts of Ni substitution and does not appear to re-emerge in any other portion of the phase diagram. Measurements on $\mathrm{URu_{2-x}Fe_xSi_2}$ reveal a two-fold enhancement of the “hidden order” (HO)/large moment antiferromagnetic (LMAFM) phase boundary $T_0(x)$. The $T_0(P_{ch})$ curve, obtained by converting x

to “chemical pressure” P_{ch}, is strikingly similar to the $T_0(P)$ curve, where P is applied pressure, for URu_2Si_2 $-$ both exhibit a “kink” at 1.5 GPa and a maximum at $\sim$ 7 GPa. This similarity suggests that the HO-LMAFM transition at 1.5 GPa in URu_2Si_2 occurs at $x \approx$ 0.2 ($P_{ch} \approx$ 1.5 GPa) in $URu_{2-x}Fe_xSi_2$. The transition temperature in $URu_{2-x}Os_xSi_2$ is enhanced from 17.5 K at $x = 0$ to 50 K at $x = 1$. At $x \approx 0.2$, the samples seem to evolve to another ordered phase as indicated by the decreasing size of the HO gap.

Chapter 1

Introduction

1.1 Energy bands in metals

In metals, the valence electrons become conduction electrons traveling through the lattice. The allowed energies of those itinerant electrons form a band of energy levels referred to as energy bands. At $T = 0$, the states within the energy band are occupied by electrons in increasing order of energy, and in a metal, there are only enough valence electrons to partially fill the conduction band. Since there are many empty states available, the electrons with the highest energy level (called the Fermi level, E_F) respond to low-energy thermal and electrical excitations as if they were a gas of free particles.

Fig. 1.1 illustrates the formation of energy bands in solids. When two atoms are brought together to form a diatomic molecule, their wave functions overlap. The single atomic energy level splits into two new states, one lower in energy and one higher in energy. The lowered state, which is the sum of the two atomic wave functions, is called a bonding state because occupying it lowers the energy and stabilizes the system, while the raised state, which is the difference between those wave functions, is called an antibonding state because occupying it raises the energy and destabilizes the system. Similarly, when more atoms are brought together to form a crystal, the number of energy levels increases, and the levels evolve into a band of bonding and antibonding states. Although the energy levels remain discrete, the number of levels is so large and the spacing between them is so small that it is useful to consider the energy as a continuous

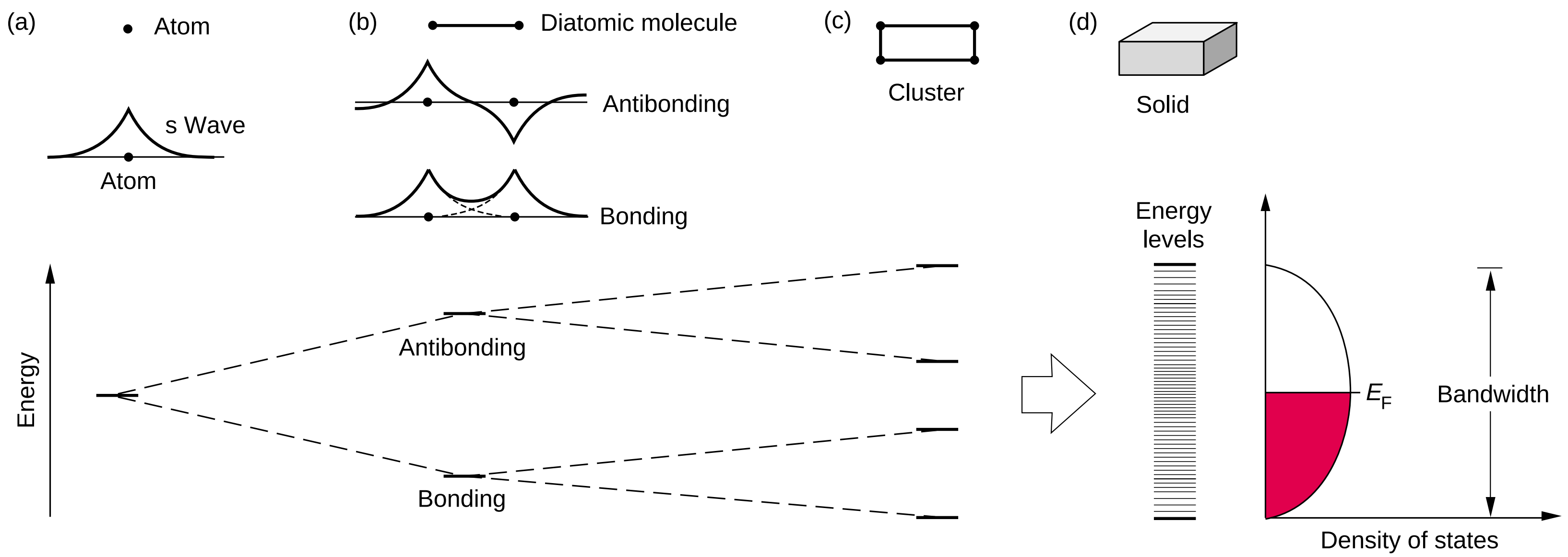

Figure 1.1: (a) The radial wave function and the energy level for a $1s$ valence electron in an isolated atom. (b) When two such atoms are brought together, their s-electron wave functions will hybridize to form the bonding and antibonding orbitals of a diatomic molecule. The bonding orbital is the sum of the two atomic wave functions, whereas the antibonding orbital is the difference between them. The original energy level has split into two: The lower level is the energy of the bonding orbital, and the upper, the energy of the antibonding orbital. As shown in (c), the energy levels split again when four atoms are brought together to form a cluster, and again they correspond to bonding and antibonding states. When a very large number of atoms are brought together into a solid (d), their energy levels form a closely spaced band corresponding to both the bonding and the antibonding states. Note that the width of the energy band is about equal to the difference between the bonding and antibonding energy levels in the diatomic molecule. The levels in the energy band are so tightly packed can be considered to be a continuous variable and the levels are enumerated in terms of a density of states function. The shaded region represents the occupied levels at $T = 0$, that is, all levels are occupied up to the Fermi level, E_F. From [1].

variable and describe the number of energy levels per unit energy in terms of a density of states at a given energy.

The width of the energy band is proportional to the amount of overlap of the two atomic wave function. The smaller the interatomic distance, the larger the overlap of the wave functions and the wider the bandwidth. Also, the s and p bands are always wider than the d band, which is always wider than the f band [2].

1.2 Nature of actinide metals

Uranium belongs to a group called actinides, metals that have $5f$ valence electrons. Actinide metal bondings can be divided into two different behaviors, localized and itinerant [4, 5]. In the localized picture, the $5f$ electrons have little or no effect on bonding whereas in itinerant picture, they strongly participate in bonding. Fig. 1.2 shows similarity of actinide ($5f$) series to the transition metal ($5d$) series and the rare earth ($4f$) series. Since electrons fill energy bands in order of increasing energy, the bonding states are filled increasing the bonding and decreasing the size of the atom, then the antibonding states are filled inducing the opposite impact on the atomic size. Thus, a parabolic-like behavior is indicative of itinerant nature of the $5d$ metal. In the $4f$ metals, the atomic radii are rather constant because the $4f$ electrons are localized. Exceptions in the rare-earth series are Eu and Yb, since they are divalent and thus have a larger volume. The actinide metals exhibit both behaviors, a parabolic-like decrease in the first half of the series, and a constant behavior in the other half. This can also be understood in terms of the bandwidth. Transition metals are more itinerant than the actinides because the bandwidth of the d band is wider than that of the f band. Furthermore, since the wave function of $4f$ electrons has less radial extent than that of the $5f$ electrons, it becomes more difficult to overlap and form a band, hence the rare earths are more localized. In the first half of the actinide series, the $5f$ electrons still forms a band while in the second half the Coulomb forces have become strong enough to localize the f electrons, leaving the spd electrons to glue atoms together. Note that, as can be seen in Fig. 1.2, the Wigner-Seitz radius of U compared to nearby elements is almost intermediate between metallic and atomic behavior.

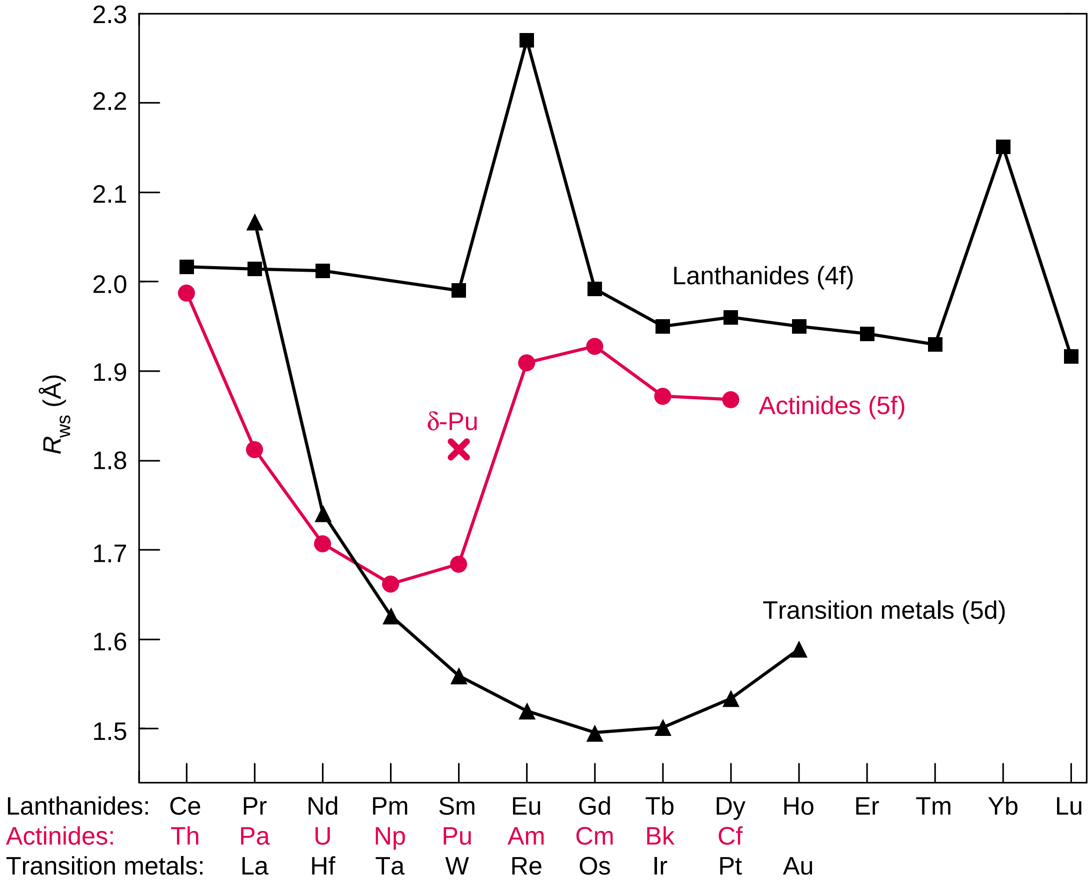

Figure 1.2: Wigner-Seitz radius of each metal as a function of atomic number for the $5d$, $4f$, and $5f$ metal series. From [1, 2, 3, 4].

Several elements have their electrons precariously balanced between itinerant and localized states. A rearranged periodic table, which contains only d and f electron elements is shown in Fig. 1.3. Metals in this table can be separated into two categories. One where electrons are itinerant and tend to exhibit superconductivity as the ground state, and the other one where electrons are localized, usually forming a magnetic ground state at low temperatures. The diagonal white band indicates where electrons transition from itinerant to localized. Thus, metals in this white band can be easily tuned via temperature, pressure, magnetic field, or chemical substitutions. Note that U also lies in the border between itinerant and localized wave functions.

The idea that the degree of overlap of the f-electron wave functions between neighboring atoms determines whether a compound is localized (magnetic) or itinerant (superconducting) is illustrated in Fig. 1.4. Most compounds behave as predicted. The superconducting compounds occur at short spacings, while the magnetic compounds appear at large spacings. However, there are a few exceptions, such as UPt_3 and UBe_{13}. This is due to the hybridization of localized d- or f-electron and conduction electron states in compounds containing transition metal, lanthanide, or actinide ions with partially-filled d- or f-electron shells (Fig. 1.5).

Across the actinide series, U is one of the most interesting elements. It is on the border between localization and itineracy (Fig 1.3). The Wigner-Seitz radius of U is almost exactly in the middle between a localized $5f$ wave function and an itinerant $5f$ wave function. Moreover, the energy bands of s, p, d and f electrons of U can hybridize with each other. Thus, U is a weakly radioactive element that can be tuned with pressure, field, or chemical substitutions to produce novel electronic ground states such as heavy fermion behavior, unconventional superconductivity, or hidden order.

1.3 Kondo effect

When a small amount of magnetic impurities are dissolved in a non-magnetic host, a minimum in electrical resistivity as a function of temperature is sometimes observed. At high temperatures, the magnetic moments of the impurities behave like free paramagnetic moments, but below a characteristic temperature T_K, the interaction between impurity moments and the conduction electrons screen the moments through an antiferromagnetic exchange interaction, resulting in the impurity spin becoming nonmagnetic. This process of magnetic screening is known as the “Kondo effect” [8]. An enhancement of resistivity at low temperatures is also due to this interaction since it strongly enhances the electron cross-section.

1.4 Heavy fermions

Heavy fermion compounds are metallic materials in which conduction electrons behave as if they had extremely heavy masses. The electron effective mass, which can be estimated from the electronic specific heat coefficient γ_0, in heavy fermion compounds can be hundreds of times larger than that in normal metals. Several relations can be utilized to characterize materials as heavy fermion compounds. For example, the Wilson-Sommerfeld scaling ratio [9],

$$R = \frac{\pi^2 k_B^2 \chi_0}{\mu_{eff}^2 \gamma_0} \tag{1.1}$$

where χ_0 is the magnetic susceptibility at zero temperature, and μ_{eff} is the effective magnetic moment. The ratio R is usually on the order of unity for heavy fermion materials. Another useful ratio is the Kadowaki-Woods relation [10],

$$\frac{A}{\gamma_0^2} = 10^{-5}\ \mu\Omega\mathrm{cm}\frac{\mathrm{molK}^2}{\mathrm{mJ}}, \tag{1.2}$$

where A is the coeffient of the T^2 term in resistivity from an equation,

$$\rho(T) = \rho_0 + AT^2. \tag{1.3}$$

At high temperatures, heavy fermion compounds behave like systems with localized magnetic moments obeying the Curie-Weiss law while, at low temperatures, the magnetic susceptibility becomes temperature independent. The electrical resistivity not only exhibits a local minimum, it also goes through a broad hump at $\approx$ 50-100 K, and then decreases rapidly with decreasing temperature to a regime where it acts like a conventional metal or varies as T^2, indicative of electron-electron scattering. These phenomena are typically elucidated as an extension of the single-ion Kondo effect with small concentrations of magnetic impurities to the case of a lattice of magnetic impurities, "Kondo lattice". At high temperatures, the highly-concentrated magnetic ions act as independent local moments, while at lower temperatures the conduction electrons screen the magnetic moments, inducing a non-magnetic ground state and large electron effective masses. Since the formation of these electron clouds enhance scattering, the screening can be observed as an increase in electrical resistivity with decreasing temperature. However, in heavy fermion systems, the moments are not impurities so the electron clouds are formed symmetrically across the lattice leading to phase coherence and a rapid drop in resistivity below a coherence temperature T_{coh}.

1.5 Superconductivity

Superconductivity was first discovered in 1911 when H. Kamerlingh Onnes cooled a mercury wire with liquid helium and found that the electrical resistivity of the mercury wire dropped abruptly to an immeasurably small value below a certain temperature, 4.2 K [11]. This temperature is now called the superconducting critical temperature, T_{sc}. Soon after the initial discovery, Onnes found an upper limit for the current that would flow in superconducting state. This is known as the critical current, I_c. He also found superconductivity in lead and tin, and that the I_c of a superconducting coil was lower than that of a superconducting wire. This was shortly understood after he discovered that a magnetic field in excess of a certain value, H_c, forces superconductors back to the normal state. Above T_{sc}, the resistivity acts as a normal metal. The resistivity becomes zero; i.e., perfect DC conductivity below T_{sc}. In fact, zero resistance is not accessible to direct measurement. The impossibility still remains for measurement of the inverse quantity, conductivity, since no technique is available to measure infinity. However, zero resistance can be inferred from experiments using a magnetic field to induce electrical currents. The currents have been observed to flow without decay for more than a year [12]. The decay time of such currents is calculated to be of the order of 100,000 years. For AC, superconductors behave as normal conductors at high frequency, and superconducting transition appears at low frequency. This suggests that there may be a gap between energy levels. Experiments of optical transmission on superconducting films of lead and tin indicated that the gap width is on order 4 k_BT_{sc} [13]. For many years after the discovery of superconductivity, scientists believed that zero electrical resistivity is the only difference from normal metals. It was not until Meissner and Ochsenfeld found, in 1933, that magnetic flux is expelled from the specimen cooled below critical temperature, leading to vanishing magnetic field inside except for a very thin layer, the thickness of which is called the penetration depth, that the assumption was shattered. This phenomenon is called the "Meissner effect". Since there is no magnetic field inside of superconductors, the susceptibility has the ideal value of a perfect diamagnet. At low temperature, the thermal conductivity of a superconductor is much lower than that of same metal in the normal state. Below T_{sc}, the specific heat rises to a higher value and then slowly decreases to below the value of a normal metal. The linear term of the normal state is replaced by an exponential term, exp($-\Delta/k_BT$), which is characteristic of a system with an energy gap. It was also observed that the transition into the superconducting state involves no latent heat; thus, the gap width must depend on temperature and must reach zero as T approaches T_{sc} [13]. In 1950, an important discovery that the isotopic mass influences the critical temperature was made. In the so-called "isotope effect", T_{sc} is proportional to $M^{-1/2}$, where M is isotopic mass [13]. This suggested that phonons may be involved in the mechanism of superconductivity.

The phenomenon of superconductivity in a conventional superconducting material is accurately explained by the Bardeen-Cooper-Schrieffer (BCS) theory [14]. In a simplified model, as an electron moves through a lattice, if the ion cores are not infinitely heavy, they will be pulled toward the electron, creating a region with excess positive charge. Another nearby electron is attracted by this region, which creates a Cooper pair. The amount of energy required to take two electrons from paired states to unpaired or normal states is equal to the energy gap. Zero DC resistance is a result of sufficient binding energy in a Cooper pair to prevent breaking of the pair by scattering. However, at high temperatures, thermal energy will cause some electrond in Cooper pairs to be unpaired, and thus a transition back to a normal conductor will occur. The achievements of the theory include

- The gap at 0 K is 3.5 $k_B T_{sc}$ which is of the same order as that found in experiments.
- The gap approaches zero as T approach T_{sc}.
- The temperature dependence and magnitude of the critical magnetic field agree very well with experiments.
- The magnitude and temperature dependence of the penetration depth are in agreement with experimental data.

It is significant to note that the BCS theory explains the properties of superconductivity arising from Cooper pairs, regardless of the pairing mechanisms.

The advent of heavy fermion superconductors in the 1980s [15] enhanced the interest and development of the field. There are also many new phenomena to investigate as well as the need for novel theories, since several properties of these materials cannot be elucidated by the BCS theory [16]. Thus, superconductivity in these novel materials is known as unconventional superconductivity. The heavy fermion superconductors have attracted a great deal of attention as it is the heavy quasiparticles that contribute to the superconductivity. Coexistence of magnetism and superconductivity is unanticipated in conventional superconductors. It was expected that magnetic interactions of electrons would break the Cooper pairs and suppress superconductivity. This means that the pairing mechanism in heavy fermion superconductors is probably not driven by the electron-phonon interactions.

1.6 Hidden order

The term "hidden order" (HO) phase was adopted for the exotic phase in the heavy fermion compound $\mathrm{URu_2Si_2}$ that occurs below $T_0 = 17.5$ K and coexists with superconductivity below $T_{sc} = 1.5$ K.[17, 18, 19] The specific-heat anomaly that accompanies the HO phase transition is reminiscent of a second order BCS-like mean field transition that opens a gap $\Delta \approx 130$ K over about 40 % of the Fermi surface(FS) due to a charge or spin density wave.[18] However, the small antiferromagnetic magnetic moment of only ~ 0.03 μ_B/U derived from neutron scattering experiments [20, 21] cannot account for the entropy of $\sim 0.2\mathrm{R}\ln(2)$ associated with the specific-heat anomaly [20]. The magnetization measurement exhibits a maximum at 60 K indicating the coherence temperature and the formation of a heavy fermion phase. The HO transition can be identified as a change in slope, which also occurs at 17.5 K [17]. The magnetization of $\mathrm{URu_2Si_2}$ is not reminiscent of that of a conventional bulk antiferromagnet [7]. In resistivity measurement, the onset of lattice coherence can be seen as a maximum at around 75 K, and the HO transition is visible as a small but sharp peak at 17.5 K [18]. Thermal expansion experiments which track the lattice constants a and c reveal an increase of volume at the HO transition, indicating that the HO is coupled to the lattice [22]. With the application of pressure, the magnetic structure in the HO phase was found to be identical to that of a larger moment antiferromagnetic (LMAFM) phase that emerges at critical pressures $P_c \geq$ 0.5-1.5 GPa [23]. It is widely accepted that the magnetic structure in the HO phase is due to a small amount of LMAFM phase induced by strain [21]. Far-infrared reflectance measurements confirm that the FS is being reconstructed at the HO transition [24]. The opening of the gap in the HO phase was affirmed by point-contact spectroscopy (PCS) measurements [25, 26, 27, 28]. However, the pressure exerted to drive the point contact causes a shift in the HO transition temperature [27]. More evidence of FS gap opening was found in thermal heat conductivity experiments [29, 30]. Quantum oscillations in both de Haas-van Alphen (dHvA) and Shubnikov de Haas (SdH) techniques were studied in order to probe the FS in the HO phase. To date five FS pockets have been revealed from these measurements [31, 32, 33].

After nearly three decades of intense research, the nature of HO and its order parameter (OP) have remained a mystery.

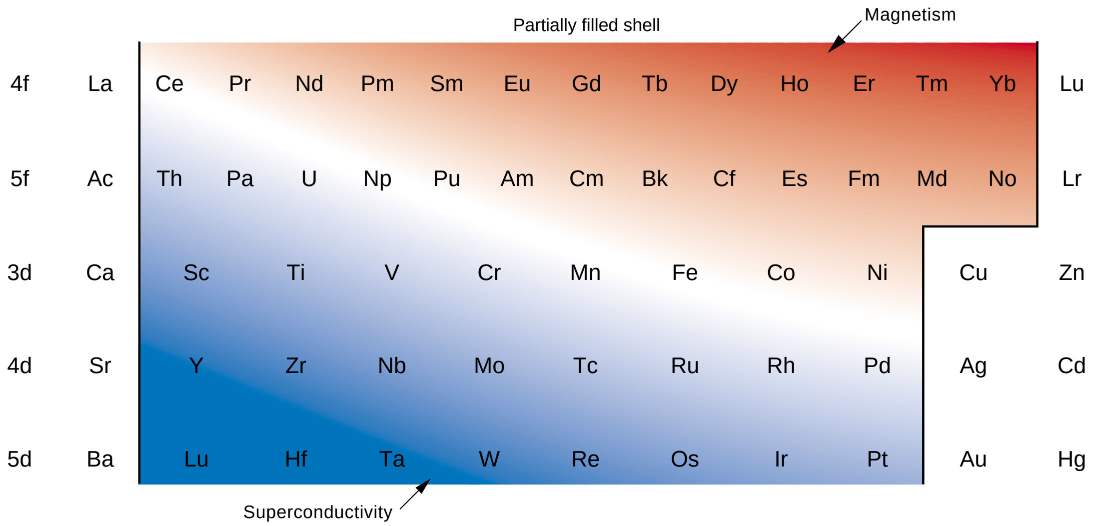

4f	La	Ce	Pr	Nd	Pm	Sm	Eu	Gd	Tb	Dy	Ho	Er	Tm	Yb	Lu
5f	Ac	Th	Pa	U	Np	Pu	Am	Cm	Bk	Cf	Es	Fm	Md	No	Lr
3d	Ca	Sc	Ti	V	Cr	Mn	Fe	Co	Ni	Cu	Zn				
4d	Sr	Y	Zr	Nb	Mo	Tc	Ru	Rh	Pd	Ag	Cd				
5d	Ba	Lu	Hf	Ta	W	Re	Os	Ir	Pt	Au	Hg				

Figure 1.3: The periodic table is rearranged with the rare-earth, or lanthanide, elements in the top row, the actinides in the second row, and the d-electron transition elements below them. Most metals have predictable ground states and become superconducting (blue) or magnetic (red) as the temperature is lowered. But the low-temperature metallic properties of the elements along the diagonal are difficult to explain because, in the solid-state, their f or d valence electrons are poised between localization and itinerancy. From [2, 4, 6].

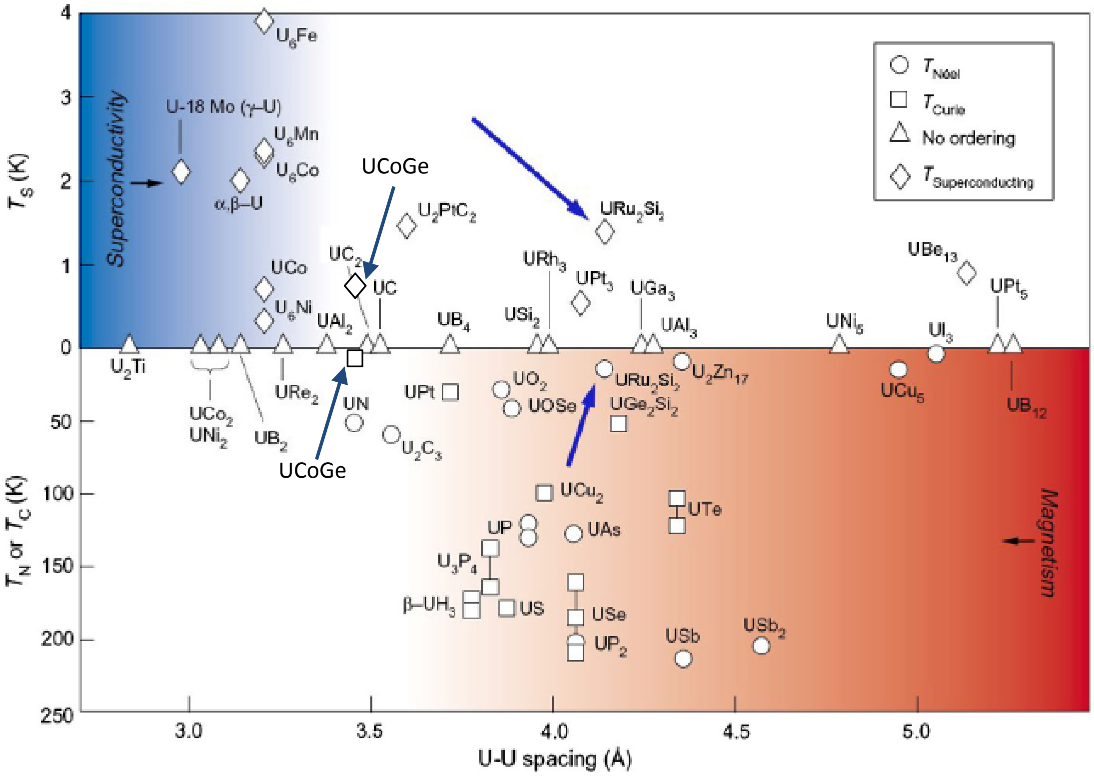

Figure 1.4: A Hill plot for a large number of U compounds. The superconducting T_{sc} or magnetic ordering T_N or T_C temperature for each compound plotted as a function of U-U interatomic distance. The transition from superconductivity to magnetism occurs around 3.5 Å, with only a few exceptions. From [7].

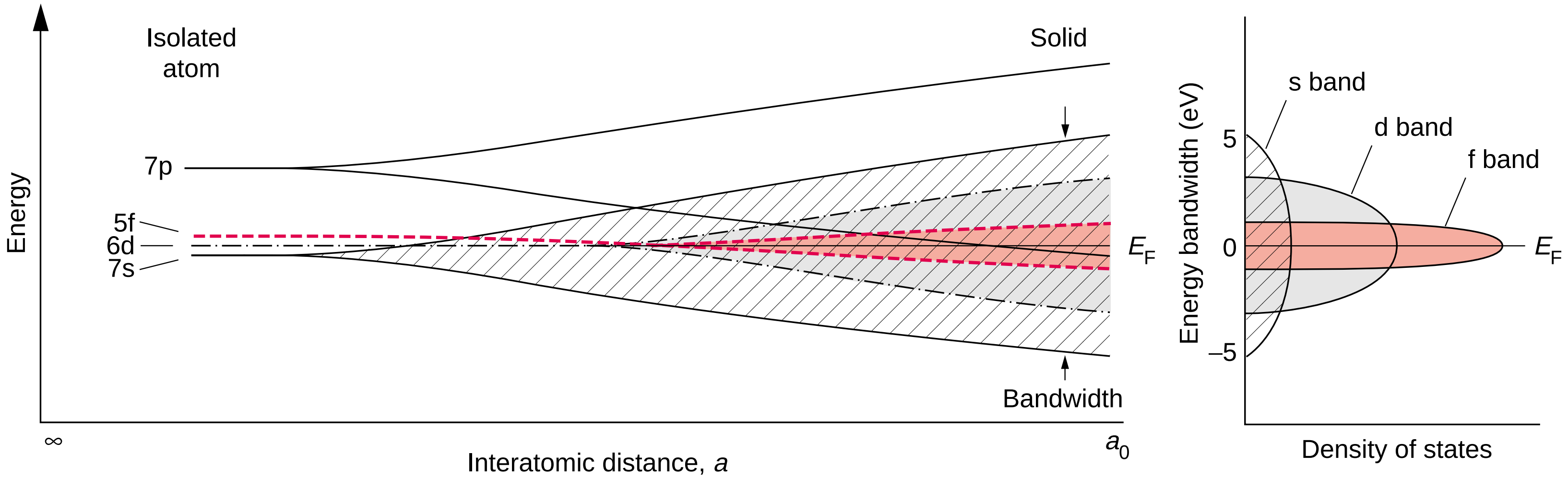

Figure 1.5: Illustrated here are the multiple energy bands that form in going from a single actinide atom to a solid. Multiple bands always form when an atom has more than one valence electron. Note that the s and p bands are much wider than the d band, which is much wider than the f band. Also, because the s, p, d, and f states overlap in energy, they can hybridize with each other. From [1].

Chapter 2

Experimental details

2.1 Sample preparation

Polycrystalline samples of $\mathrm{UCo}_{1-x}\mathrm{Ni}_x\mathrm{Ge}$ $(0 \leq x \leq 1)$, $\mathrm{URu}_{2-x}\mathrm{Fe}_x\mathrm{Si}_2$ $(0 \leq x \leq 2)$, and $\mathrm{URu}_{2-x}\mathrm{Os}_x\mathrm{Si}_2$ $(0 \leq x \leq 1.2)$ were prepared by arc melting high-purity starting materials, in stoichiometric ratio, on a water-cooled copper hearth in a zirconium gettered argon atmosphere. Elemental U (3N, New Brunwick Lab) was obtained in ingot form and had to be sectioned with bolt cutters, after which selected pieces were etched for 2 minutes in $1:1$ $\mathrm{HNO_3/H_2O}$ to remove the oxide layer. Co (3N, Alfa Aesar), Ni (4N5, Puratronic), Ge (6N, Puratronic), and Si (6N, Alfa Aesar) were cut to smaller pieces from large solid chunks. Fe (4N, Alfa Aesar) was arc melted, and then brushed to remove iron-oxide. Ru (3N5, ESPI) and Os (3N5, Alfa Aesar) were initially melted into balls from powder in an arc furnace, which served to reduce their surface area, remove any oxide layer, and, by increasing their mass, make them easier to handle. After arc melting, each sample was flipped over and remelted. This process was repeated five times in order to ensure homogeneous mixing of the starting materials. This was followed by annealing in vacuum at 900 °C for 5 days.

2.2 Measurements

2.2.1 X-ray diffraction and energy dispersive x-ray

The crystal structure was verified by means of x-ray powder diffraction (XRD) using a Bruker D8 Discover x-ray diffractometer with Cu-Kα radiation. X-ray slides were prepared by mixing powdered samples with Petrolatum jelly. The resulting XRD patterns were fitted via Rietveld refinement[34] using the GSAS+EXPGUI software package [35]. The chemical composition was investigated by means of energy dispersive x-ray spectroscopy (EDX) using a FEI Quanta 600 scanning electron microscope equipped with an INCA EDX detector from Oxford instruments.

2.2.2 Electrical resistivity

Electrical resistivity measurements were performed using a home-built probe in a liquid ^{4}He dewar for temperatures 1 K $\leqslant T \leqslant$ 300 K by means of a standard four-wire technique at $\sim$ 16 Hz using a Linear Research LR700 AC resistance bridge. The excitation current applied to the samples was 0.3 mA. For selected samples, $\rho(T)$ was also measured down to $T \approx$ 0.05 K in an Oxford Kelvinox-300 ^{3}He-^{4}He dilution refrigerator. Electrical resistance R was converted to electrical resistivity ρ by

$$\rho = \frac{RA}{L}, \tag{2.1}$$

where A is the cross-sectional area and L is the distance between voltage leads.

2.2.3 Magnetization

Magnetization measurements were made for 2 K $\leq T \leq$ 300 K and in magnetic fields H = 0.001 T - 0.1 T using a Quantum Design SQUID magnetometer. Magnetization samples were prepared by placing 10 - 20 mg of material in a cotton-filled gelcap, preventing the sample from moving, which might cause errors in measurements. The capsule was then placed in a straw, which can be attached to the probe. The magnetic moment m, obtained from the measurement in units of emu, can be converted to magnetization M, in units of $\mu_B/\mathrm{f.u.}$ by

$$M = \frac{1.79 \times 10^{-4} m}{n}, \tag{2.2}$$

where n is number of moles of the sample.

2.2.4 Specific heat

Specific heat measurements were performed for 1.8 K $\leqslant T \leqslant$ 50 K in a Quantum Design Physical Property Measurement System semiadiabatic calorimeter using a heat-pulse technique. The total heat capacity, composed of the sample and addenda heat capacity, was determined by fitting the decay of the temperature after a heat pulse was sent through the temperature-stabilized sample. The addenda heat capacity, composed of the additional signal from the platform, attached wires, and grease on the platform, was measured using the same technique without a sample. The specific heat of the sample was then calculated by subtracting the addenda from the total heat capacity, and dividing by the number of moles of sample.

Chapter 3

$\mathbf{UCo}_{1-x}\mathbf{Ni}_x\mathbf{Ge}$

3.1 Introduction

Materials such as $\mathrm{ErRh_4B_4}$ [36, 37, 38] and $\mathrm{HoMo_6S_8}$ [39, 40], which display the coexistence of superconductivity (SC) and ferromagnetism (FM), have been known for over three decades. In these two compounds, the latter compounds T_C lies below T_{sc} and the superconductivity vanishes at a second, lower critical temperature $T_{sc}^{'} < T_C$. Within the temperature interval between T_{sc} and T_C, the ferromagnetism and superconductivity coexist macroscopically (in a spatially inhomogeneous manner), whereas a new sinusoidally-modulated state with a wavelength 100 Å and superconductivity coexist microscopically (within the same volume element) [41]. In contrast, the recently discovered uranium-based compounds UCoGe [42], $\mathrm{UGe_2}$ (under pressure) [43], UIr (under pressure) [44], and URhGe [45] appear to exhibit the microscopic coexistence of superconductivity and itinerant electron ferromagnetism. Such a coexistence is intriguing since, in a conventional superconductor, the large internal field generated by the ferromagnetic order would be expected to destroy the superconducting state by breaking the spin-singlet Cooper pairs [46]. It is thus often suggested that the superconducting electrons in such compounds may pair in triplet states, mediated by critical fluctuations associated with a ferromagnetic quantum critical point (QCP) [42, 47, 48].

A key question for any magnetic superconductor is how changes in the magnetic state effect the superconducting critical temperature. For UCoGe, both chemical substitution and pressure have been used to address this question. Upon isovalent doping of Si for Ge (UCoGe$_{1-x}$Si$_x$), both T_{sc} and T_C decrease until they both vanish simultaneously for $x \geq 0.12$ [47]. This result strongly suggests an intimate link between the two states, wherein the superconductivity is enhanced by the presence of ferromagnetic order. In contrast, under pressure, T_C decreases and T_{sc} initially increases [49, 50]. Near 1 GPa, T_C is suppressed to zero temperature and T_{sc} passes through a broad maximum of 1 K. A similar negative correlation between T_C and T_{sc} was found for small (1% and 5%) replacements of Co with Fe, Ru, and Ni, where the magnetic ordering temperature increased and the superconductivity was rapidly suppressed [51].

In this chapter, we report x-ray diffraction, electrical resistivity, and magnetization measurements on polycrystalline UCo$_{1-x}$Ni$_x$Ge samples for x spanning the entire range from 0 - 1. The motivation for this study was to examine the evolution of the superconducting and magnetic critical temperatures on tuning from weak itinerant ferromagnet UCoGe to antiferromagnetic (AFM) UNiGe. Both UCoGe and UNiGe crystallize in the orthorhombic TiNiSi structure [52]. UNiGe develops incommensurate AFM below 50 K and, below 42 K, commensurate AFM order sets in [53]. Low temperature measurements down to 0.4 K show no evidence for superconductivity in UNiGe [54].

3.2 Results

3.2.1 Crystal structure and sample quality

In this chapter, data for the annealed UCo$_{1-x}$Ni$_x$Ge was presented, although no significant differences between annealed and unannealed samples could be found in the diffraction patterns. The results for as-grown and annealed samples roughly agree for all dopings except undoped UCoGe, in which the annealed sample seemed to enhance the quality of the crystal.

Both UCoGe and UNiGe crystallize in orthorhombic TiNiSi structure (space group P_{nma}) and, correspondingly, powder x-ray diffraction patterns indicated that for the entire range of Ni substitutions $0 \leq x \leq 1$, samples can be described by the same space group and there are no indications of miscibility gaps. The typical goodness of fit extracted from the Rietveld refinement indicated by χ^2 ranged from 6 to 15. Fig. 3.1

illustrates the quality of the refinement that was typically achieved. As shown in Fig. 3.2, the lattice parameters a and b increase with increasing Ni concentration, while c decrease with larger x. However, the shift of b and c are much smaller. Overall, the unit cell volume of UCo$_{1-x}$Ni$_x$Ge increases linearly with x (Fig. 3.3).

3.2.2 Electrical Resistivity

Electrical resistivity as a function of temperature can be divided into 3 regions: a ferromagnetic region starting from x = 0 to 0.4 (Fig. 3.4 and Fig. 3.5), a crossover region from x = 0.5 to 0.6 (Fig. 3.6), and an antiferromagnetic region from x = 0.7 to 1 (Fig. 3.7 and Fig. 3.8). For resistivity data, the Curie temperature T_C of UCoGe is usually marked by a small hump [42, 48, 55]. Nonetheless, for our sample, the transition temperature is hard to define from resistivity data alone. A maximum, at $T \approx$ 2.3 K, in the derivative of resistivity was used to identify T_C (inset of Fig. 3.4). As illustrated in Fig. 3.5, T_C in ferromagnetic region is visible as a maximum in $\rho(T)$. T_C increases with x from $\approx$ 2 K at x = 0.05 to a maximum value of 25 K at x = 0.3, before decreasing to 23 K at x = 0.4. In the crossover region (Fig. 3.6), there is a broad minimum in each of the samples below which the curvature becomes strongly negative. The minima are so broad that it is difficult to determine the transition temperature. As will be discussed in more detail in section 3.2.3 and section 3.3.1 of this chapter, our data indicates that transitions in this region is neither ferromagnetic nor antiferromagnetic. For samples in the antiferromagnetic region (Fig. 3.7), the antiferromagnetic transition temperature or Néel temperature T_N can be seen as a minimum in $\rho(T)$. T_N increases with x from 39 K at x = 0.7 to a maximum value of 49 K at x = 0.9. Interestingly, x = 0.9 also shows a maximum at 32 K and an upturn at low temperatures. Unlike the other samples in this region, the T_N of UNiGe is determined by a shoulder in $\rho(T)$, and has a value of 44 K.

Of all the UCo$_{1-x}$Ni$_x$Ge samples studied in this project, only undoped UCoGe ($T_{sc} \approx$ 0.68 K) displayed superconductivity. The rapid suppression of T_{sc} is in agreement with the results from [51].

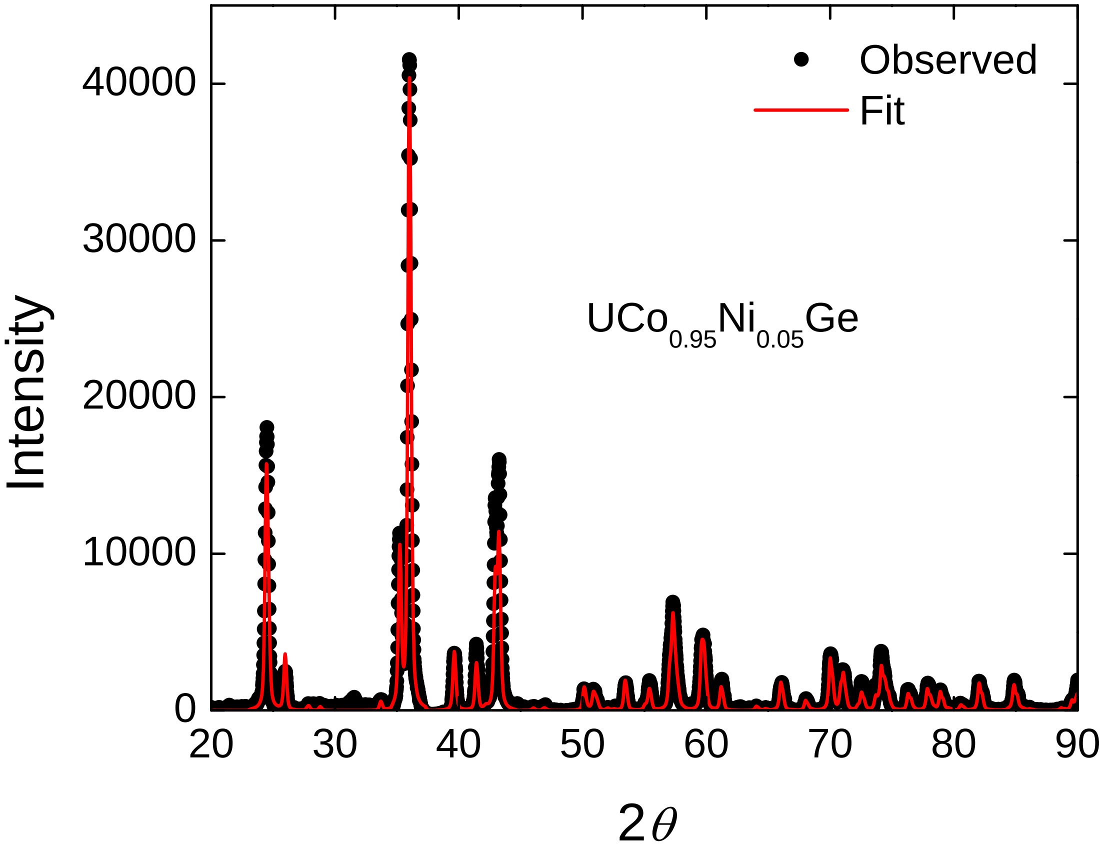

Figure 3.1: X-ray diffraction pattern of $UCo_{1.95}Ni_{0.05}Ge$. Black dots represent the data, and the red solid line is the fit to the data.

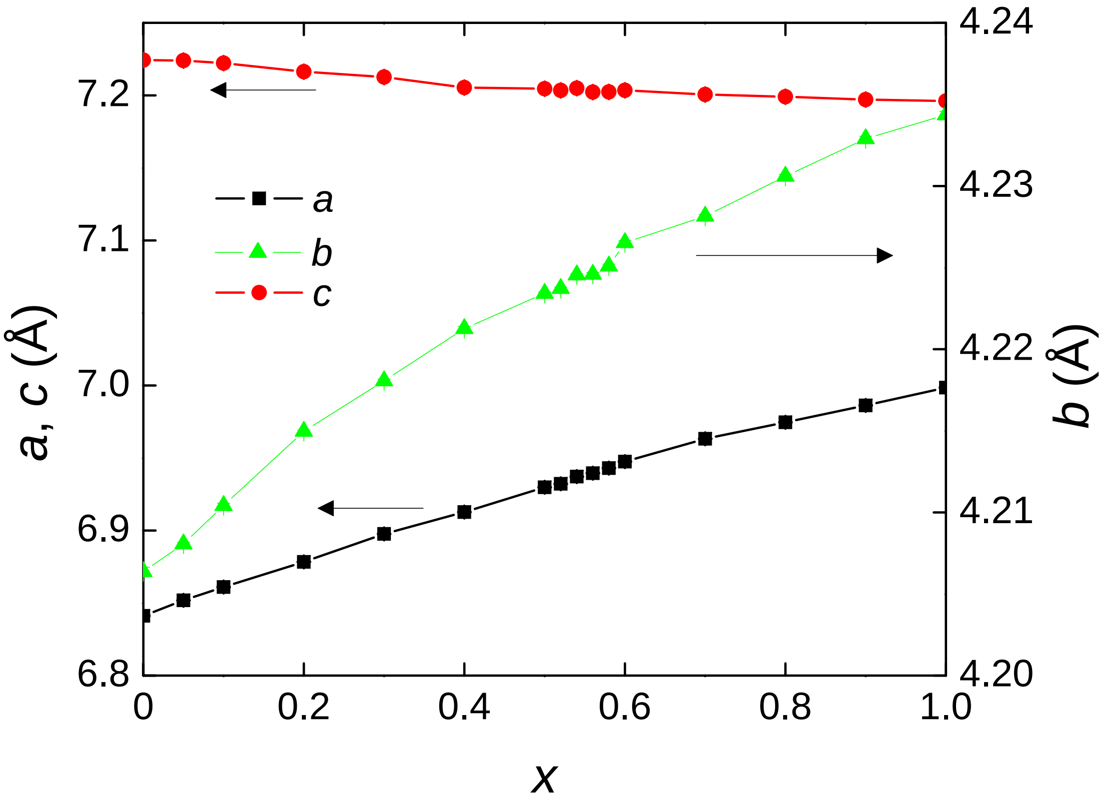

Figure 3.2: Lattice parameters a, b, and c vs. Ni concentration x.

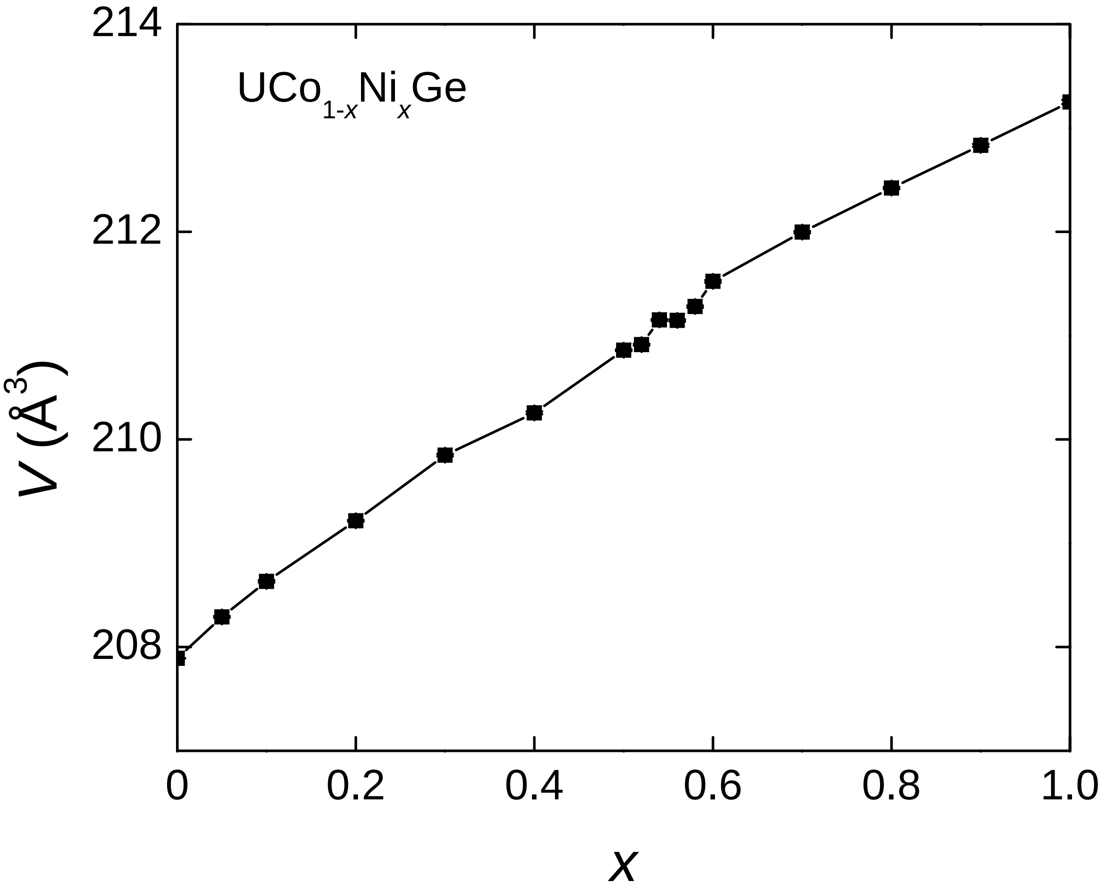

Figure 3.3: Unit cell volume V vs. Ni concentration x.

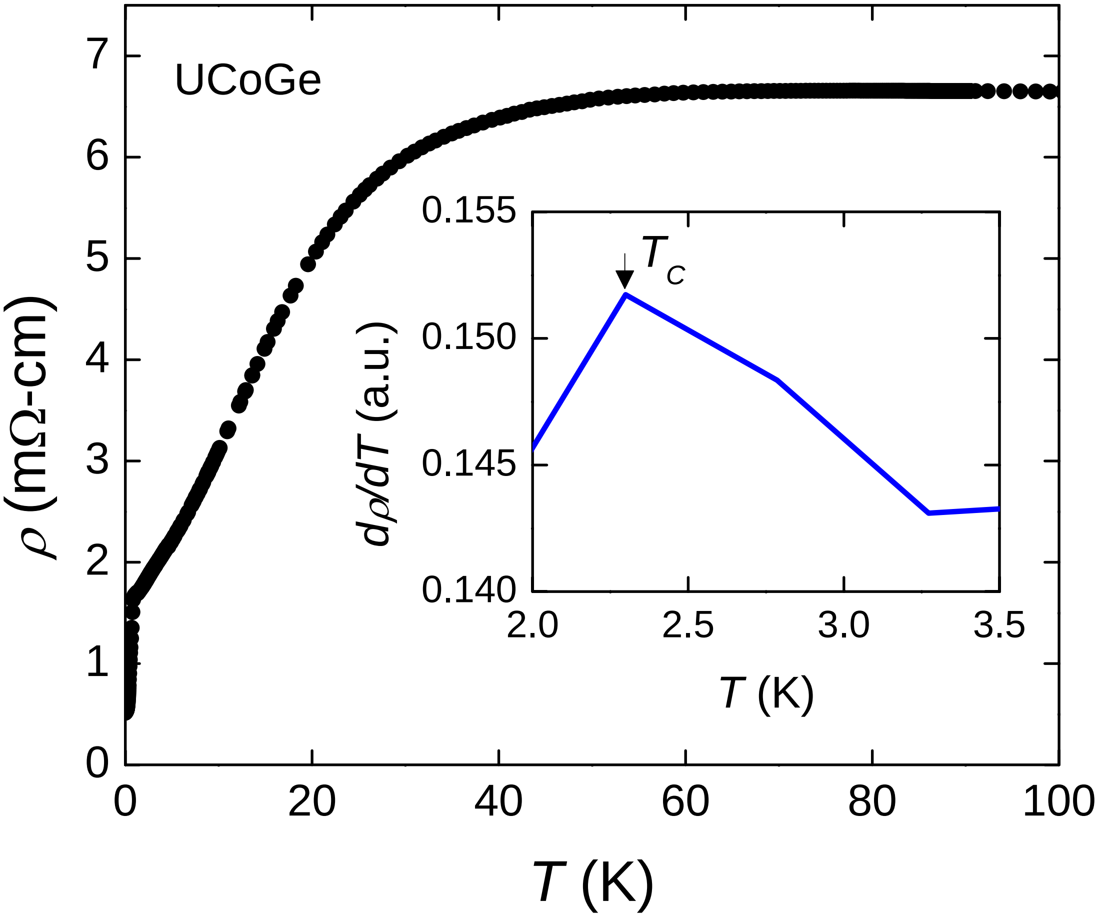

Figure 3.4: Electrical resistivity ρ vs. temperature T for UCoGe. Inset: derivative of ρ with respect to T, $d\rho/dT$, vs. T. The solid arrow marks the ferromagnetic transition temperature T_C.

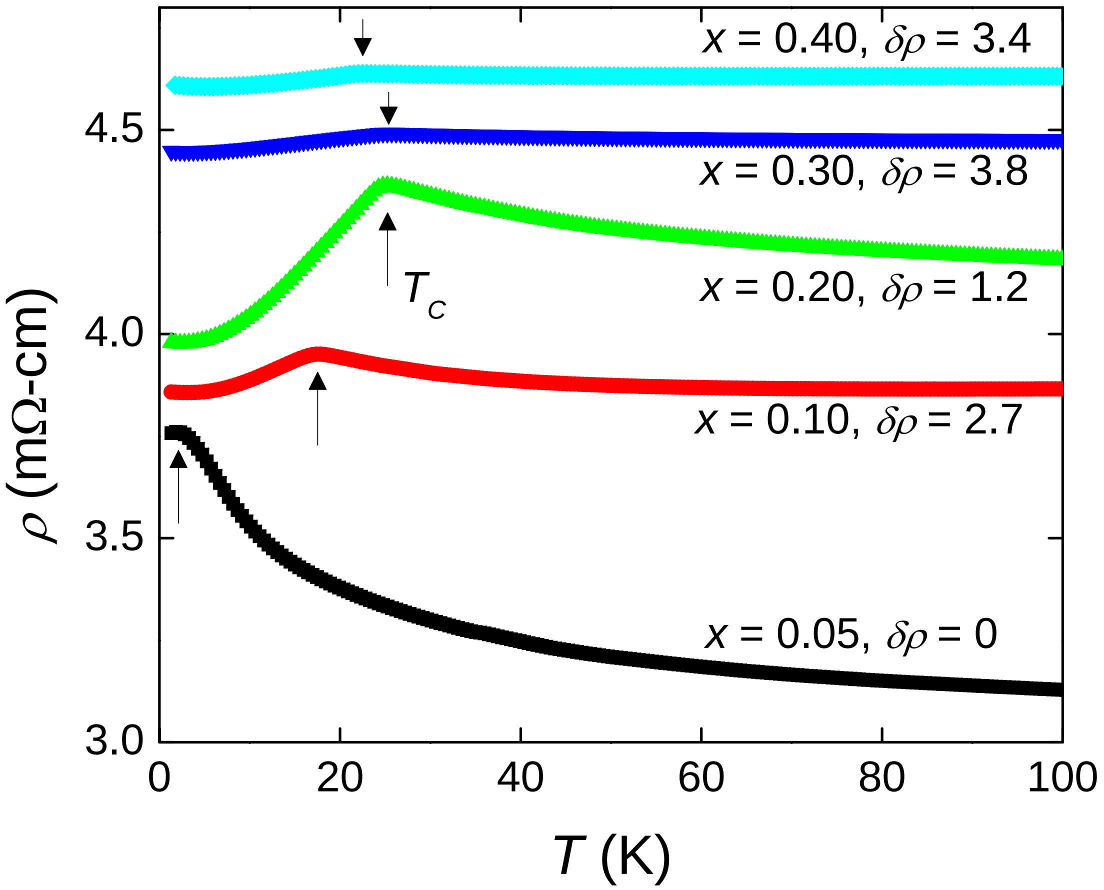

Figure 3.5: Electrical resistivity ρ vs. temperature T for, $0 < x \leq 0.4$, $\mathrm{UCo_{1-x}Ni_xGe}$. Each data set is shifted by $\delta\rho$, the values of which are indicated in the figure. The solid arrows mark the ferromagnetic transition temperature T_C.

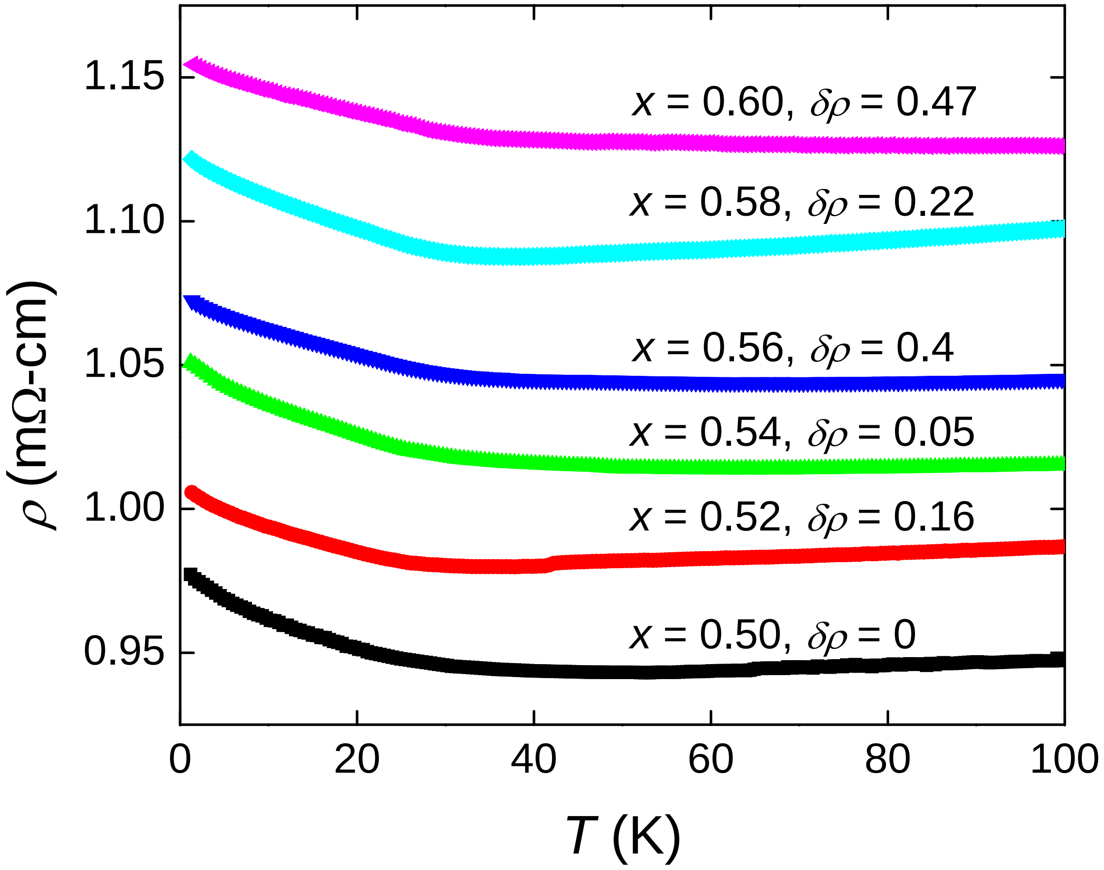

Figure 3.6: Electrical resistivity ρ vs. temperature T for, $0.5 \leq x \leq 0.6$, $\mathrm{UCo}_{1-x}\mathrm{Ni}_x\mathrm{Ge}$. Each data set is shifted by $\delta\rho$, the values of which are indicated in the figure.

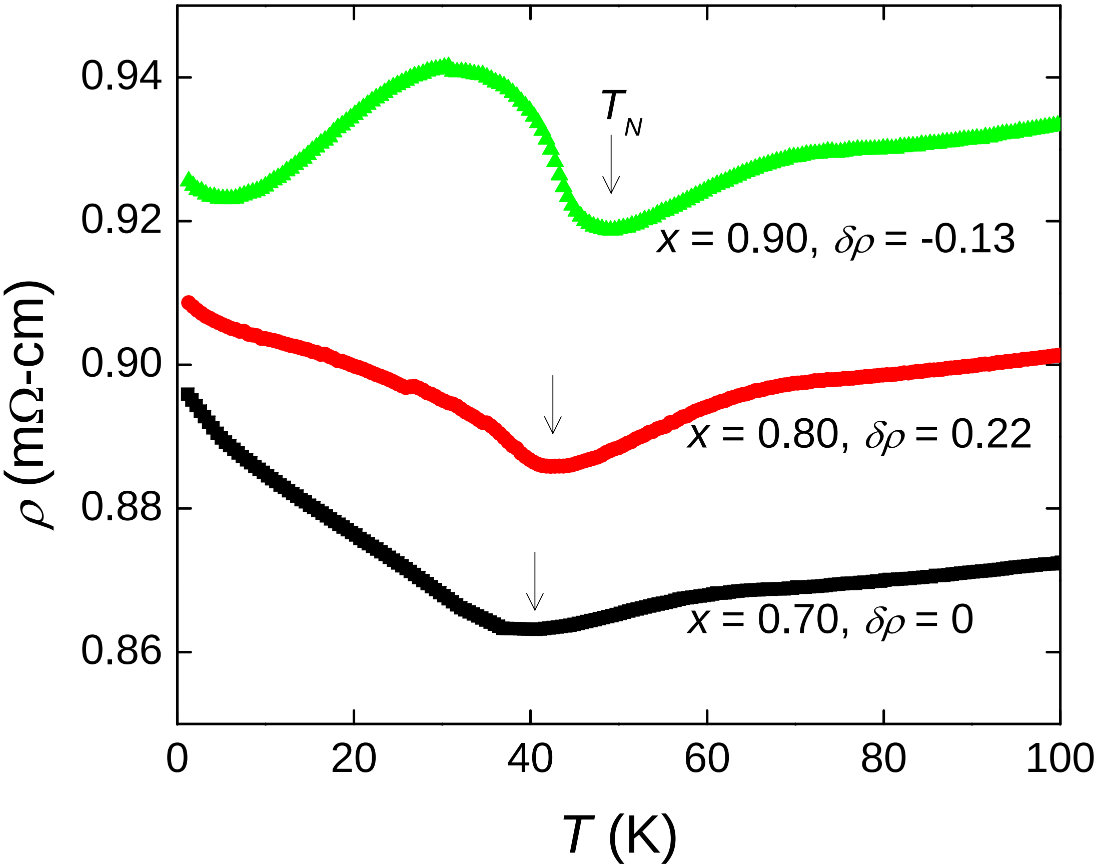

Figure 3.7: Electrical resistivity ρ vs. temperature T for, $0.7 \leq x \leq 0.9$, UCo$_{1-x}$Ni$_x$Ge. Each data set is shifted by $\delta\rho$, the values of which are indicated in the figure. The open arrows mark the antiferromagnetic transition temperature T_N.

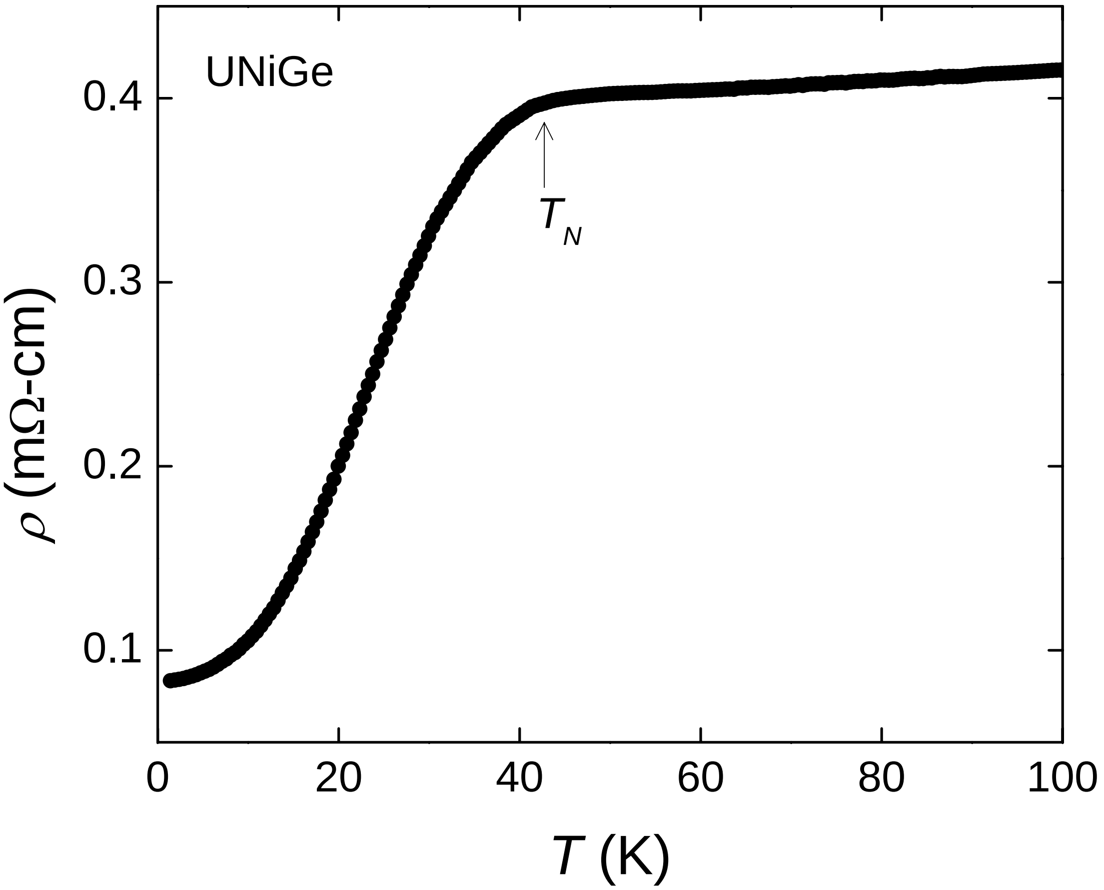

Figure 3.8: Electrical resistivity ρ vs. temperature T for UNiGe. The open arrow marks the antiferromagnetic transition temperature T_N.

3.2.3 Magnetization

Magnetization $M(T)$ as a function of temperature T was measured on cooling from room temperature to 2 K in applied fields H of 0.001 T and 0.01 T. Similar to electrical resistivity data, magnetization data can also be separated into ferromagnetic, crossover, and antiferrmagnetic regions. Samples with $x \leq$ 0.4 (Fig. 3.9) show a clear ferromagnetic characteristic. The transition temperature T_C is defined by extrapolating the magnetization near the transition to zero. T_C increases with x from $\approx$ 3 K for UCoGe to a maximum value of 26 K at x = 0.2, before it decreases to 23 K at x = 0.4. For samples in the intermediate doping range ($x = 0.5 - 0.56$) or the crossover region, the exact nature of the magnetic order is difficult to unambiguously determine from $M(T)$ alone. As illustrated in Fig. 3.10, the magnetization in 0.001 T saturates at low temperatures, whereas in 0.01 T (Fig. 3.11), the magnetization passes through a weak maximum suggesting possible AFM behavior. For samples with $x \geq 0.58$ (Fig. 3.12), $M(T)$ displays a peak that is typical of AFM order, and also can be used to determined T_N which has an initial value of 24 K at x = 0.58, and maximizes with a value of 44 K at x = 0.9. Superconductivity is not observed in $M(T)$ for any samples down to 2 K.

The magnetic field dependence of magnetization $M(H)$ was measured at 2 K in applied fields up to 7 T. In samples with $x \leq$ 0.4 (Fig. 3.13), the measurement shows typical ferromagnetic behavior. The magnetization at high fields is enhanced as x increases, until reaching a maximum at x = 0.3, which is in a good agreement with the enhancement of T_C with increasing x in $M(T)$. For 0.5 $\leq x \leq$ 0.56 (Fig. 3.14), $M(H)$ exhibits a hysteresis loop, but a different curvature than that of ferromagnetism is observed. Thus, magnetic order in this region might be different from that of low Ni concentrations. In order to further investigate this problem, Arrott plots were prepared, which are discussed in section 3.3.1. For $x \geq 0.58$ (Fig. 3.15), $M(H)$ displays exemplary antiferromagnetic behavior without hysteresis.

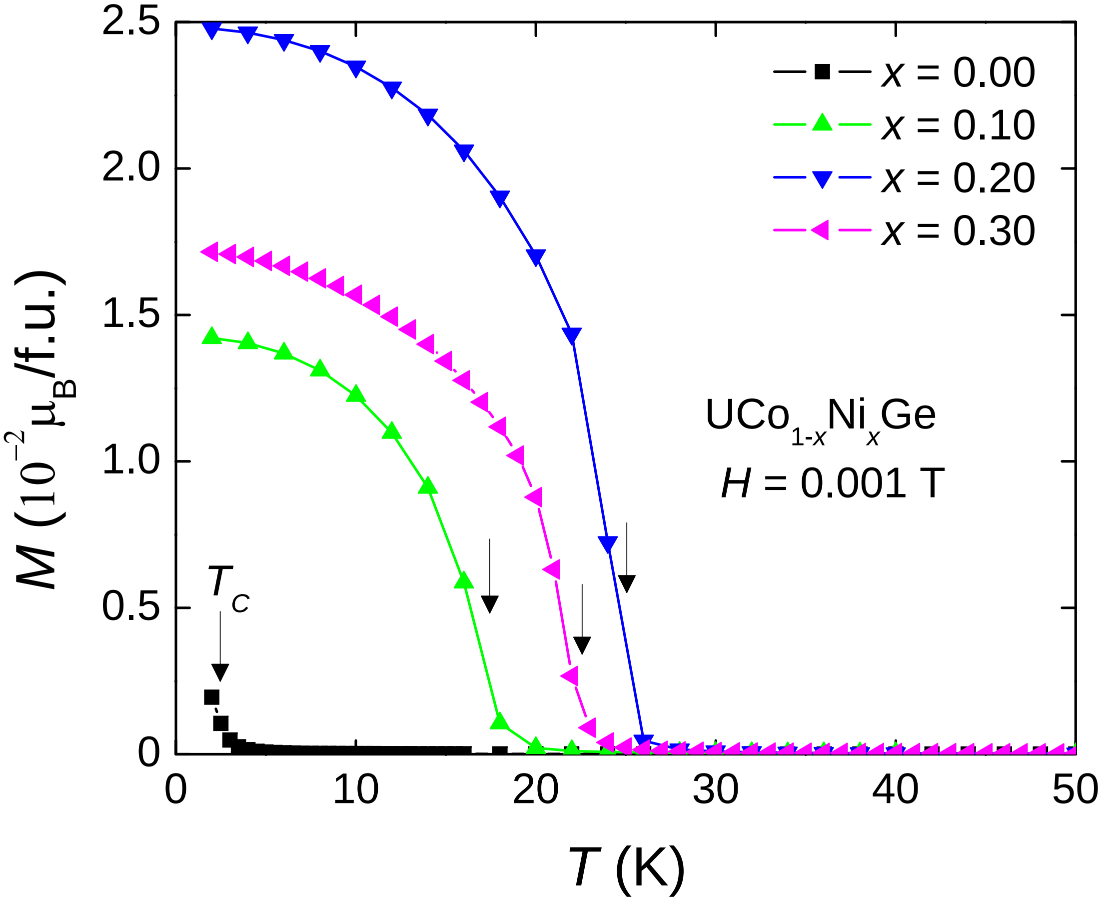

Figure 3.9: Magnetization M vs. temperature T for, $0 \leq x \leq 0.3$, UCo$_{1-x}$Ni$_x$Ge in a magnetic field H = 0.001 T.

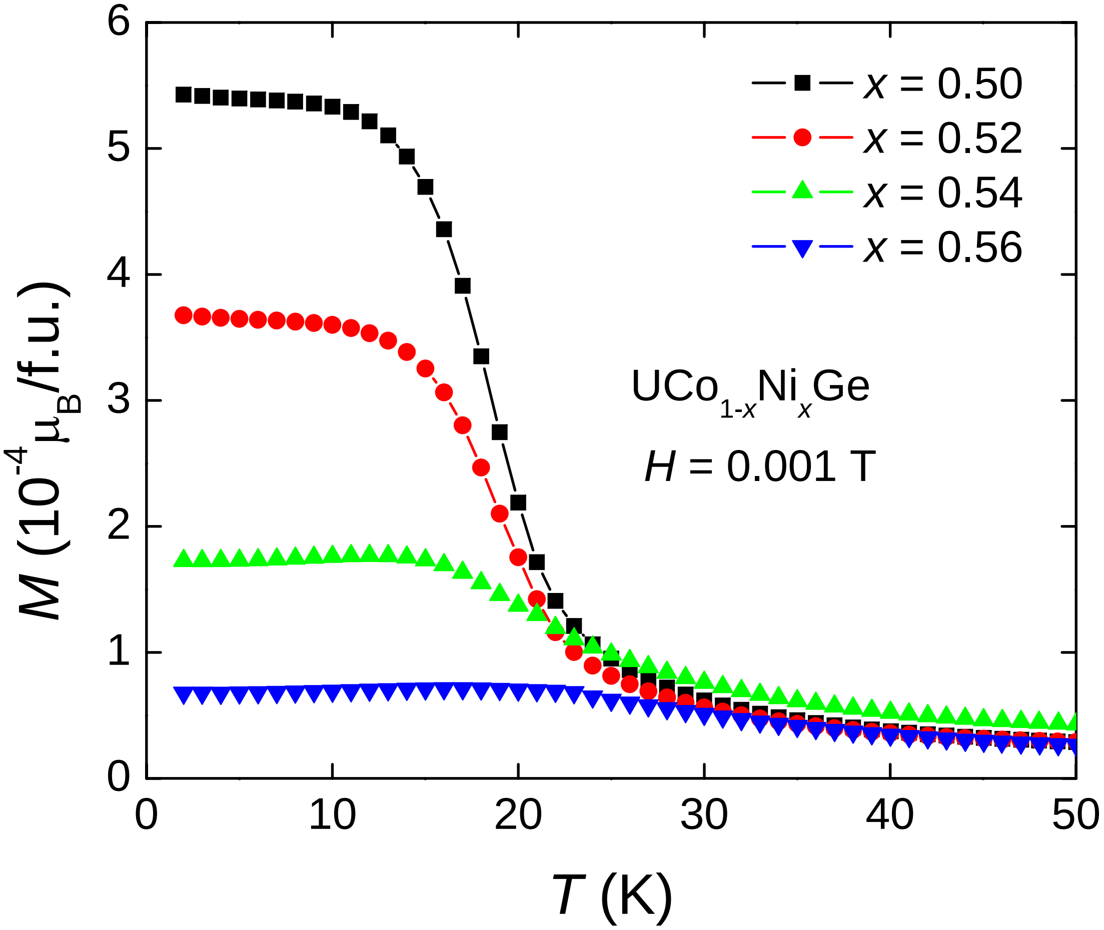

Figure 3.10: Magnetization M vs. temperature T for, $0.5 \leq x \leq 0.56$, UCo$_{1-x}$Ni$_x$Ge in a magnetic field H = 0.001 T.

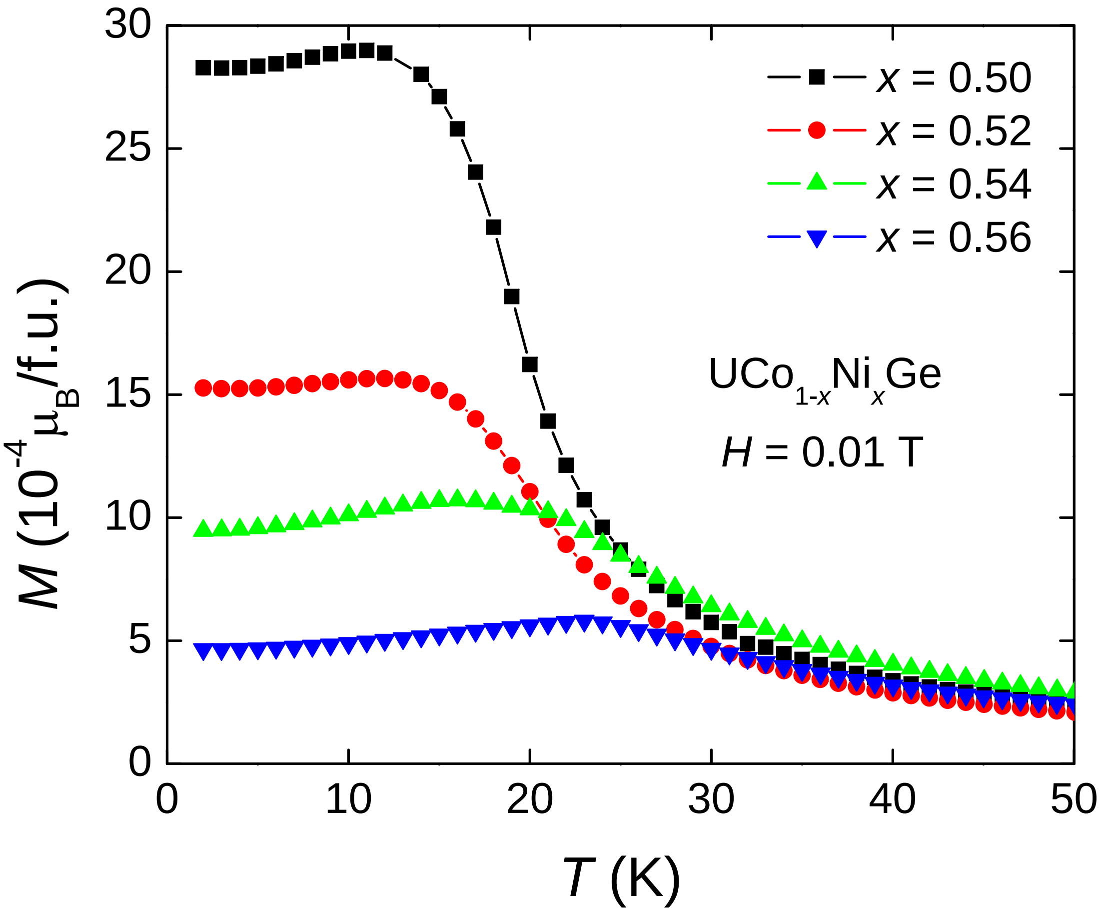

Figure 3.11: Magnetization M vs. temperature T for, $0.5 \leq x \leq 0.56$, UCo$_{1-x}$Ni$_x$Ge in a magnetic field H = 0.01 T.

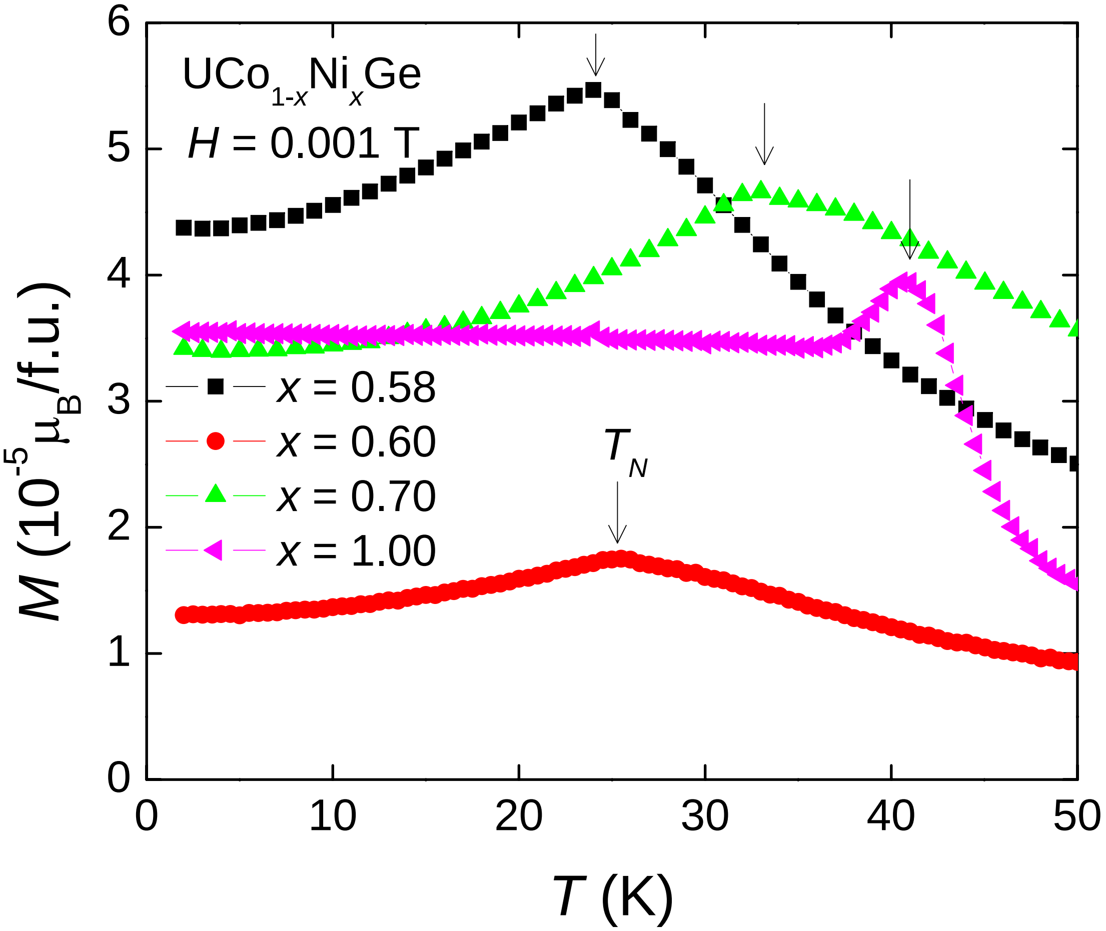

Figure 3.12: Magnetization M vs. temperature T for, $0.58 \leq x \leq 1$, UCo$_{1-x}$Ni$_x$Ge in a magnetic field H = 0.001 T.

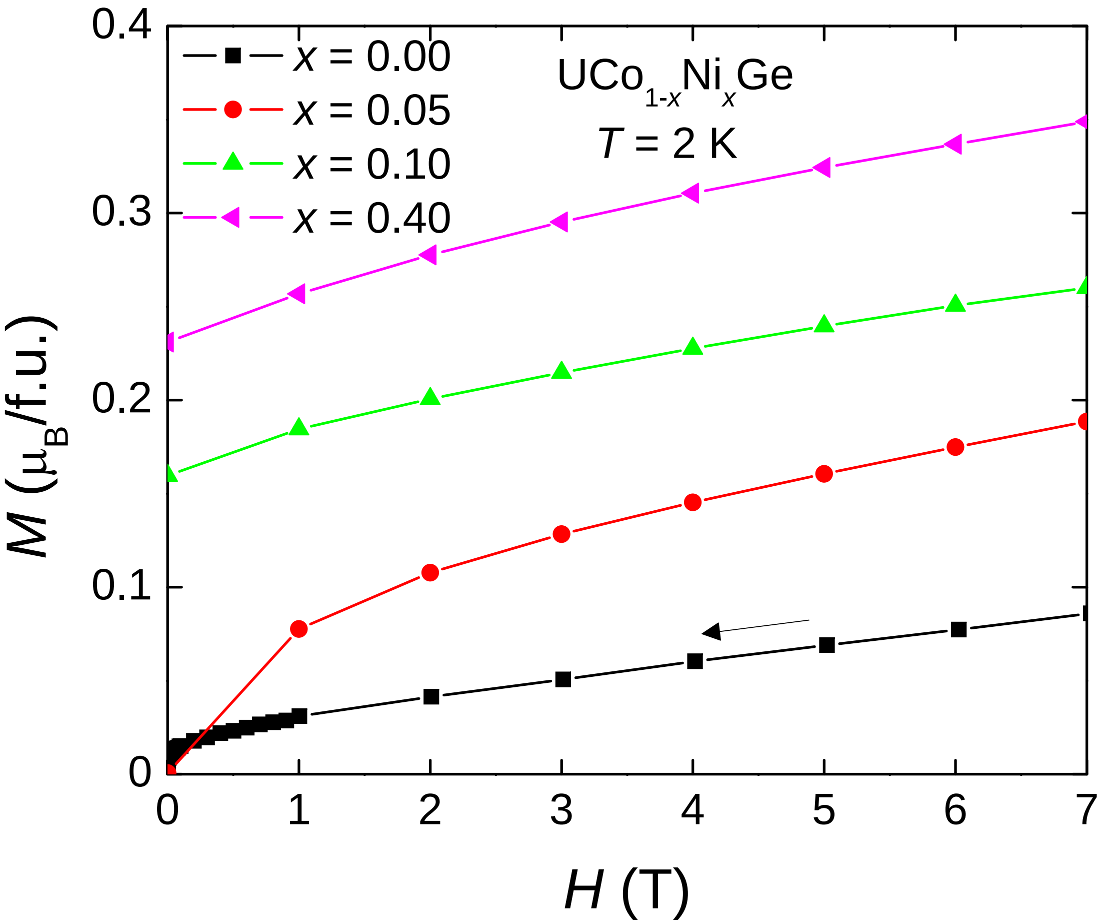

Figure 3.13: Magnetization M vs. field H for, $0 \leq x \leq 0.4$, UCo$_{1-x}$Ni$_x$Ge at 2 K.

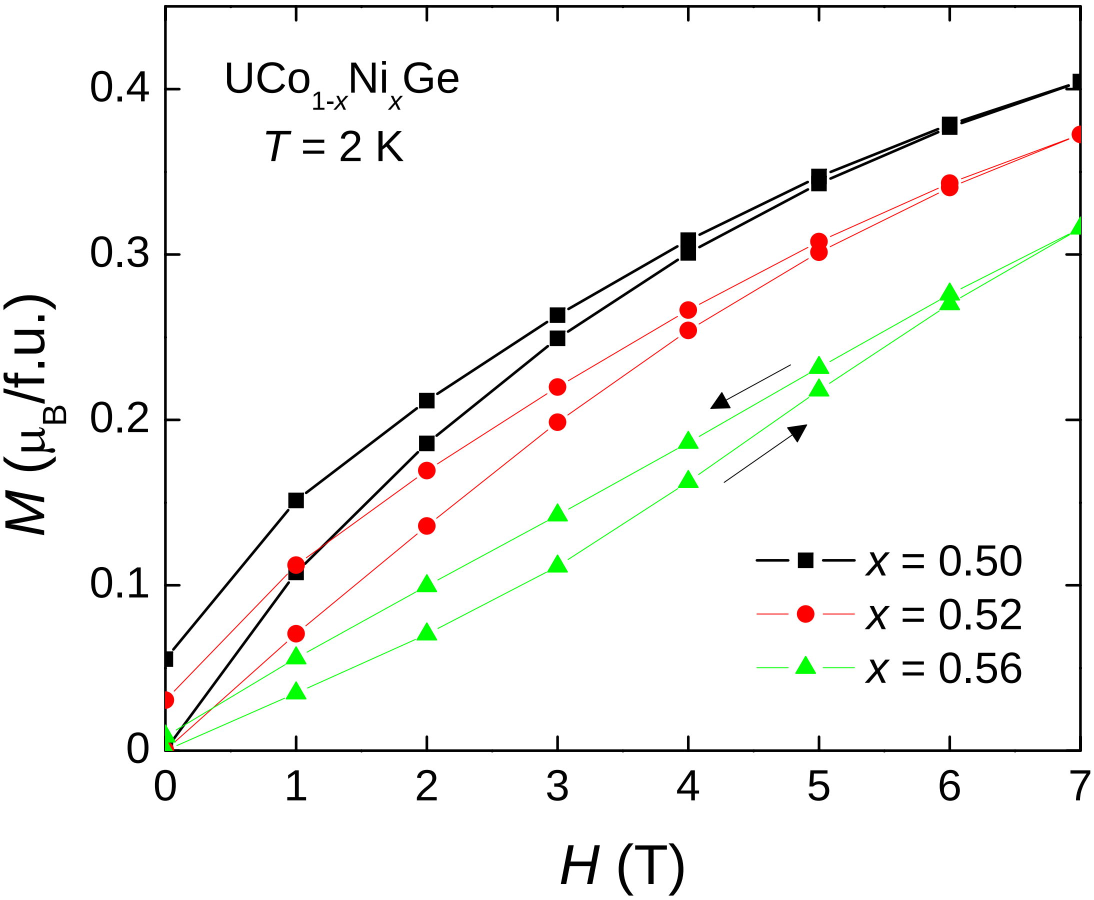

Figure 3.14: Magnetization M vs. field H for, $0.5 \leq x \leq 0.56$, UCo$_{1-x}$Ni$_x$Ge at 2 K.

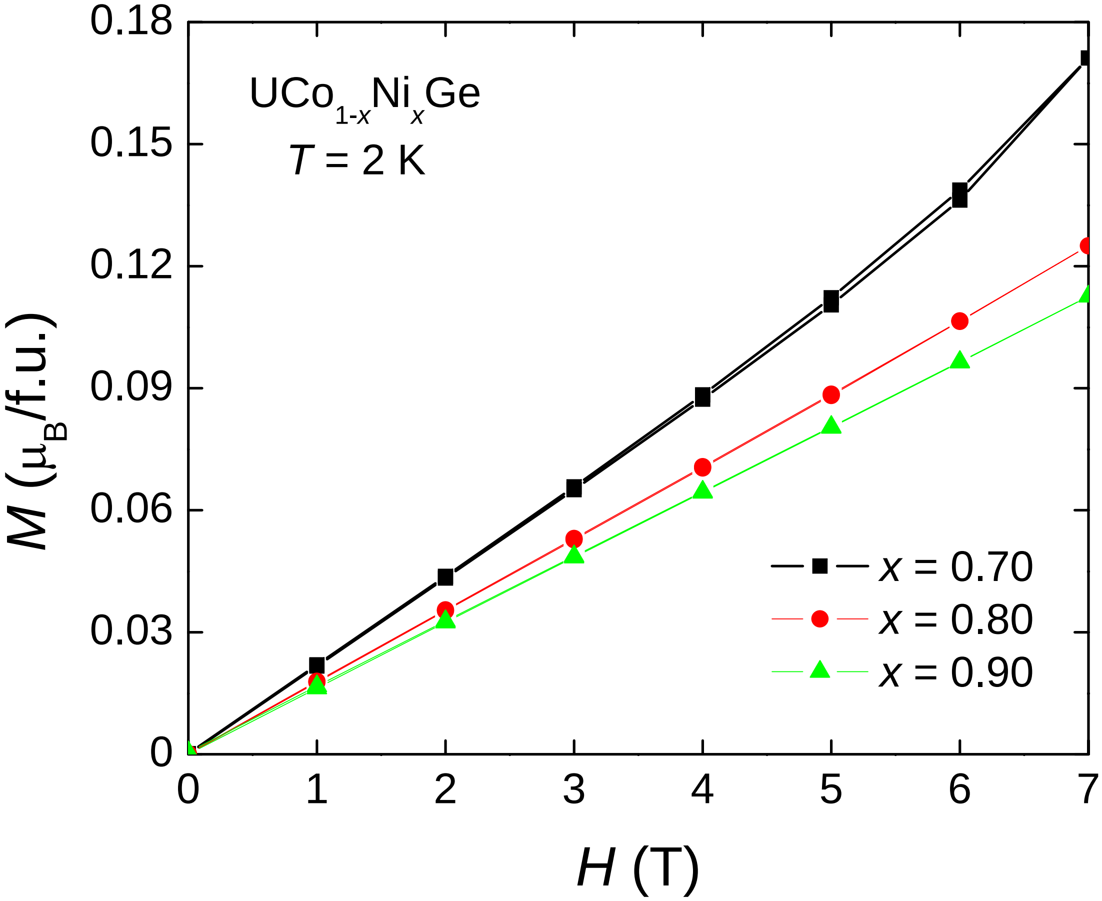

Figure 3.15: Magnetization M vs. field H for, $0.7 \le x \le 0.9$, $UCo_{1-x}Ni_xGe$ at 2 K.

3.3 Discussions

3.3.1 Arrott plot

The Arrott plot, a plot between the square of the magnetization in a field, and the field divided by the magnetization (M^2 vs. H/M) at certain temperatures T [56], is one of the experimental methods to establish ferromagnetism. The Curie temperature can be determined by the isotherm that passes through the origin. This can be understood from the equation [57],

$$M^2 = \frac{1}{4b}\frac{H}{M} + \frac{a}{2b}(T_C - T), \tag{3.1}$$

where a and b are positive constants. A schematic plot of this equation is shown in Fig. 3.16.

This method can be utilized to identify T_C effectively for samples with low Ni concentration. As illustrated in Fig. 3.17, T_C = 2.4 K was extracted from the Arrott plot for x = 0.05. However, the Arrott plots of samples in the crossover region do not behave in a similar fashion (Fig. 3.18 and Fig. 3.19). The slope is strongly enhanced, and none of the isotherms can be extrapolated to intercept the origin. Furthermore, according to Eq. 3.1 when linearly extrapolated, data with lower T would intercept the y-axis at larger value than that with higher T. Nevertheless, Fig. 3.19 shows that the y-axis interception for data with higher T would be larger than that with lower T. Since the Arrott plot is based on a mean-field theory, that it failed to explain the system with competing order might be due to the limitation of the theory. Mean-field theories assume that all regions of the sample are identical, and hence ignore fluctuations [57], which is of great importance for the crossover region since it is in the middle of transition between ferromagnetic phase and antiferromagnetic phase. Samples in the region between $x = 0.5 - 0.56$ (crossover region) could exhibit magnetic phase separation, glassy behavior, or some other form of complex magnetism. Further measurements (e.g., neutron diffraction) are necessary to distinguish between these possibilities.

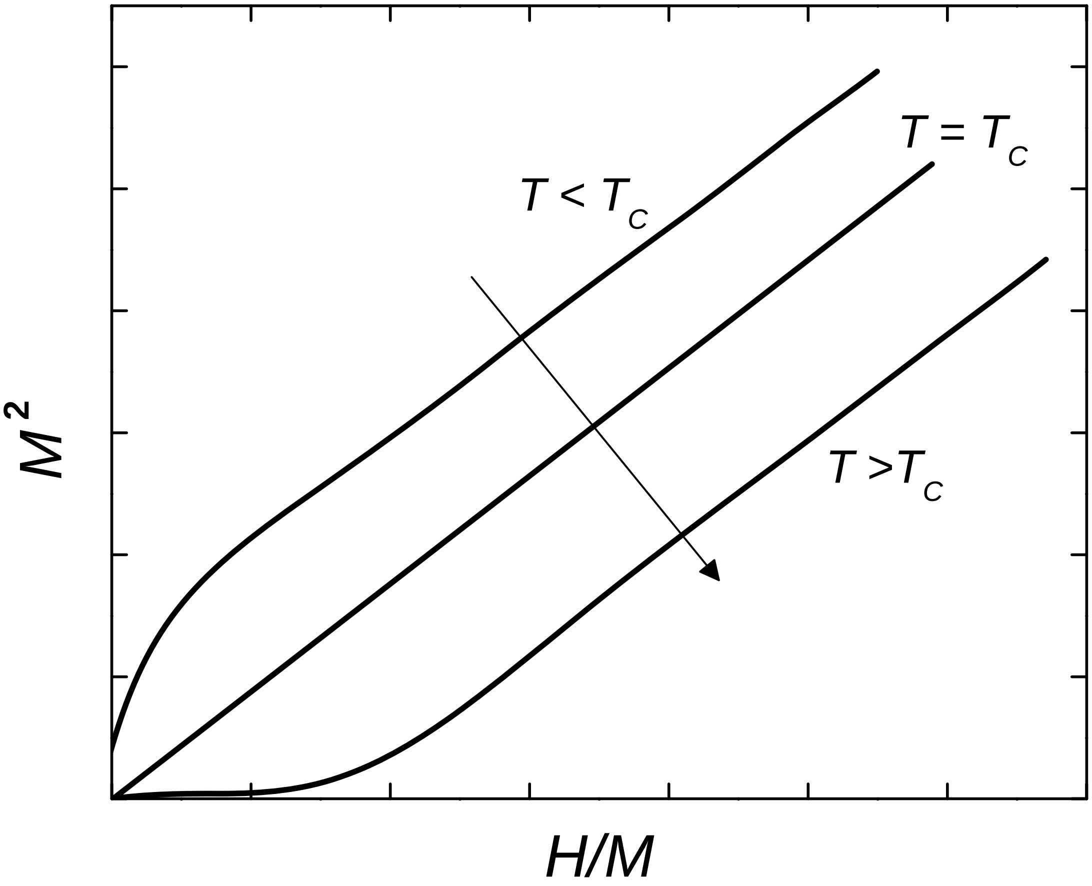

Figure 3.16: Magnetization squared vs. field divided by magnetization for $T < T_C$, $T = T_C$, and $T > T_C$.

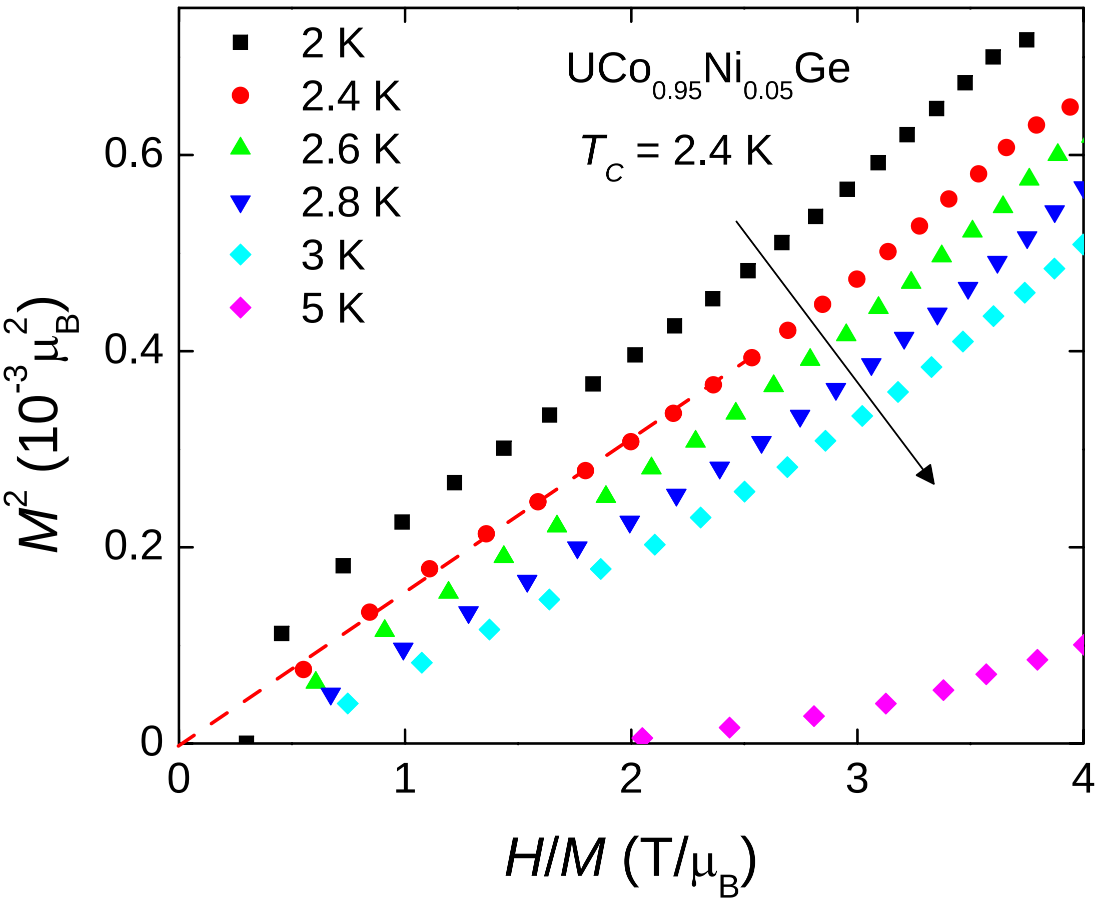

Figure 3.17: Arrott plot of $UCo_{1.95}Ni_{0.05}Ge$. The red dash line is an extrapolated line from T = 2.4 K data, intercepting zero.

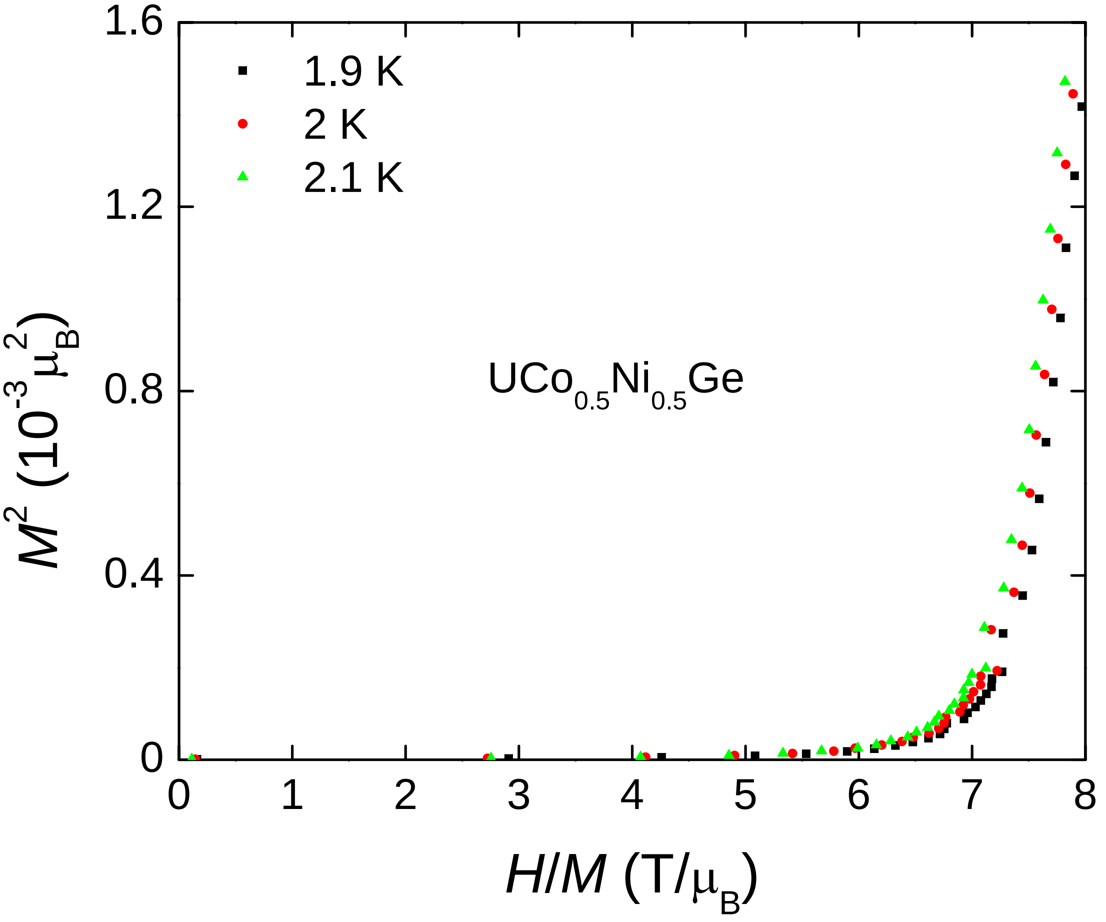

Figure 3.18: Arrott plot of $UCo_{0.5}Ni_{0.5}Ge$.

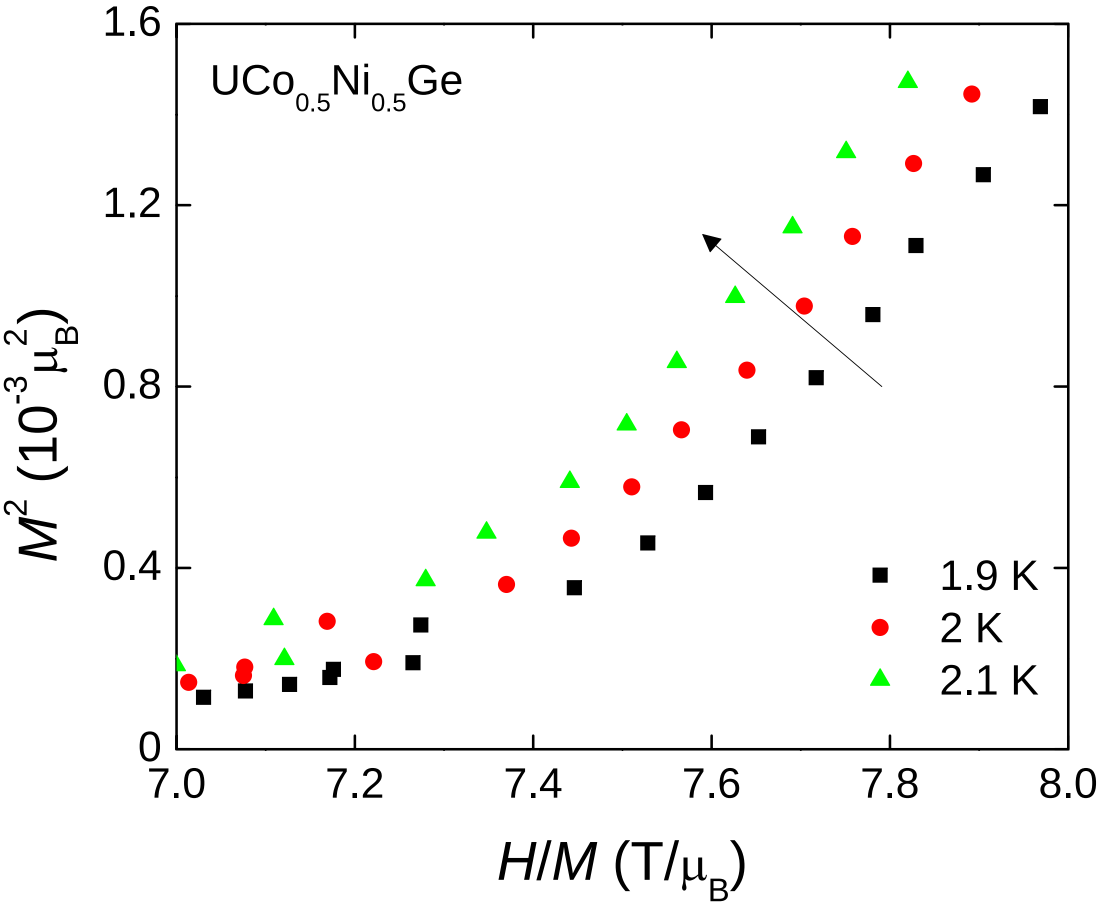

Figure 3.19: High field region of Arrott plot of $UCo_{0.5}Ni_{0.5}Ge$.

3.3.2 Itinerant ferromagnetism

One way to decide whether our sample exhibit itinerant ferromagnetism is to calculate the ratio between effective magnetic moment μ_{eff} and saturation magnetic moment μ_S. The criterion for itinerant ferromagnetism is [58, 59]

$$\frac{\mu_{eff}}{\mu_s} >> 1. \tag{3.2}$$

As illustrated in Fig. 3.20, the effective moment was determined by fitting the high temperature region of the reciprocal magnetic susceptibility $\frac{1}{\chi}$ with the modified Curie-Weiss law;

$$\frac{1}{\chi - \chi_0} = \frac{T - T_C}{C}, \tag{3.3}$$

where χ_0 is a constant due to Pauli or Van Vleck paramagnetism [60], and

$$\mu_{eff} = 2.82C^{\frac{1}{2}}. \tag{3.4}$$

μ_s was obtained by linearly extrapolating $M(H)$ curve to zero field. A plot of μ_{eff}, μ_s, and their ratio is displayed in Fig. 3.21. μ_{eff} peaks at $x = 0.1$, while μ_s maximizes at $x = 0.2$, the concentration with highest value of Curie temperature. $\frac{\mu_{eff}}{\mu_s}$ drops rapidly from almost 100 at $x = 0$ to less than 20 for the rest of the ferromagnetic samples. The plummet of the ratio is consistent with the suppression of superconductivity since no samples with $x \geq 0.05$ showed superconducting transitions. This indicates that itinerant ferromagnetism might play a significant role for superconductivity in UCoGe.

3.4 Conclusions

The phase diagram of UCo$_{1-x}$Ni$_x$Ge is shown in Fig. 3.22. Magnetic order starts as ferromagnetism for UCoGe with $T_C \approx$ 2.4 K, increases with x, and reaches a maximum value of 25 K at $x = 0.2$. For samples with $x = 0.5 - 0.58$, magnetic order cannot be ambiguously determined by resistivity, magnetization, or conventional Arrott plot analysis. Starting at $x = 0.6$, antiferromagnetism was detected. T_N increases to a maximum value of 44 K at $x = 0.9$, and slightly decreases to 41 K for UNiGe.

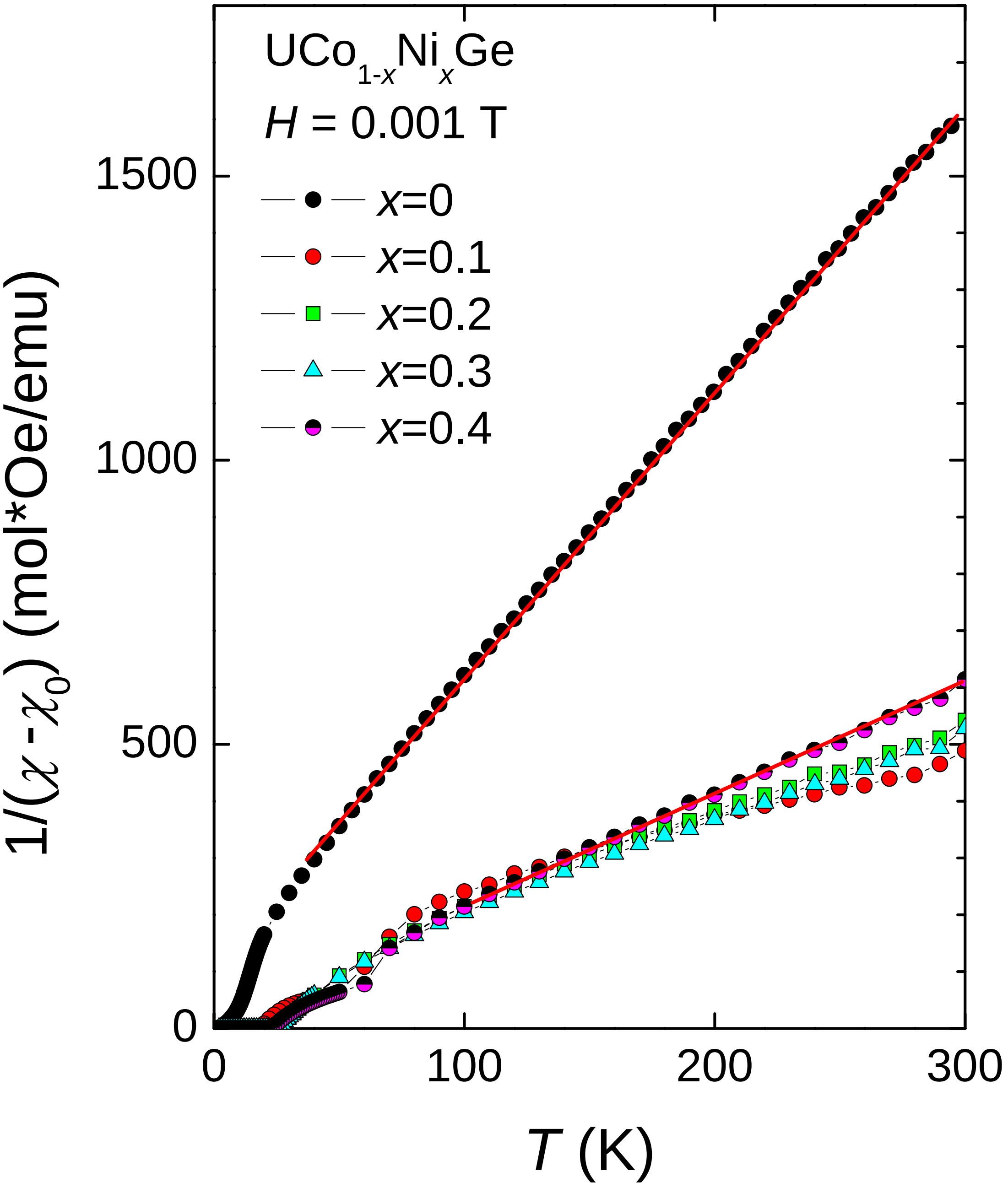

Figure 3.20: Inverse magnetic susceptibility $\frac{1}{\chi-\chi_0}$ vs. temperature T for, $0 \leq x \leq 0.4$, UCo$_{1-x}$Ni$_x$Ge in a magnetic field H = 0.001 T. The red lines represent linear fits of the modified Curie-Weiss law.

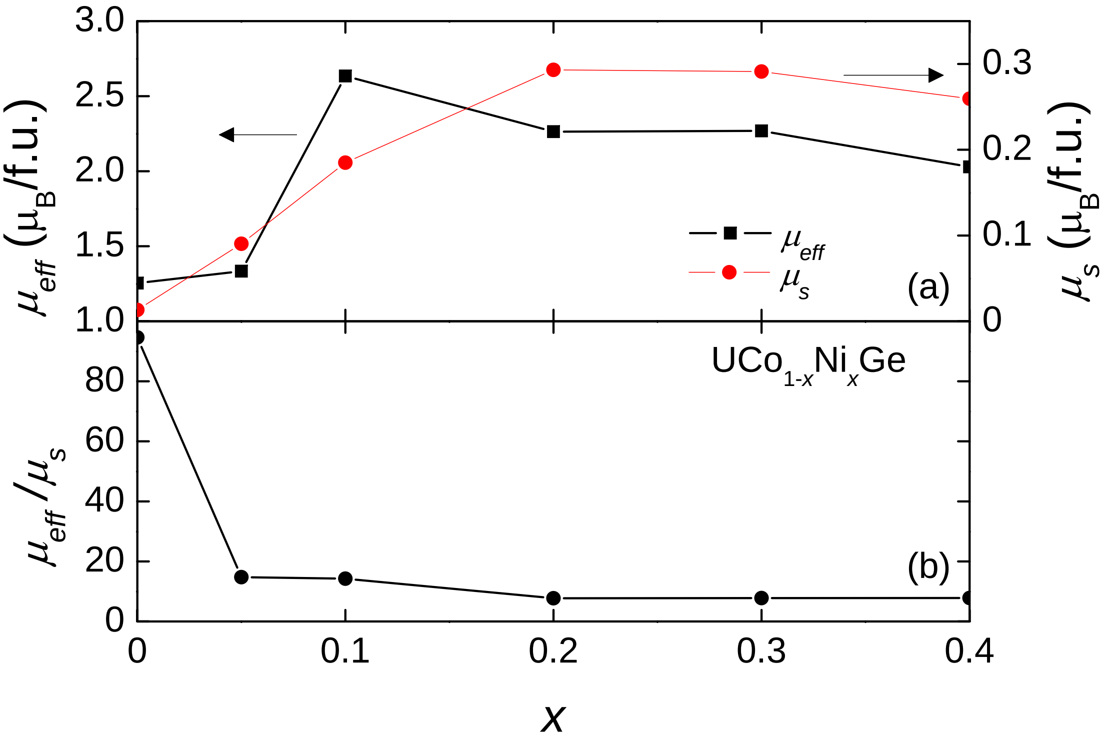

Figure 3.21: (a) Effective moment μ_{eff} and saturation moment μ_s. (b) Ratio $\frac{\mu_{eff}}{\mu_s}$ of UCo$_{1-x}$Ni$_x$Ge.

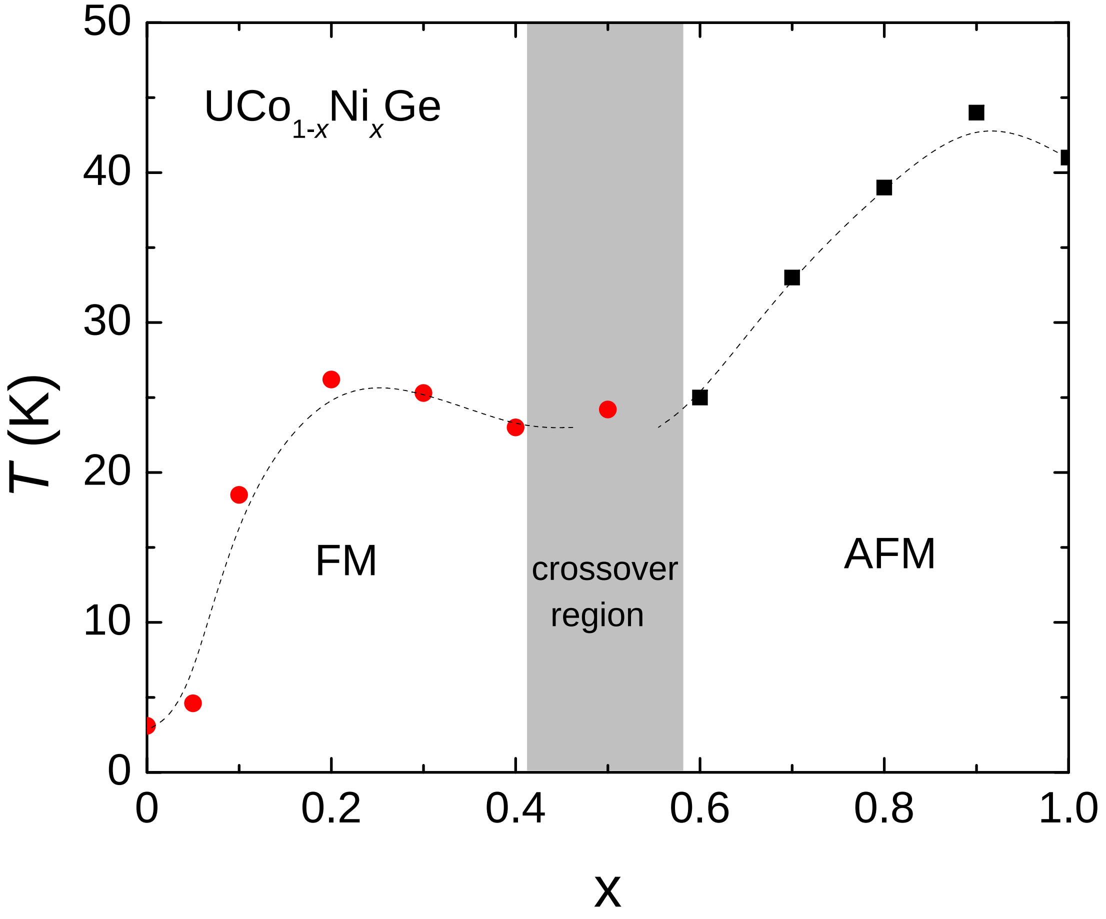

Figure 3.22: Phase diagram of $UCo_{1-x}Ni_xGe$. The gray area represents a region where samples showed no conclusive signs of ferromagnetism or antiferromagnetism, "crossover" region.

Superconductivity was suppressed with the lowest Ni concentration, $x = 0.05$.

A portion of the text and data presented in this chapter are reprints of material that appears in “Evolution of the magnetic and superconducting states in UCoGe With Fe and Ni substitution”, J. J. Hamlin, R. E. Baumbach, K. Huang, M. Janoschek, N. Kanchanavatee, D. A. Zocco, and M. B. Maple, Mater. Res. Soc. Symp. Proc. 1264, 1264-Z12-04 (2010). The dissertation author was a co-author of the article.

Chapter 4

$\mathbf{URu}_{2-x}\mathbf{Fe}_x\mathbf{Si}_2$

4.1 Introduction

The strong electronic correlations that arise from the hybridization of localized d- or f-electron and conduction electron states in compounds containing transition metal, lanthanide, or actinide ions with partially-filled d- or f-electron shells often lead to the emergence of novel electronic ground states such as heavy fermion metals, complex magnetic order, quadrupolar order, non-Fermi-liquid (NFL) behavior and unconventional superconductivity (SC) [61]. A prime example of such emergent behavior is the "hidden order" phase in the heavy fermion compound $\mathrm{URu_2Si_2}$ that occurs below T_0 = 17.5 K and coexists with SC below T_{sc} = 1.5 K [17, 18, 19]. The specific-heat anomaly that accompanies the HO phase transition is reminiscent of a second order BCS-like mean field transition that opens a gap $\Delta \approx$ 130 K over about 40 % of the Fermi surface(FS) due to a charge or spin density wave [18]. However, the small antiferromagnetic magnetic moment of only $\sim$ 0.03 μ_B/U derived from neutron scattering experiments [20, 21] cannot account for the entropy of $\sim$ 0.2Rln2 associated with the specific-heat anomaly [20]. The terminology HO [62] refers to the ordered phase responsible for the striking specific heat anomaly whose order parameter has eluded identification for nearly three decades.

The search for the OP of the HO phase has attracted an enormous amount of attention. A multitude of models for the HO have been proposed, which can be roughly divided into two groups, one based on a local OP and another involving order that occurs in momentum space [63, 64, 65, 66, 67, 68, 69, 70, 71, 72, 73, 74]. ARPES, [75] STM [76, 77] and PCS [27] studies show that upon cooling into the HO phase, the electronic structure is reorganized and a heavy quasiparticle band shifts below the Fermi level, where the crossing with a light hole-like band at $Q^* = \pm 0.3\pi/a$ leads to the formation of a hybridization gap Δ_{Q^*} = 5 meV. It was suggested that the HO may be a hybridization wave where Δ_{Q^*} is the corresponding OP [63, 74]. The recent proposal of a modulated spin liquid lies between the extremes of local and itinerant OPs [78].

The hybridization between localized f and conduction electron states may be tuned by varying a control parameter such as composition x, pressure P or magnetic field H, allowing information about the electronic ground state to be extracted from various measurements. This approach has been applied extensively to $\mathrm{URu_2Si_2}$, revealing rich T vs. x, P, and H phase diagrams with a plethora of competing electronic ground states. Through the application of pressure, it has been shown that the magnetic structure in the HO phase is identical to that of a larger moment antiferromagnetic phase that emerges at critical pressures $P_c \geq$ 0.5-1.5 GPa [23]. There is strong evidence that the HO-LMAFM phase transition is of first order [79], leading to the widely held view that the magnetic structure in the HO phase is due to a small amount of the LMAFM phase induced by strain [21]. However, other researchers believe that the small magnetic moment in the HO phase is intrinsic since its onset temperature coincides with that of the HO, and it is present in samples with residual resistivities that vary by as much as two orders of magnitude [80]. In fact, some models predict that antiferromagnetic order in the HO phase is intrinsic [69]. Tuning with H revealed several high field quantum phases that exhibit non Fermi liquid (NFL) behavior [81]. Finally, substitution of other transition metals for Ru generally leads to suppression of the HO [82], and, for example, yields a LMAFM phase for Rh substitution [83] and an itinerant ferromagnetic phase for Mn, Tc, or Re substitutions [84, 85] , accompanied by NFL behavior deep in the ferromagnetic state for Re [86, 87].

In this chapter, we demonstrate that substitution of the smaller Fe ions for Ru ions in $\mathrm{URu_2Si_2}$ provides a new approach for studying the properties of the HO phase. Measurements of electrical resistivity ρ, specific heat C, and magnetization M on a series of polycrystalline samples of $\mathrm{URu_{2-x}Fe_xSi_2}$ with Fe concentrations x ranging from

x = 0 to 2 reveal a remarkable phase diagram. The most salient characteristics of this phase diagram are (1) the striking shape of the $T - x$ phase boundary $T_0(x)$ separating the paramagnetic phase from the ordered phases (HO and/or LMAFM) with a more than two-fold enhancement of T_0; (2) features in $T_0(x)$, similar to those in the $T - P$ phase diagram of pure URu_2Si_2, that appear to be generated by "chemical pressure" (reduction in the unit cell volume) arising from the substitution of the smaller isoelectronic Fe ions for Ru ions, particularly the kink at $x = 0.2$ that maybe related to a HO-LMAFM transition; (3) increase of the energy gap Δ of the HO phase and the amount of the FS gapped by the HO phase with increasing x, inferred from fits of a theoretical model with gapped excitations to the low temperature electrical resistivity and specific heat; (4) coexistence of SC and HO for $x \lesssim 0.075$; and (5) the possible existence of a quantum critical point at $x \approx 1.3$ where the HO and/or LMAFM are suppressed to 0 K. This phase diagram may provide new opportunities for establishing the identity of the OP of the HO phase.

4.2 Results

4.2.1 Crystal structure and sample quality

UFe_2Si_2 is isostructural with URu_2Si_2 (space group $I4/mmm$) and, correspondingly, we find that samples for the entire range of Fe substitutions $0 \leq x \leq 2$ can be described in the same space group and there are no indications of miscibility gaps. The typical goodness of fit extracted from the Rietveld refinement indicated by χ^2 ranged from 4 to 10; Fig. 4.1(a) illustrates the quality of the refinement that was typically achieved. As shown in Fig. 4.1(b), the lattice parameters a and c decrease with increasing Fe concentration, although the decrease of c is much smaller. Overall, the unit cell volume of $URu_{2-x}Fe_xSi_2$ decreases linearly with x (Fig. 4.1(c)), as expected from the smaller size of Fe relative to Ru ions. Furthermore, the combined EDX/XRD refinement indicated correct composition within the accuracy of the measurement (see Fig. 4.1(d)) and no evidence of impurities, except for samples with x = 0.70, 0.80, and 1.00, where we identified a small amount of UO impurity phase of only a few percent.

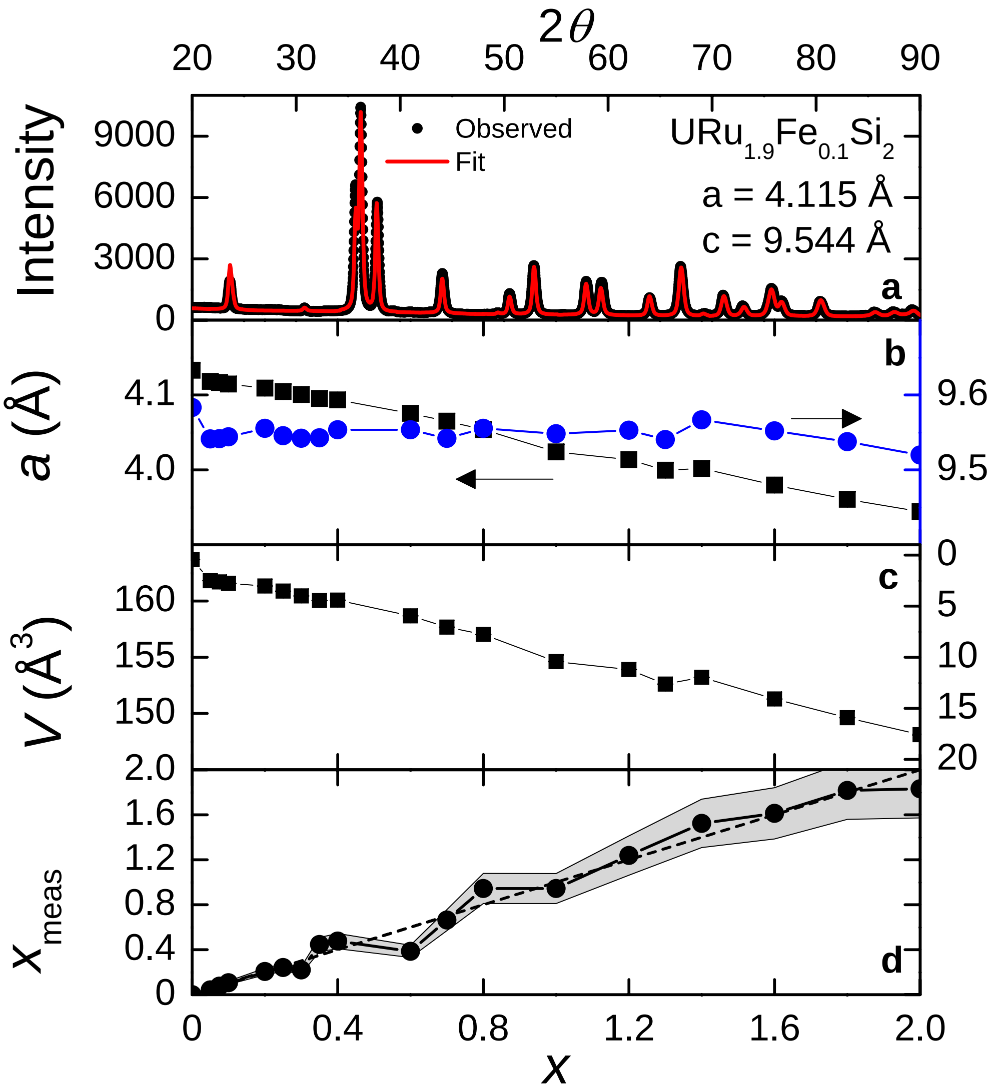

Figure 4.1: Results of the Rietveld refinement and EDX analysis. (a) X-ray diffraction pattern for $URu_{2-x}Fe_xSi_2$ with Fe concentration x = 0.1. Black dots represent the data, and the red solid line is the fit to the data. (b) Lattice parameters a and c vs. nominal Fe concentration x. (c) Unit cell volume V vs. x. For the axis on the right side the unit cell volume was converted to chemical pressure (see text, section 5.3) (d) Fe concentration $x_{\rm meas}$, determined from EDX measurements, vs. x. The shaded region is the error in $x_{\rm meas}$ due the accuracy of the EDX measurement.

4.2.2 Electrical resistivity

The measurements of the electrical resistivity ρ further emphasize that polycrystalline samples of high quality have been obtained. The residual resistivity ratio (RRR), defined as ρ(300 K)$/\rho$(2 K), for the pure URu$_2$Si$_2$ and UFe$_2$Si$_2$ samples are 100 and 220, respectively. For increasing Fe concentration x, however, the RRR drops rapidly to approximately 5, presumably due to the disorder introduced by the Fe substitution.

The superconducting critical temperature T_{sc} is rapidly suppressed by Fe substitution and SC is not observed for $x \gtrsim$ 0.075 down to 50 mK. As illustrated in Fig. 4.2, the transition at $T_0(x)$ into the HO in URu$_{2-x}$Fe$_x$Si$_2$ is visible as a small peak in $\rho(T)$ or, alternatively, an inflection point in $d\rho/dT$. $T_0(x)$ increases with x from 17.5 K at x = 0 to a maximum value of 42 K at $x \approx$ 0.8. We note, that, as will be discussed in more detail in section 5.3 of the manuscript, our data indicates a phase transition from the HO into the LMAFM phase at $x \approx$ 0.2. For $x >$ 0.8, $T_0(x)$ decreases with x and disappears at $x \approx$ 1.3. Additionally, starting from $x =$ 0.075, the peak in $\rho(T)$ that we associate with T_0 begins to broaden significantly. This broadening is more clearly visible in $d\rho/dT$ as shown in Fig. 4.2(e). We have identified the onset of the transition to the HO phase, T_0', as the upper inflection point in $d\rho/dT$ as marked with the empty arrows. Starting from $x =$ 0.8, $\rho(T)$ also develops a low T minimum that "tracks" T_0, where the corresponding low T upturn of ρ is most pronounced for $x =$ 1 and disappears when T_0 is suppressed to zero for $x \rightarrow$ 1.3 (Fig. 4.2(c+f)).

4.2.3 Magnetization

The HO transition in $M(T)$ is manifested as a change of slope (Fig. 4.3(a)) that closely tracks $T_0(x)$, as observed in $\rho(T)$. Alternatively, the HO transition can be identified as a peak in dM/dT (Fig. 4.3(b)). The signature of the onset of the HO at T_0' in $M(T)$ is weak and only discernible for $x =$ 0.60 as a small kink that appears as an inflection point in dM/dT. A low T upturn is observed in $M(T)$ for $x \leq$ 1.0 and $T <$ 5 K, which becomes more pronounced for $x \geq$ 1.0 as it moves to higher T.

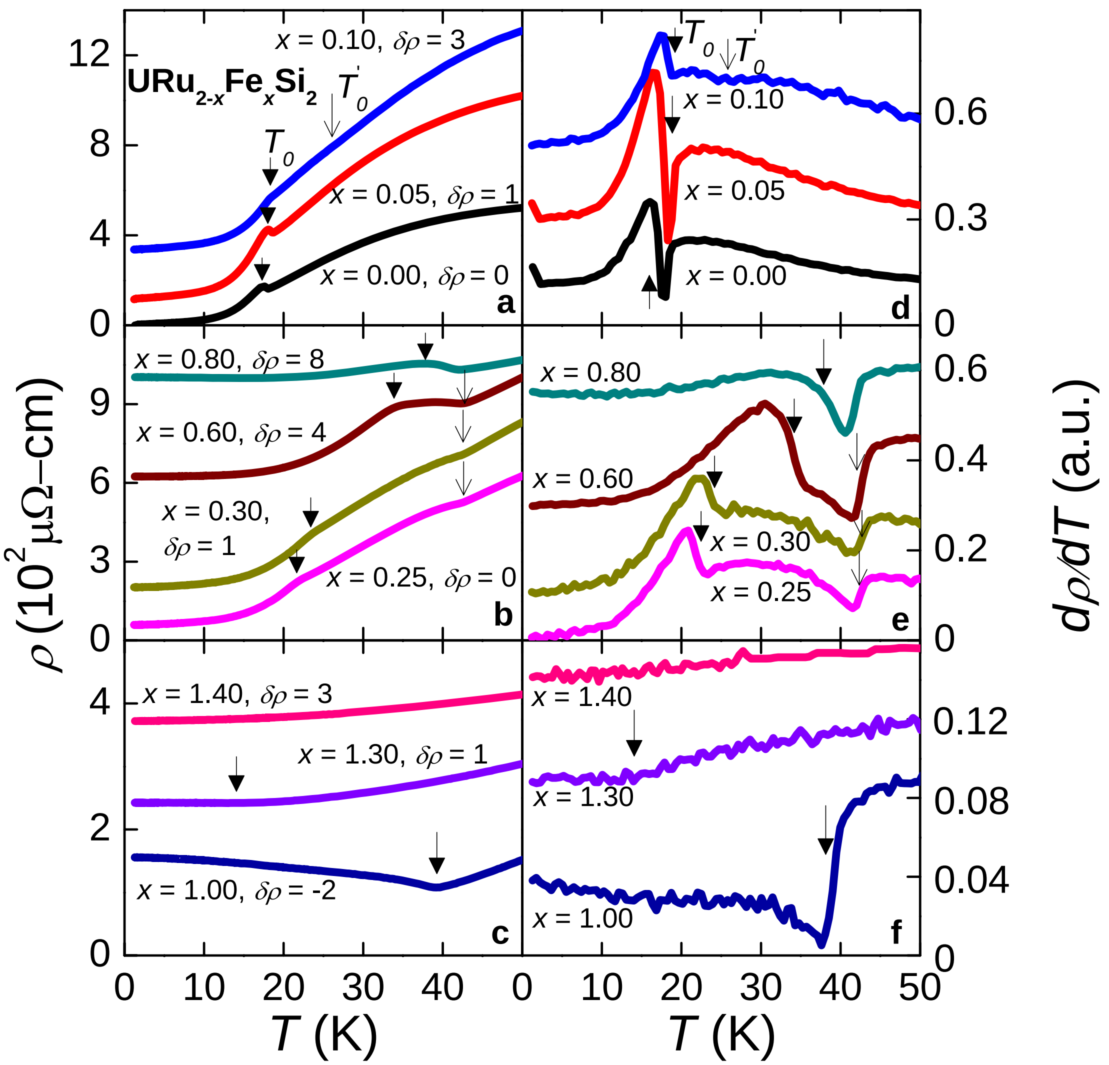

Figure 4.2: (a-c) Electrical resistivity ρ vs. temperature T for URu$_{2-x}$Fe$_x$Si$_2$. For clarity of presentation, only selected values of x are shown. Each data set is shifted by $\delta\rho$, the values of which are indicated in the figure. (d-f) Derivative of ρ with respect to T, $d\rho/dT$, vs. T. T_0 marks the transition to the HO/LMAFM phases and T_0' is the onset of the transition (see text).

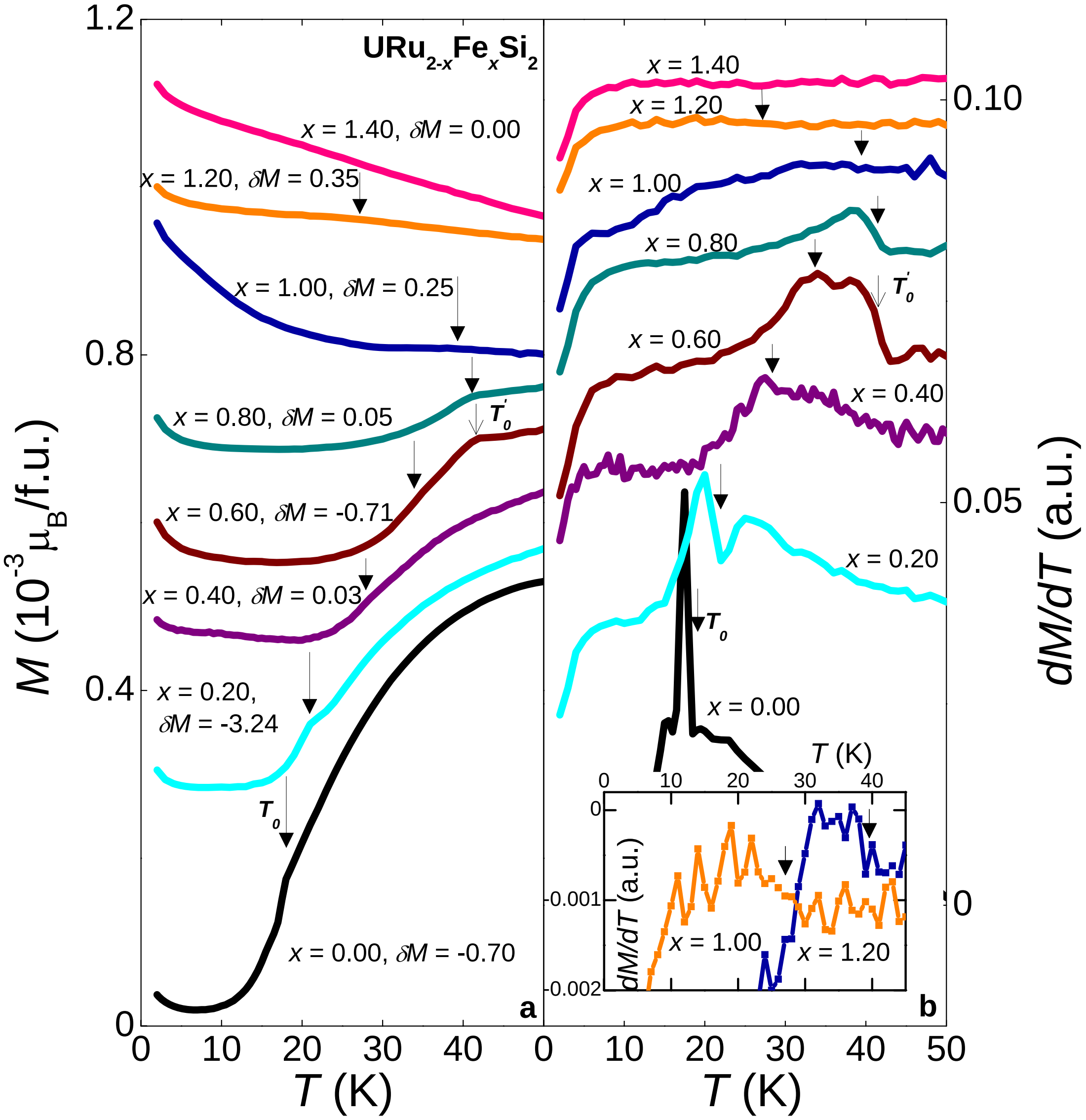

Figure 4.3: (a) Magnetization M vs. temperature T for URu$_{2-x}$Fe$_x$Si$_2$ in a magnetic field H = 0.1 T. For clarity of presentation, only selected values of x are shown. Each data set is shifted by δM, the values of which are indicated in the figure. (b) Derivative of M with respect to T, dM/dT, vs. T. T_0 and T_0' are the ordering temperature and the onset to the hidden order (see text), respectively. Inset: Detail of dM/dT for x = 1.0 and 1.2.

4.2.4 Specific heat

In Fig. 4.4, we show the electronic specific heat $C_e(T)$ that was determined for all x by subtracting the phonon contribution $C_{ph}(T)$ of $\mathrm{UFe_2Si_2}$. This method should yield a good estimate of the phonon contribution for all values of x, since the end member compounds are isostructural, and $\mathrm{UFe_2Si_2}$ is reported to be a Pauli paramagnet down to 0.2 K.[88] Using only a Debye function, we were not able to account correctly for the phonon contribution over the entire T-range measured.

For $\mathrm{URu_2Si_2}$, the HO transition appears in $C_e(T)/T$ as a jump at T_0 whose shape is reminiscent of a second-order BCS-type mean-field transition. With increasing x, this anomaly moves to higher temperatures, while the size of the jump $\Delta C_e/T$ decreases and disappears at $x \approx 0.8$. In agreement with $\rho(T)$ and $M(T)$ results, the transition broadens significantly, leading to a shoulder in the $C(T)$ peak for x ≥ 0.075. Here, we define the shoulder at T_0' as the onset of the transition to the HO and LMAFM phases, respectively.

4.3 Discussion

4.3.1 Phase diagram and HO-LMAFM phase transition

In Fig. 4.5(a), we have summarized the results of the $\rho(T)$, $M(T)$, and $C(T)$ measurements discussed in the previous section in a phase diagram showing the HO transition temperature T_0 vs. Fe concentration x. $T_0(x)$ increases linearly with x from 17.5 K at x = 0 to 21 K at $x \approx 0.2$, exhibits a kink at $x \approx 0.2$, and then increases linearly with a larger slope to a maximum value of 42 K at $x \approx 0.8$; thereafter, $T_0(x)$ decreases with x and vanishes at $x \approx 1.3$. This behavior is quite reminiscent of the T vs P phase diagram observed for $\mathrm{URu_2Si_2}$. Due to the differences in the atomic radii, substitution of isoelectronic ions often induces a change in the unit cell volume that may be interpreted as a “chemical pressure” P_{ch}. The linear decrease of the unit cell volume of $\mathrm{URu_{2-x}Fe_xSi_2}$ with increasing Fe concentration x (see Fig. 4.1(c)) established by our XRD analysis is consistent with that view. We have therefore used the variation of the unit cell volume with x to estimate the value of P_{ch} corresponding to each concentration

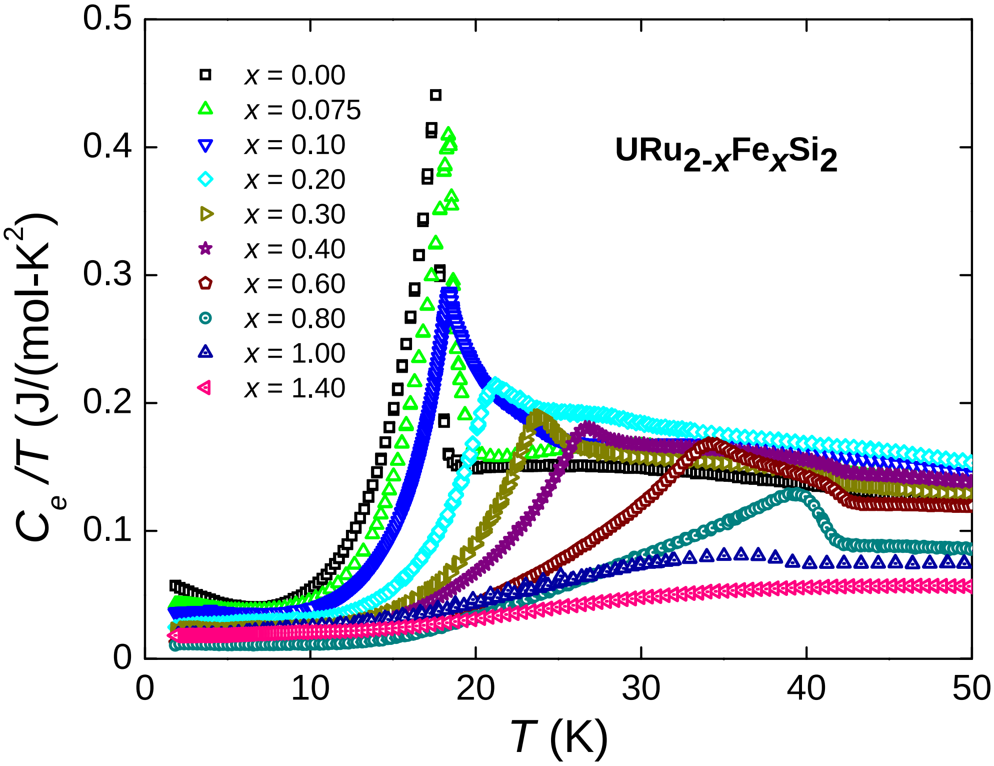

Figure 4.4: Electronic specific heat C_e divided by temperature T vs. T for $\mathrm{URu}_{2-x}\mathrm{Fe}_x\mathrm{Si}_2$. For clarity of presentation, only selected values of x are shown.

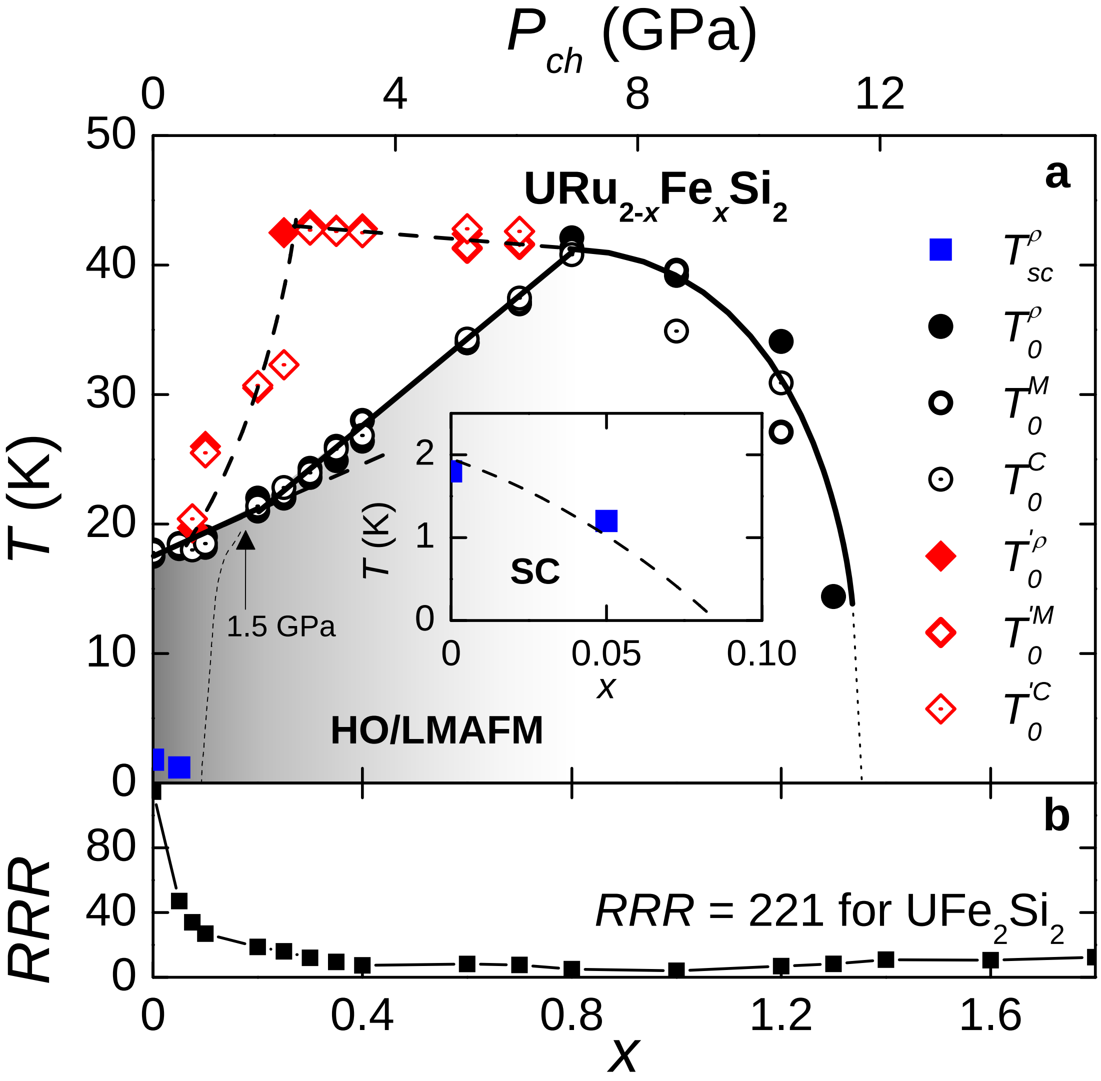

Figure 4.5: (a) Temperature T vs. Fe concentration x phase diagram of $\mathrm{URu_{2-x}Fe_xSi_2}$, constructed from electrical resistivity (ρ, filled symbols), specific heat (C, empty-dotted symbols), and magnetization (M, empty symbols) measurements. The $T - x$ phase boundary $T_0(x)$ (solid black line) separates the ordered phases (HO and LMAFM) from the paramagnetic phase. The superconducting critical temperature T_{sc} and the transition temperature T_0 and onset temperature T_0'(see text) of the ordered phases are denoted by blue squares, black circles, and red diamonds, respectively. The dashed bold line is an extrapolation of $T_0(x)$ to emphasize the kink at $x \approx 0.2$. The Fe concentration x was converted to "chemical pressure" P_{ch} on the top horizontal axis (see text). The thin dashed line is the HO-LMAFM transition in $\mathrm{URu_2Si_2}$ as observed under pressure.[89] The inset highlights the region around the superconducting phase. (b) Residual resistivity ratio RRR, defined as ρ(300 K)/ρ(2 K), vs. x.

x according to the isothermal compressibility $\kappa_T = 5.2{\cdot}10^{-3}$ GPa^{-1} of URu$_2$Si$_2$ [90] (see right axis of Fig. 4.1(c) and top horizontal axis in Fig. 4.5(a)). We note, however, that the conversion depends on the value chosen for κ_T, and that literature values vary from $2{\cdot}10^{-3}$ GPa^{-1} to $7.3{\cdot}10^{-3}$ GPa^{-1} ([22, 23, 90, 91, 92]). It is interesting that the kink in the $T - P_{ch}$ phase boundary $T_0(P_{ch})$ at 1.5 GPa and the slopes of $T_0(P_{ch})$ of 2.1 K/GPa and 3.9 K/GPa below and above the kink are consistent with the values of the $T - P$ phase boundary $T_0(P)$ of pure URu$_2$Si$_2$ (1.3 and 3.8 K/GPa, respectively), where the kink occurs at the transition between the HO and LMAFM phases. This similarity suggests that the kink in $T_0(P_{ch})$ (and, in turn, $T_0(x)$) is associated with a transition from the HO to the LMAFM phase as indicated by the thin dashed line in Fig. 4.5(a) that marks the HO-LMAFM transition in URu$_2$Si$_2$, according to recent neutron scattering studies under pressure.[89] In addition, the chemical pressure $P_{ch} \approx 0.8$ GPa at which SC is suppressed to zero agrees well with previous high pressure studies,[89] while the maximum value of $T_0 \approx 42$ K and the value of $P_{ch} \approx$ 7-8 GPa at which it occurs, are consistent with the high pressure study of URu$_2$Si$_2$ by Iki et al.[93]

The low T upturns that are observed in $\rho(T)$ and $M(T)$ for $x \rightarrow 1.3$ where T_0 is suppressed to zero (Fig. 4.2(c+f) and Fig. 4.3) are reminiscent of the quantum critical scenario recently reported for chromium where spin density wave order breaks down at the critical pressure P_c = 9.71 GPa.[94] This suggests that a quantum critical point (QCP) may be located at $x \approx 1.3$ in URu$_{2-x}$Fe$_x$Si$_2$ due to suppression of the LMAFM phase.

The established T vs. P_{ch} phase diagram also offers an explanation for the broadening of the HO transition that is mainly manifested in the $\rho(T)$ and $C_e(T)$ data. We believe that the broadening of the transition is due to small Fe concentration inhomogeneities that may generate appreciable internal strain. From high pressure studies on URu$_2$Si$_2$, it is known that the HO transition is very sensitive to strain [21, 89]. This scenario is corroborated by the residual resistivity ratio RRR that drops rapidly with increasing x from 100 at $x = 0$, and then levels off at $x = 0.075$ where the broadening of the HO transition first appears, indicating additional scattering due to disorder (Fig. 4.5(b)). It is noteworthy that the value of T_0' saturates rapidly at $\sim$42 K corresponding to the maximum of $T_0(x)$. Accordingly, the width of the transition again decreases when T_0 reaches its maximum at $x = 0.8$. The weak signature of the onset of the HO/LMAFM phases, T_0', in the $M(T)$ measurements indicates that the inhomogeneous regions occupy only a small volume fraction, as further corroborated by XRD and EDX measurements, which show that the samples are formed with the correct composition. We therefore attribute the broadening of the transition to the extreme sensitivity of $\mathrm{URu_2Si_2}$ to strain [21, 89]. Preliminary results on single crystals of $\mathrm{URu_{2-x}Fe_xSi_2}$ show no broadening of the transition, supporting this interpretation.

4.3.2 Stabilization of the HO phase

In order to investigate the stabilization of the HO phase by the substitution of Fe with Ru, manifested in the increase of T_0 with x, in more detail, we have performed fits of relevant theoretical models to the features in $\rho(T)$ and $C_e(T)$ that characterize the HO phase. As demonstrated for $\mathrm{URu_2Si_2}$ at ambient pressure,[95] under pressure,[96] and substituted with other elements,[97] $\rho(T)$ in the HO phase is well described by the expression

$$\rho(T) = \rho_0 + AT^2 + B\Delta T \left(1 + 2\frac{T}{\Delta}\right) e^{-\frac{\Delta}{T}}, \tag{4.1}$$

which includes the residual resistivity ρ_0, a Fermi liquid term AT^2, and an electron-magnon scattering contribution due to spin excitations with an energy gap Δ. We note, however, that some ambiguity about the expression used to describe the electrical resistivity in the HO phase exists in the literature. Eq. 4.1 was originally derived to describe electron-magnon scattering due to ferromagnetic magnons [98]. However, the magnons observed in $\mathrm{URu_2Si_2}$ are of antiferromagnetic nature and the following expression should, in principle, be used to fit the electrical resistivity [99]:

$$\rho(T) = \rho_0 \ + \ AT^2 + B\Delta^2\sqrt{\frac{T}{\Delta}}\left[1 + \frac{2}{3}\left(\frac{T}{\Delta}\right) + \frac{2}{15}\left(\frac{T}{\Delta}\right)^2\right] e^{-\frac{\Delta}{T}}. \tag{4.2}$$

The resulting fits of $\rho(T)$ using Eq. 4.2 are shown in Fig. 4.6(a-c). The differences in the values extracted for Δ via fits to the low temperature $\rho(T)$ data of Eqs. 4.1 and 4.2, respectively, are small because the exponential term that contains the gap Δ is the dom-

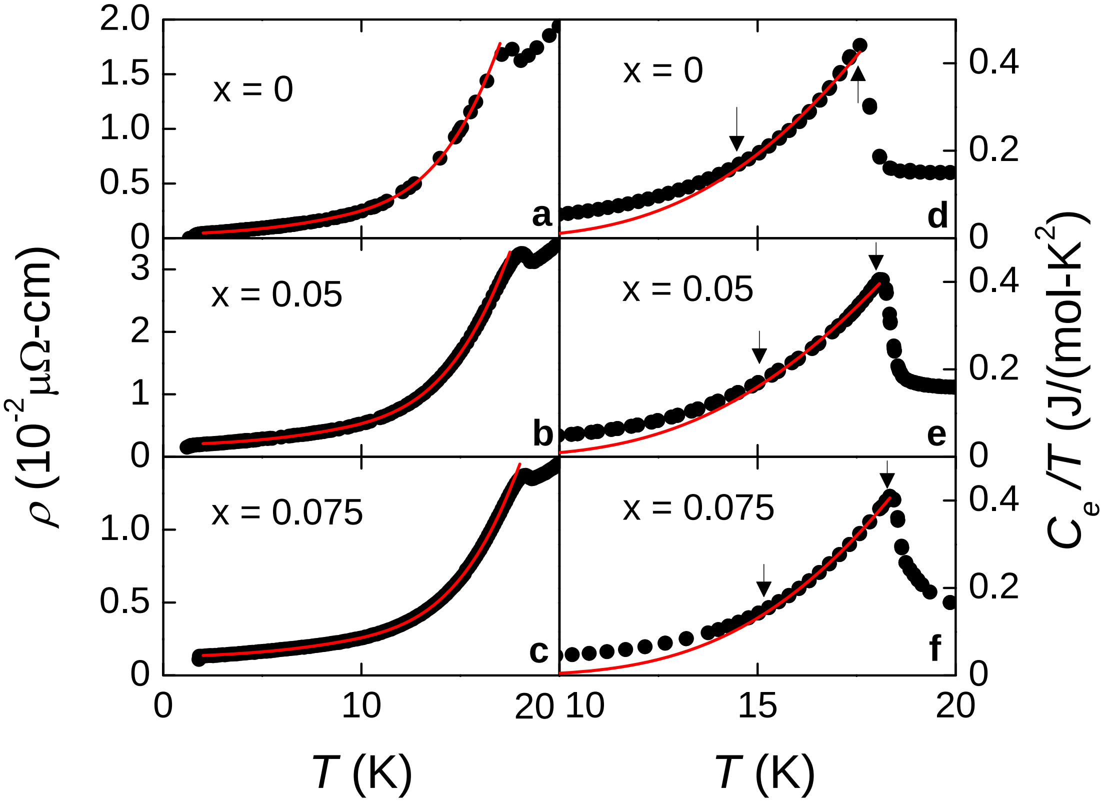

Figure 4.6: Fits of the low temperature electrical resistivity $\rho(T)$ and electronic specific heat $C_e(T)$ to a theoretical model with gapped magnetic excitations (see text) for several Fe concentrations x. In the HO phase, the $\rho(T)$ data (a-c) have been fitted using Eq. 4.2 whereas the $C_e(T)$ data (d-f) have been fitted using Eq. 4.3. Black circles represent the data, red solid lines the resulting fits, and arrows the fitting ranges.

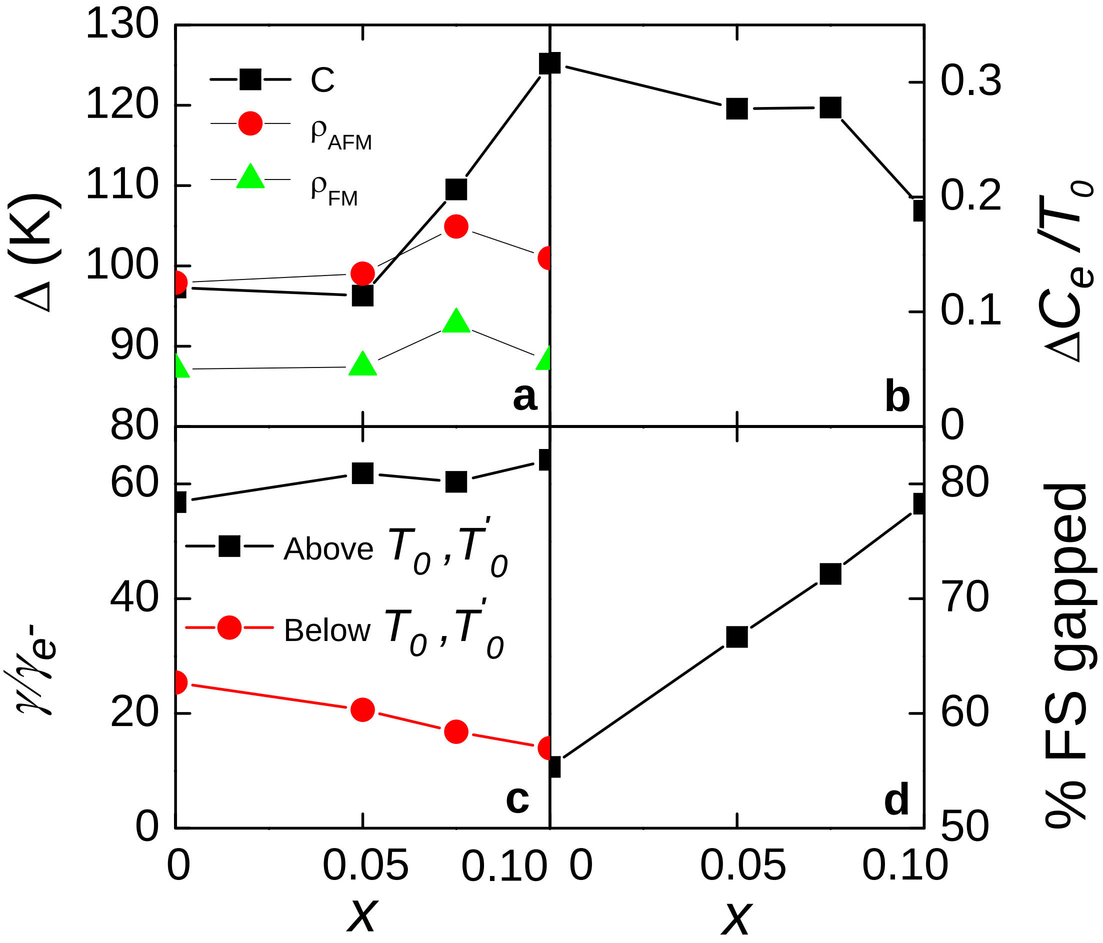

Figure 4.7: (a) Energy gap Δ that opens on the FS due to the onset of the hidden order (HO) phase as determined via fits to the low temperature electrical resistivity $\rho(T)$ (red circles and green triangles corresponding to a theoretical model with gapped antiferromagnetic and ferromagnetic excitations, respectively; see text) and electronic specific heat $C_e(T)$ (black squares), vs. x (see text and Fig. 4.6). (b) Jump in C_e at the transition to the hidden order (HO) phase divided by T_0, $\Delta C_e/T_0$, vs. Fe concentration x. (c) Ratio of measured and calculated free electronic specific-heat coefficients γ and γ_{e^-} vs. x for T above and below T_0 (and T_0'), respectively. (d) Fraction of the FS that is gapped below the HO transition vs. x.

inant term in both expressions, and thus qualitatively identical behavior is observed. In order to facilitate the comparison to previously published data, we provide the values of Δ derived from both expressions in Fig. 4.7(a). We emphasize that the values for Δ extracted by means of Eq. 4.2 also match much better with the values for the gap obtained from fits of the low temperature specific heat (see below and Fig. 4.7(a)). Since for $x > 0.1$, the low temperature electrical resistivity flattens considerably, it becomes unreasonable to describe the $\rho(T)$ data with both the Fermi liquid and exponential contributions; therefore, we have limited the fits to the $\rho(T)$ data for $x \leq 0.1$. The extracted size of the HO gap increases moderately with increasing x up to $x = 0.075$, after which it saturates again (Fig. 4.7(a)), suggesting that the HO phase is at least initially stabilized by introducing Fe into URu_2Si_2.

Below the HO transition, the $C_e(T)$ data can be described by the expresssion

$$C_e(T) = A\exp(-\Delta/T), \tag{4.3}$$

where Δ is the gap that opens over the FS [18]. The fits of Eq. 4.3 to the $C_e(T)$ data are displayed in Fig. 4.6(d-f) in the form of $C_e(T)/T\ vs.\ T$ plots. Since the shape of the HO anomaly in C/T deviates increasingly from a BCS form with increasing x, we have limited this analysis to $x \leq 0.1$, as well. As indicated in Fig. 4.7(a), the size of Δ increases with increasing x. At the same time, the jump in C_e at the transition to the HO phase divided by T_0 remains approximately constant with increasing x and only decreases significantly for $x \geq 0.1$. In order to approximate the fraction of the FS that is gapped, we have estimated the electronic specific-heat coefficient γ_n by linearly extrapolating C_e/T from above T_0 and T_0' to $T = 0$, and, accordingly, γ_0 for the gapped FS by linearly extrapolating the C_e/T data from below the transition to $T = 0$, following the method described in [18] In Fig. 4.7(c), both γ_n and γ_0 are compared to γ_{e^-} for the ungapped state, calculated for conduction electrons with the free electron mass. At $x = 0$, we find that 55% of the FS is gapped, in agreement with previous reports.[18] With increasing x, γ_n increases, whereas γ_0 decreases, leading to an increase of the fraction of the FS that is gapped, which at $x = 0.1$ reaches a value of 0.8 (Fig. 4.7(d)). It is noteworthy that the change of shape of the HO anomaly occurs at $x = 0.2$, where $T_0(x)$ exhibits a kink. In addition, extrapolating the fraction of the FS that is gapped to higher values of x suggests that the FS will be entirely gapped at $x \approx 0.2$.

To further elucidate this point, we have calculated the entropy for $URu_{2-x}Fe_xSi_2$as a function of x. Shown in Fig. 4.8 is the difference of entropy between the normal state and the hidden order state ΔS vs. x. Here, the entropy of the normal state was estimated by linearly extrapolating C_e/T from above the HO transition to zero and computing the area below that line, whereas the entropy in the HO state was calculated by integrating C_e/T up to T_0. ΔS peaks at $x = 0.2$, demonstrating that the largest amount of entropy is removed from the system due to onset of the HO phase for $x = 0.2$, again indicating that the HO state is stabilized with increasing Fe concentration for $0 \leq x \ \leq 0.2$. The decrease in ΔS for $x > 0.2$ provides further support for the possibility of a transition from the HO to LMAFM state at $x = 0.2$.

4.4 Conclusions

In summary, we have established the phase diagram for $URu_{2-x}Fe_xSi_2$ over the entire range of Fe compositions from x = 0 to 2 (Fig. 4.5). Particularly noteworthy is a more than two-fold increase of T_0 from 17.5 K at $x = 0$ to 42 K at $x = 0.8$. Here the striking similarities of the effect of "chemical pressure" and external pressure on URu_2Si_2 suggest that for $x \geq 0.2$ (corresponding to $P_{ch} = 1.5$ GPa), $T_0(x)$ marks the phase boundary to an ordered phase that is different from the HO phase and is presumably similar to the LMAFM phase identified in URu_2Si_2 for pressures $P \geq 1.5$ GPa. However, in the experiments reported herein, it was not possible to determine the phase boundary between the HO and LMAFM phases in the ordered region of the phase diagram. This will require neutron diffraction measurements that are able to determine the magnetic structure and ordered magnetic moment as a function of Fe concentration x. Both the electrical-resistivity and the specific heat results demonstrate that, at least up to $x = 0.1$, the HO is further stabilized as indicated by the increasing size of both the HO gap and the fraction of gapped FS. Furthermore, circumstantial evidence suggests that the HO is stabilized against thermal fluctuations even up to $x \approx 0.2$: (1) the shape of the T_0-anomaly in the specific heat changes at x = 0.2, (2) the extrapolated gapped fraction of the FS approaches 1 as $x \rightarrow 0.2$, (3) the difference of entropy between the normal

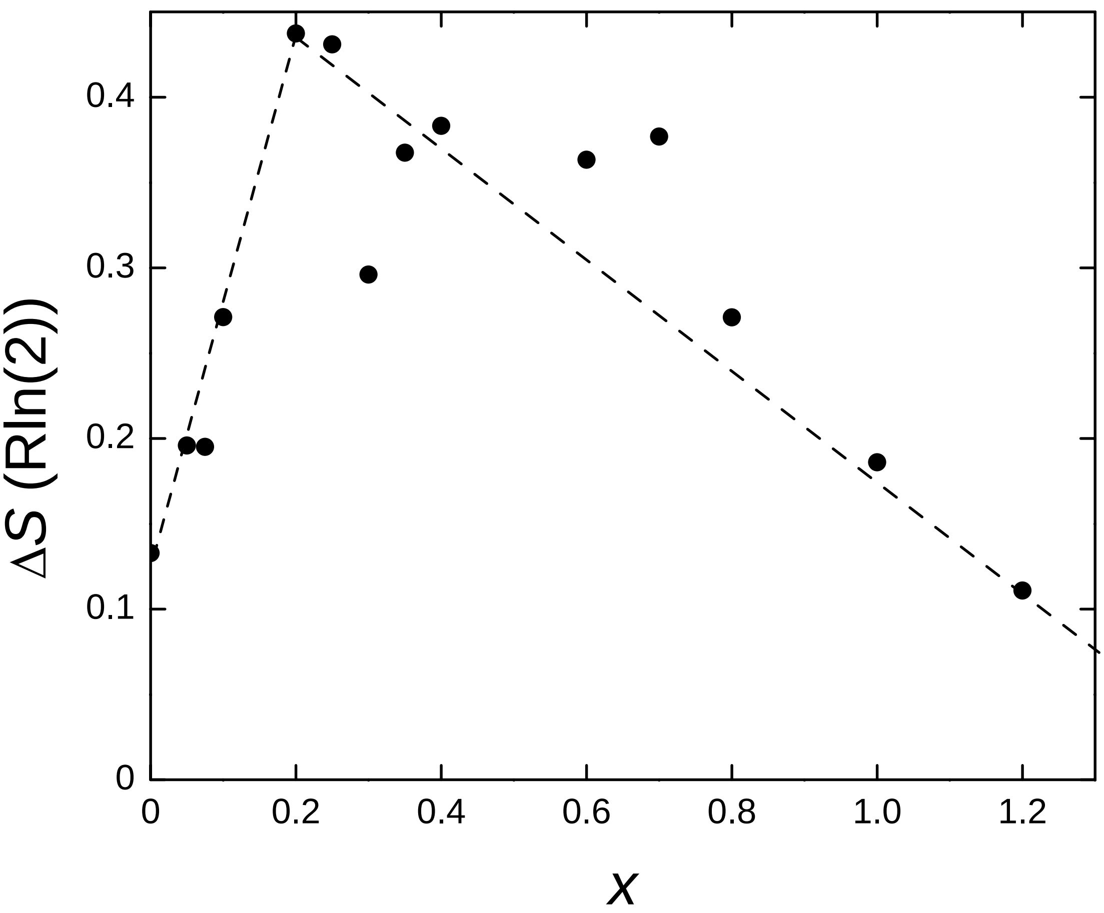

Figure 4.8: The difference in entropy between the normal state and the hidden order state ΔS vs. Fe concentration x.

state and the HO state ΔS peaks at $x = 0.2$, and (4) the similarity of $T_0(P_{ch})$ and $T_0(P)$, in conjunction with the kink in $T_0(x)$ at $x = 0.2$, indicates that the HO phase extends to $x = 0.2$. We note that the application of "chemical pressure" to URu_2Si_2 extends the range of experiments that may be used to study the HO to methods, such as STM, ARPES and PCS, that are generally not available in combination with applied pressure, but hold the promise of new insights into the HO. In particular, this will be important for testing models for the HO based on an itinerant OP such as the recently proposed hybridization wave [63, 74]. We note, however, that high quality single crystals are required for these experiments. Using single crystal samples will also mitigate the problem of disorder that is observed for increasing Fe concentrations, thereby reducing the broadening of the HO transition. This has been verified with preliminary experiments on single crystals of $URu_{2-x}Fe_xSi_2$ that will be published elsewhere. Finally, the apparent QCP that is indicated by low temperature divergences in the electrical resistivity and magnetization at x = 1.3, where T_0 extrapolates to zero, may also shed some light onto the delicate interplay between HO and the LMAFM phase.

A portion of the text and data presented in this chapter are reprints of material that appears in "Two-fold enhancement of the "hidden order"/large moment antiferromagnetic phase boundary in the $\mathrm{URu}_{2-x}\mathrm{Fe}_x\mathrm{Si}_2$ system", N. Kanchanavatee, M. Janoschek, R. E. Baumbach, J. J. Hamlin, D. A. Zocco, K. Huang, and M. B. Maple, Phys. Rev. B 84, 245122 (2011). The dissertation author was the first author of the article.

Chapter 5

$\mathbf{URu}_{2-x}\mathbf{Os}_x\mathbf{Si}_2$

5.1 Introduction

Several novel electronic ground states can emerge from the hybridization between localized d- or f-electron states and conduction electron states. The heavy fermion compound URu_2Si_2 exhibits two of such ground states: the hidden order at T_0 = 17.5 K and superconductivity (SC) at T_{sc} = 1.5 K [17, 18, 19]. The term HO was adapted for the unknown phase displaying a mean-field like transition in specific heat. The entropy lost due to the transition is approximately 0.2Rln2 [18], which indicates a large magnetic moment should be observed in neutron scattering experiments. However, only a 0.03 μ_B/U antiferromagnetic moment was detected [20, 21].

For nearly three decades, the search for the order parameter of the HO phase has driven numerous research studies on this topic. Control parameters, such as pressure P, magnetic field H, and chemical substitution x have been tuned to gather information about the electronic ground state. Upon applying pressure P, T_0 slightly increases, and at critical pressures $P_c \geq$ 0.5-1.5 GPa, a large moment antiferromagnetic phase was observed [89]. The magnetic structure in this phase is identical to that of the LMAFM phase, and the transition is believed to be first order [79]. Thus, it is widely accepted that the magnetic order in the HO phase is extrinsically triggered by strain in a small fraction of the LMAFM phase, and that the LMAFM is caused by a stress field increasing the c/a ratio over a critical value [100]. Alternatively, the small moment in the HO phase might be intrinsic since its onset temperature coincides with that of the HO, and the moment is still detectable in samples with different residual resistivities [80]. Through the application of magnetic field H, HO is suppressed at 35.9 T [81]. Several novel phases exhibiting NFL behavior emerge at higher fields. Substitution of most elements bordering Ru in the periodic table for Ru leads to suppression of the HO, and results in other magnetic phases [82]; a LMAFM phase results from Rh substitution [83], and an itinerant ferromagnetic phase arises with Mn, Tc, and Re substitution [84, 85]. On the other hand, an enhancement of the HO transition temperature was found with Fe and Os substitution [82, 101]. For Fe substitution, it is believed that the HO phase is enhanced by the "chemical pressure" generated by substitution of smaller Fe ions into Ru ions. Nevertheless, in a low Os concentration substitution study, it was found that the HO is still enhanced even when Ru is replaced by larger Os ions. This raises an intriguing question: how might the HO be enhanced without chemical pressure? By substituting higher concentration of Os, we might be able to shed some light on this long-lasting problem. In this chapter, results from x-ray, electrical resistivity ρ, magnetization M, and specific heat C measurements are discussed.

5.2 Results

5.2.1 Crystal structure and sample quality

UOs_2Si_2 is isostructural with URu_2Si_2 (space group $I4/mmm$) and, correspondingly, we find that samples with the $0 \leq x \leq 1.2$ range of Os substitutions can be described by the same space group, though there might be a miscibility gap between $1.2 \leq x < 2$. The typical goodness of fit extracted from the Rietveld refinement, characterized by χ^2, ranged from 5 to 15; Fig. 5.1 illustrates the quality of the refinement that was typically achieved. As shown in Fig. 5.2, the lattice parameter a decreases while c increases with increasing Os concentration. The decrease of a is much smaller in overall magnitude than the increase of c. Hence, the ratio between lattice constants c and a increases with x (Fig. 5.3). Overall, the unit cell volume of $URu_{2-x}Os_xSi_2$ increases with x (Fig. 5.4), as expected from the larger size of Os relative to Ru ions.

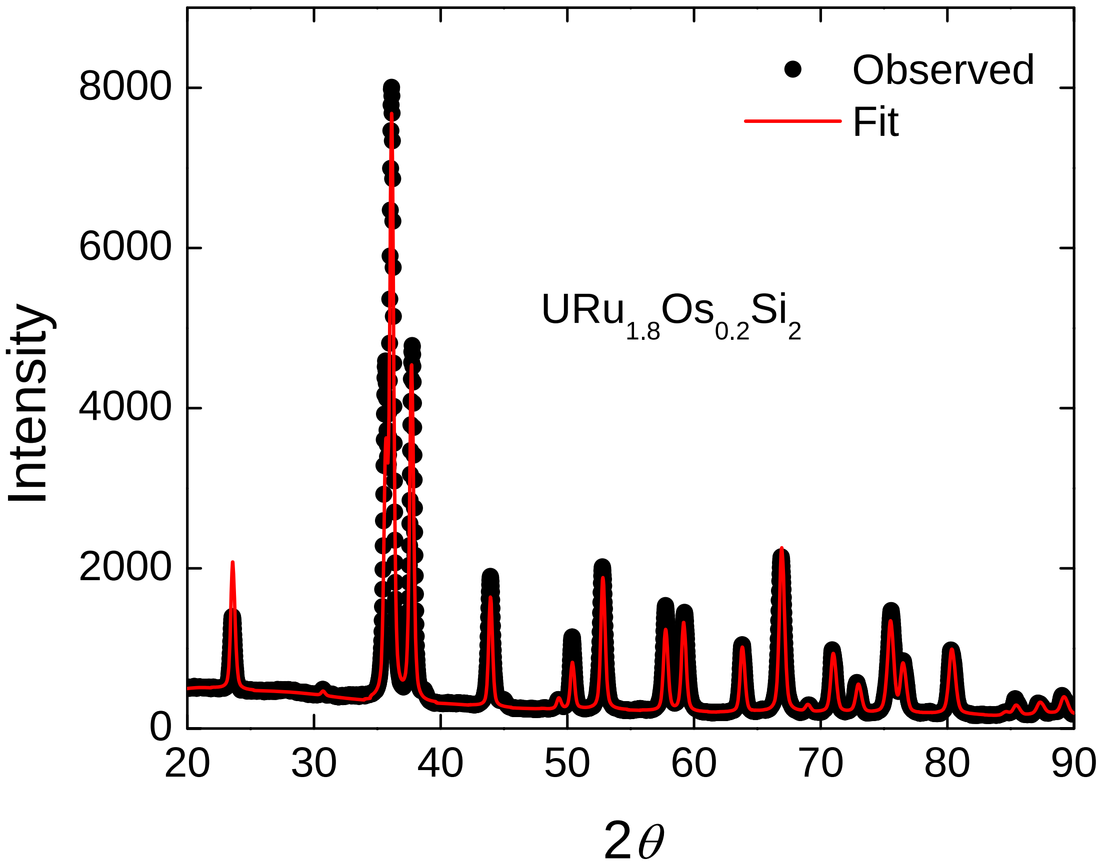

Figure 5.1: X-ray diffraction pattern for $URu_{1.8}Os_{0.2}Si_2$. Black dots represent the data, and the red solid line is the fit to the data.

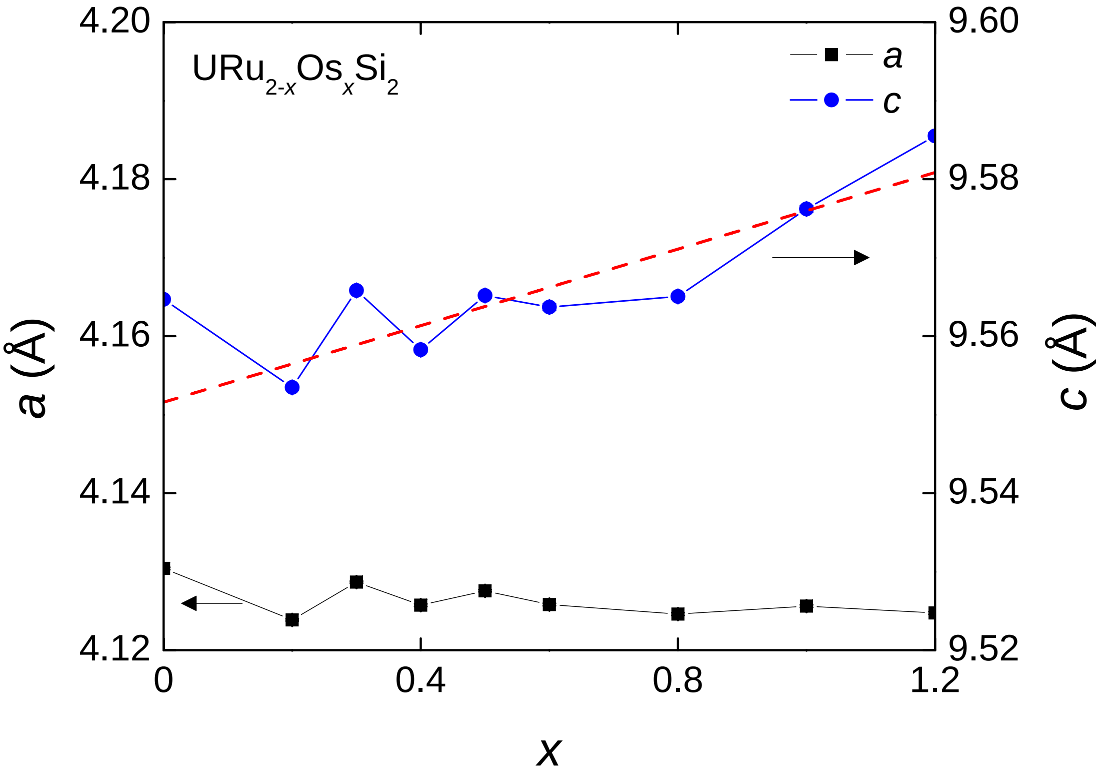

Figure 5.2: Lattice parameters a and c vs. Os concentration x.

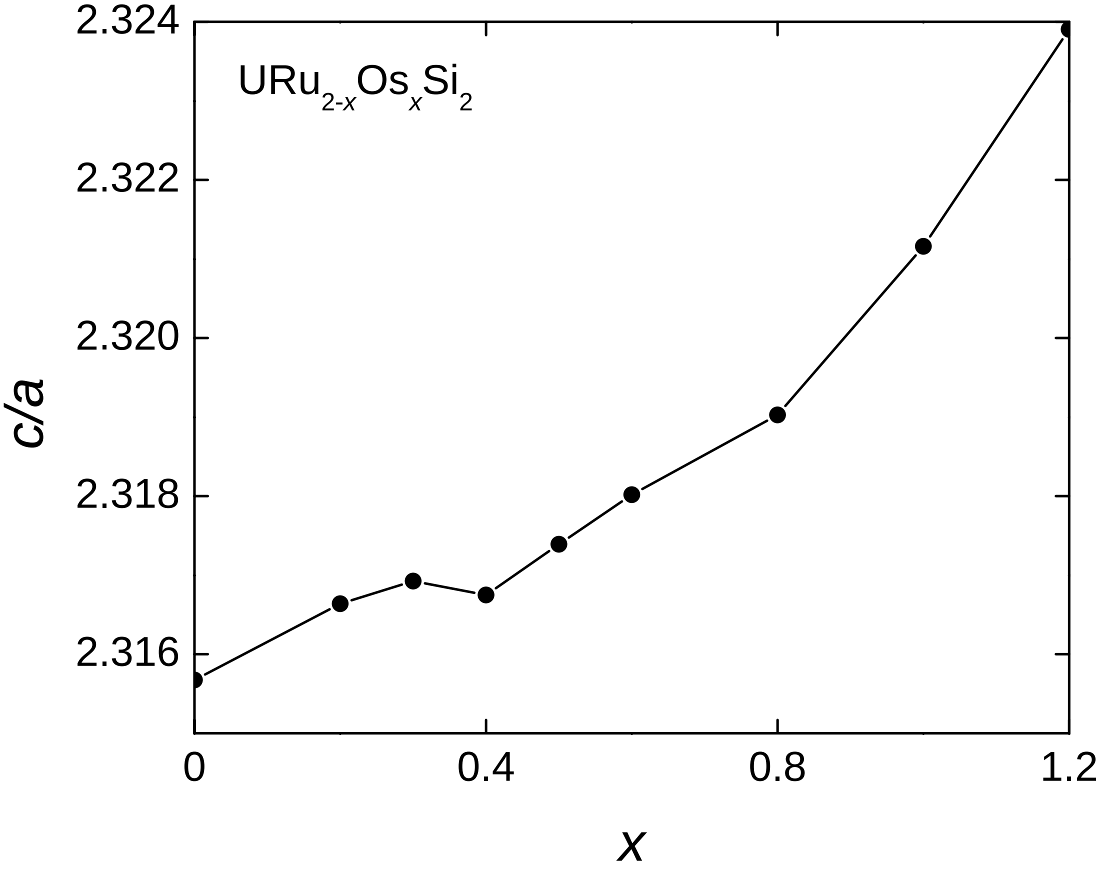

Figure 5.3: Ratio c/a vs. Os concentration x.

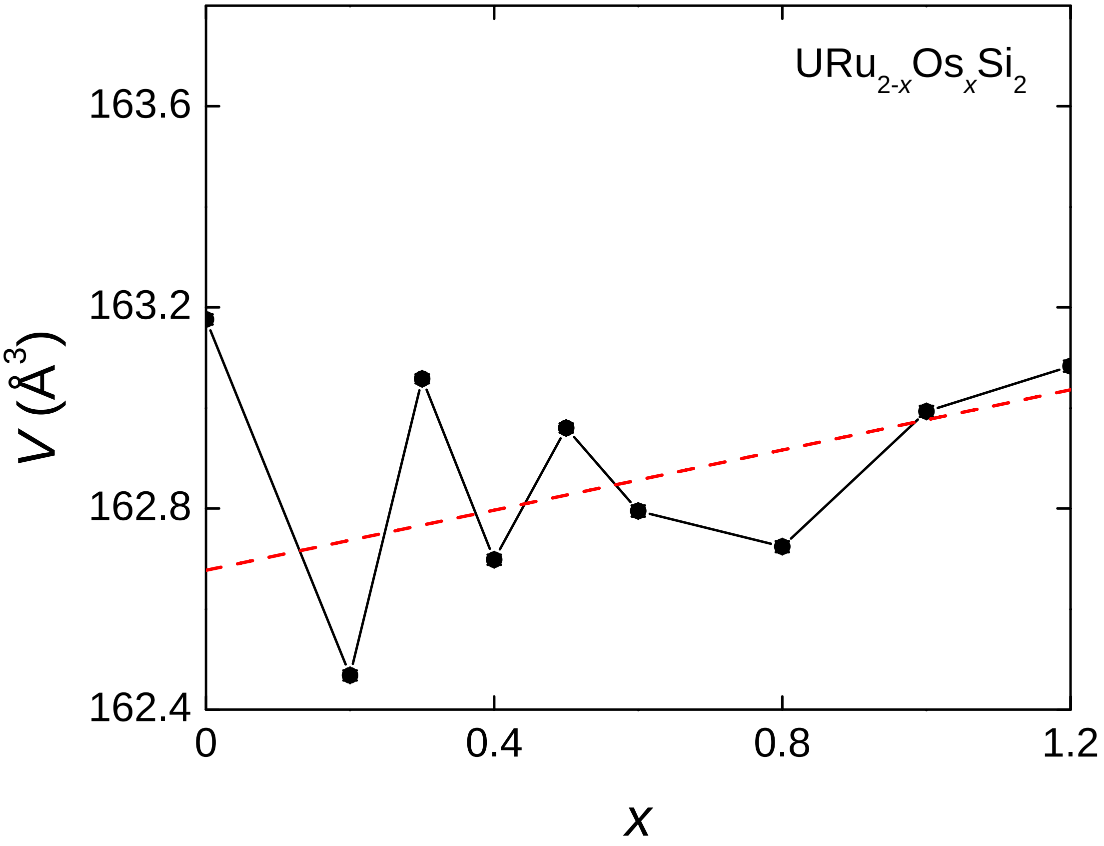

Figure 5.4: Unit cell volume V vs. Os concentration x.

5.2.2 Electrical Resistivity

From the substitution study with low Os concentration [82], the superconducting critical temperature T_{sc} is rapidly suppressed by Os substitution and SC is not observed for $x \gtrsim$ 0.05 down to 70 mK. As illustrated in Fig. 5.5(a), the transition at $T_0(x)$ into the HO phase in $URu_{2-x}Os_xSi_2$ is visible as a midpoint between a maximum and a minimum in $\rho(T)$ or, alternatively, a minimum in $d\rho/dT$ (Fig. 5.5(b)). $T_0(x)$ increases with x from 17.5 K at x = 0 to a maximum value of 50 K at $x \approx$ 1. We note, that, as is discussed in more detail in section 5.3 of the manuscript, our data indicates a possible phase transition from the HO phase to another order phase at $x \approx$ 0.2.

5.2.3 Magnetization

The HO transition in $M(T)$ is manifested as a change of slope (Fig. 5.6(a)) that closely tracks $T_0(x)$, as observed in $\rho(T)$. Alternatively, the HO transition can be identified as a peak in dM/dT (Fig. 5.6(b)). A low T upturn is observed in $M(T)$ for all x, which becomes more pronounced with increasing x as it moves to higher T.

5.2.4 Specific heat

In Fig. 5.7, we show the electronic specific heat $C_e(T)$ that was determined for all x by subtracting the phonon contribution $C_{ph}(T)$ of UOs_2Si_2. This method should yield a good estimate of the phonon contribution for all values of x, since the end member compounds are isostructural, and UOs_2Si_2 is reported to be a Pauli paramagnet down to 1.5 K [102]. Using only a Debye function, we were not able to account correctly for the phonon contribution over the entire T-range measured.

For URu_2Si_2, the HO transition appears in $C_e(T)/T$ as a jump at T_0 whose shape is reminiscent of a second-order BCS-type mean-field transition. With increasing x, this anomaly moves to higher temperatures, while the size of the jump $\Delta C_e/T_0$ decreases rapidly from x = 0 to x = 0.2, and slightly drops above that concentration. For samples wtih $x > 0$, the transition broadens and the shape is distinguishable from that of URu_2Si_2.

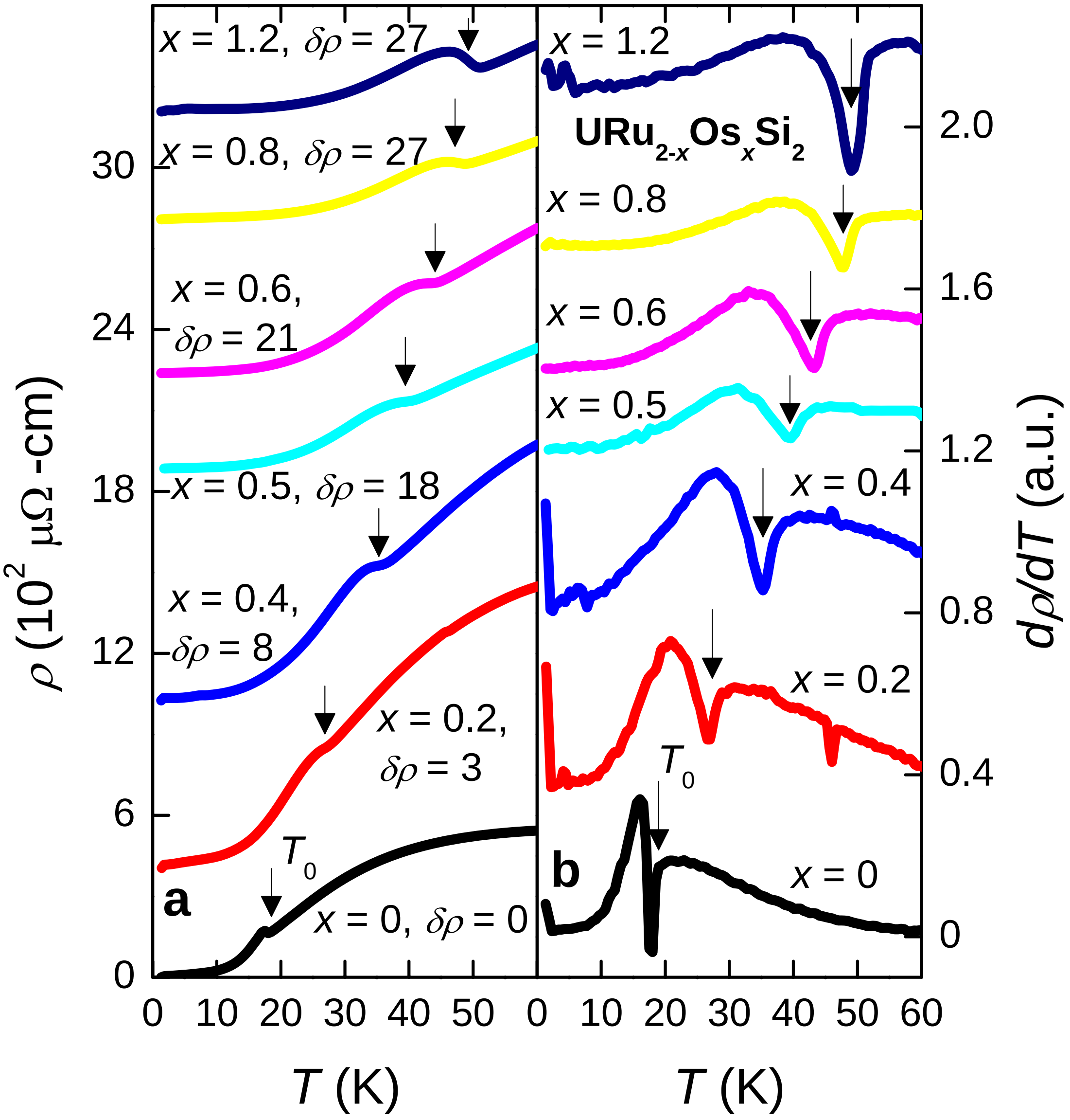

Figure 5.5: (a) Electrical resistivity ρ vs. temperature T for URu$_{2-x}$Os$_x$Si$_2$. For clarity of presentation, only selected values of x are shown. Each data set is shifted by $\delta\rho$, the values of which are indicated in the figure. (b) Derivative of ρ with respect to T, $d\rho/dT$, vs. T. T_0 marks the transition to the HO phase.

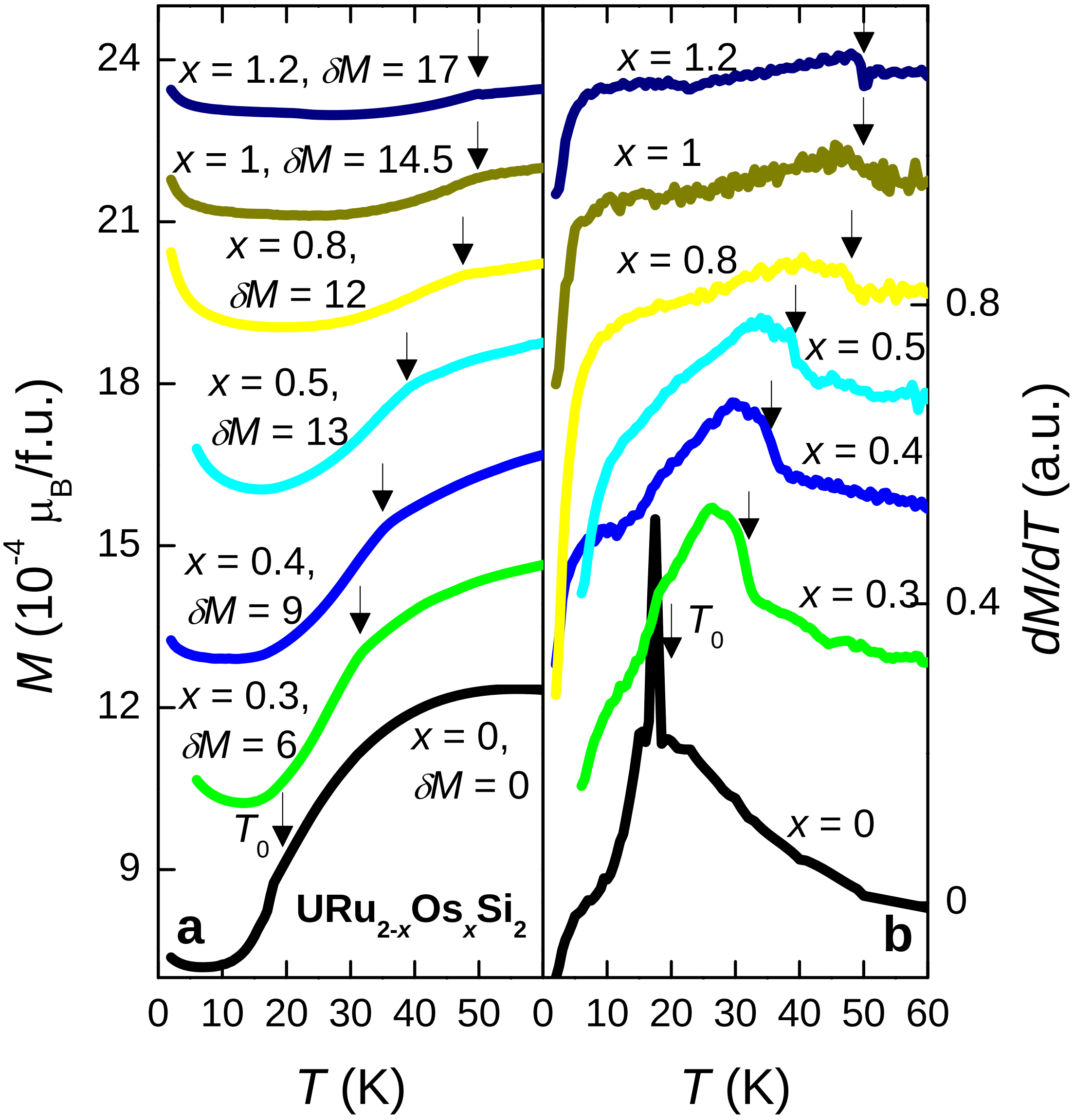

Figure 5.6: (a) Magnetization M vs. temperature T for $\mathrm{URu}_{2-x}\mathrm{Os}_x\mathrm{Si}_2$ in a magnetic field H = 0.1 T. For clarity of presentation, only selected values of x are shown. Each data set is shifted by δM, the values of which are indicated in the figure. (b) Derivative of M with respect to T, dM/dT, vs. T. T_0 is the ordering temperature.

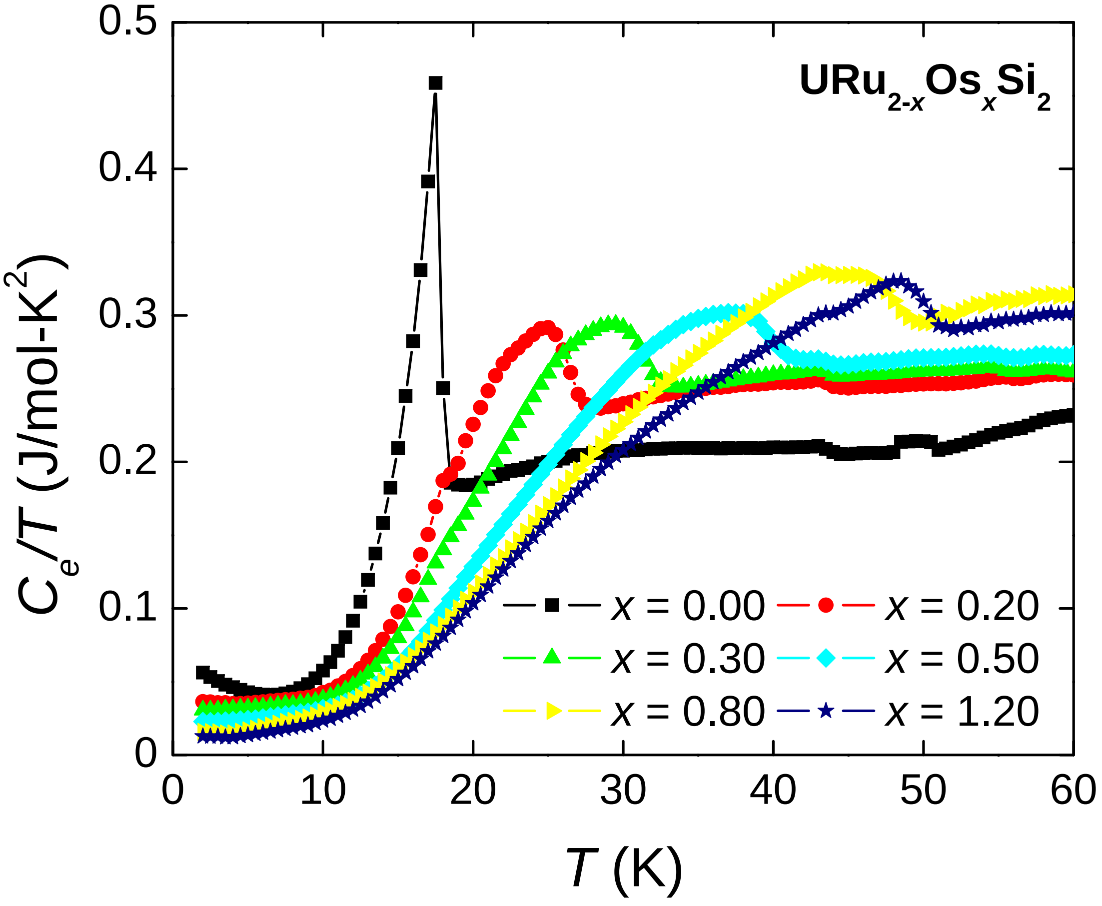

Figure 5.7: Electronic specific heat C_e divided by temperature T vs. T for $URu_{2-x}Os_xSi_2$. For clarity of presentation, only selected values of x are shown.

5.3 Discussion

5.3.1 Phase diagram

In Fig. 5.8, we have summarized the results of the $\rho(T)$, $M(T)$, and $C(T)$ measurements discussed in the previous section in a phase diagram showing the HO transition temperature T_0 vs. Os concentration x. $T_0(x)$ increases with x from 17.5 K at x = 0 to a maximum value of 50 K at $x \approx 1$.

It is interesting to compare the phase diagram with that resulting from a Ge substitution study since Ge ions are larger than Si ions. The phase diagram of URu$_{2-x}$Os$_x$Si$_2$ displays an opposite trend compared to that of URuSi$_{2-x}$Ge$_x$ since the HO transition temperature of URuSi$_{2-x}$Ge$_x$ is suppressed with Ge substitution [97, 103].

5.3.2 Effect of Os substitution on the HO phase

To analyze the effect of Os substitution on the HO phase, the magnitude of the anomaly in the resistivity measurement was studied. Fig. 5.9 displays the height of the resistive anomaly, defined as $\Delta\rho = \rho_2 - \rho_1$, where ρ_1 and ρ_2 are resistivities below and above the transition, respectively. However, errors in measuring the dimensions of resistivity samples might have an impact on $\Delta\rho$. Thus, percent of the magnitude of the jump $\Delta\rho(\%) = 100\frac{\rho_2-\rho_1}{\rho_1}$ was calculated. $\Delta\rho(\%)$ decreases rapidly to a minimum at $x = 0.2$ (Fig. 5.10).

In order to investigate the stabilization of the HO phase by the substitution of Os for Ru, manifested in the increase of T_0 with x, in more detail, we have performed fits of relevant theoretical models to the features in $\rho(T)$ and $C_e(T)$ that characterize the HO phase. The resulting fits of $\rho(T)$ using Eq. 4.2 are shown in Fig. 5.11(a-c). We emphasize that the values for Δ extracted by means of Eq. 4.2 also match with the values for the gap obtained from fits of the low temperature specific heat up to $x \approx 0.4$ (see below and Fig. 5.12). The extracted size of the HO gap decreases moderately with increasing x to a minimum at $x = 0.3$ (Fig. 5.12). This is consistent with the result from URuSi$_{2-x}$Ge$_x$ study where Δ, extracted from a similar method, decreases with Ge substitution [97]. Since for URuSi$_{2-x}$Ge$_x$ samples the HO transition temperature is suppressed as the HO gap is reduced, the decrease of Δ for URu$_{2-x}$Os$_x$Si$_2$ might

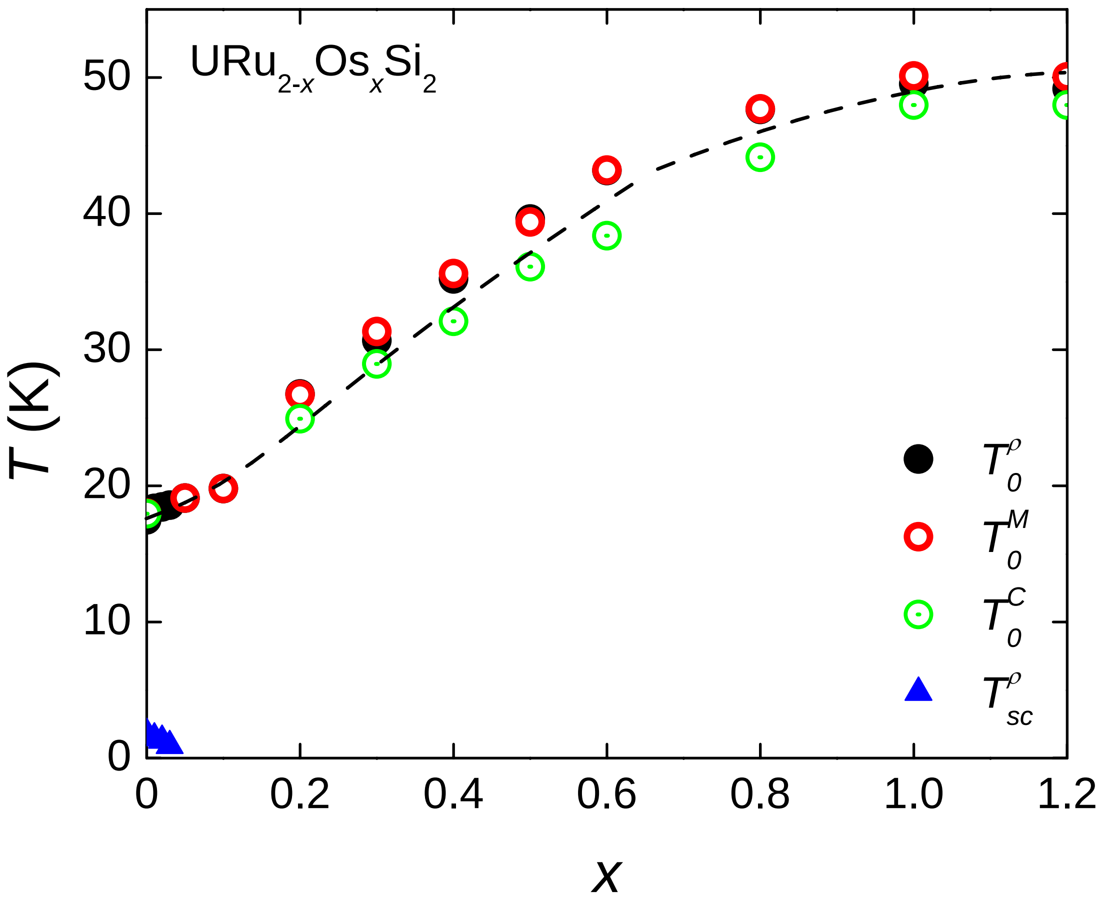

Figure 5.8: Temperature T vs. Os concentration x phase diagram of URu$_{2-x}$Os$_x$Si$_2$, constructed from electrical resistivity (ρ, solid symbols), magnetization (M, empty symbols), and specific heat (C, empty-dotted symbols) measurements. The $T - x$ phase boundary $T_0(x)$ (dashed line) separates the ordered phases (HO and LMAFM) from the paramagnetic phase. The superconducting critical temperature T_{sc} and the transition temperature T_0 from ρ, M, and C are denoted by blue triangles, black, red, and green circles, respectively. Data for samples with $0 < x \leq 0.1$ were taken from [82].

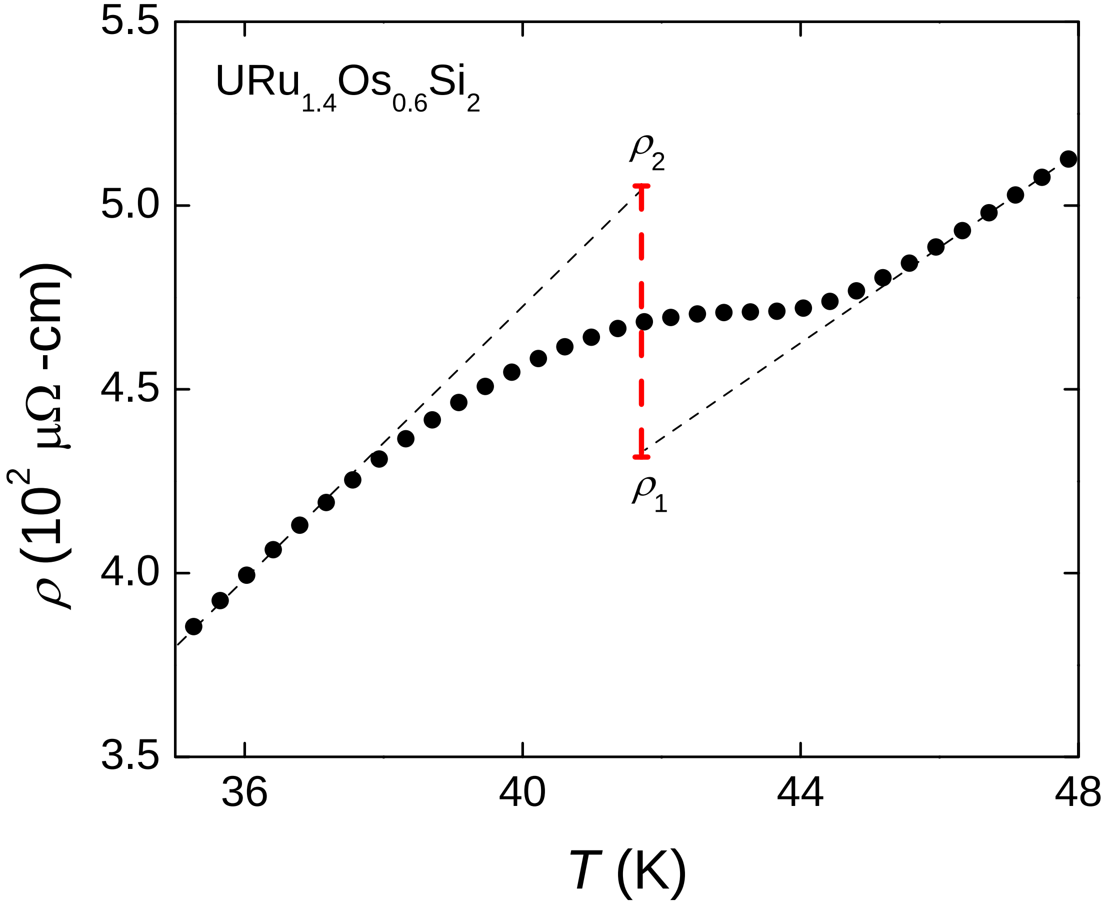

Figure 5.9: Jump or difference in resistivity at the transition for $URu_{1.4}Os_{0.6}Si_2$. ρ_1 and ρ_2 are resistivities above and below the transition, respectively.

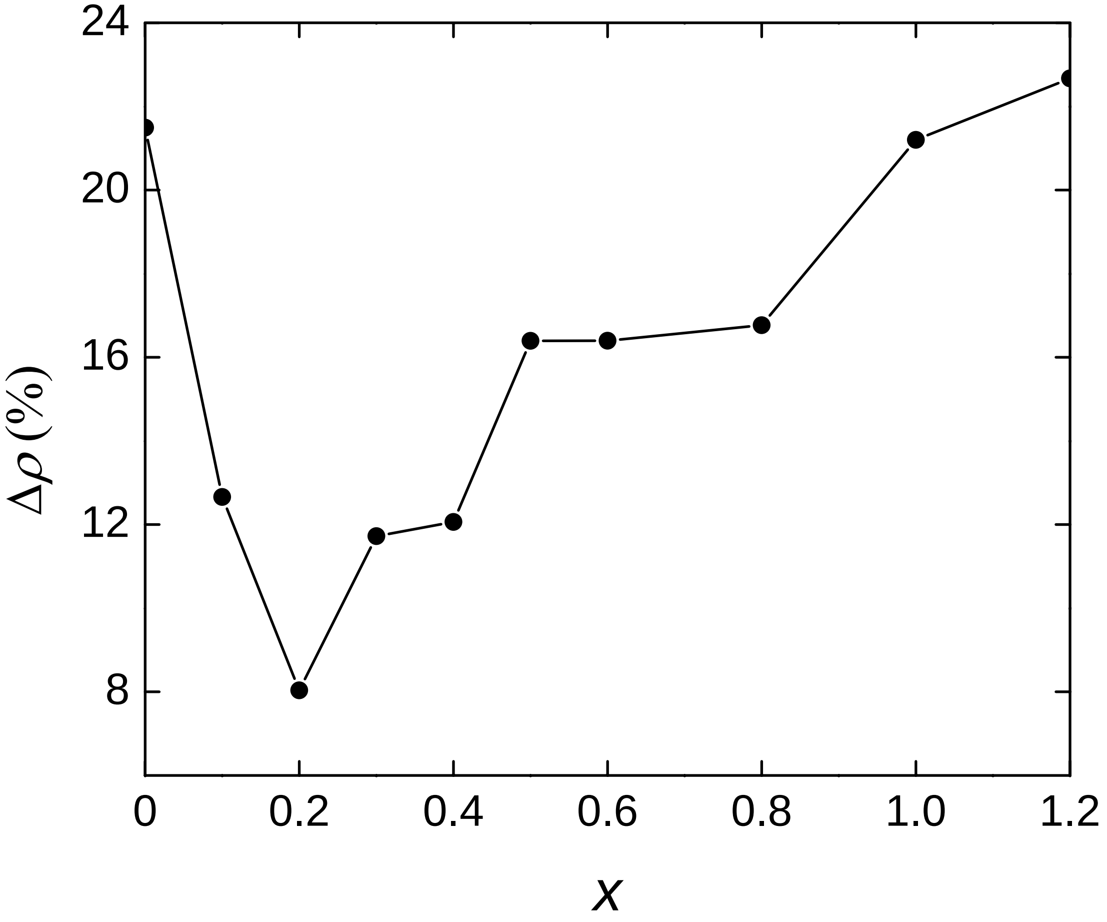

Figure 5.10: Percent of the magnitude of the jump in resistivity at the transition ΔR (see text) vs. Os concentration x for $\mathrm{URu}_{2-x}\mathrm{Os}_x\mathrm{Si}_2$. Data at $x = 0.1$ was taken from [82].

also be interpreted as a suppression of the HO phase. In other words, with increasing x the samples evolve from the HO phase to another ordered phase. Neutron diffraction measurements are required to confirm this. However, if there is a phase transition, then it is possible that the transition is from the HO phase to LMAFM phase since LMAFM phase is believed to be a result of increasing the c/a ratio beyond a critical value [100], and as can be seen from Fig. 5.3, the the c/a ratio increases with Os concentration x. For samples with higher concentrations, the constant and quadratic term of Eq. 4.2 becomes more dominant than the exponential term. Thus, Δ extracted by fitting Eq. 4.2 with electrical resistivity is reliable up to $x \approx\ 0.4$.

Below the HO transition, the $C_e(T)$ data can be described by Eq. 4.3. The fits of Eq. 4.3 to the $C_e(T)$ data are displayed in Fig. 5.11(d-f). At the same time, the jump in C_e at the transition to the HO phase divided by T_0 (Fig. 5.13) plummets with the smallest amount of Os substitution. In order to approximate the fraction of the FS that is gapped, we have estimated the electronic specific-heat coefficient γ_n by linearly extrapolating C_e/T from above T_0 to $T = 0$, and, accordingly, γ_0 for the gapped FS by linearly extrapolating the C_e/T data from below the transition to $T = 0$, following the method described in [18]. In Fig. 5.14, both γ_n and γ_0 are compared to γ_{e^-} for the ungapped state, calculated for conduction electrons with the free electron mass. At $x = 0$, we find that 65% of the FS is gapped, which is slightly larger than the value previously reported [18]. With increasing x, γ_n increases, whereas γ_0 decreases, leading to an increase of the fraction of the FS that is gapped, which at $x = 0.2$ reaches a value of 0.85, and slowly increases at higher x (Fig. 5.15).

5.4 Conclusions

In conclusion, the phase diagram for URu$_{2-x}$Os$_x$Si$_2$ over the range of Os compositions from x = 0 to 1.2 has been established (Fig. 5.8). Interestingly, T_0 is enhanced from 17.5 K at $x = 0$ to 50 K at $x = 1$. Both the electrical resistivity and the specific heat analysis demonstrate that the samples might be evolving from the HO phase to another ordered phase as indicated by the decreasing size of the HO gap. However, in the experiments reported herein, it was not possible to confirm or obtain more information on this

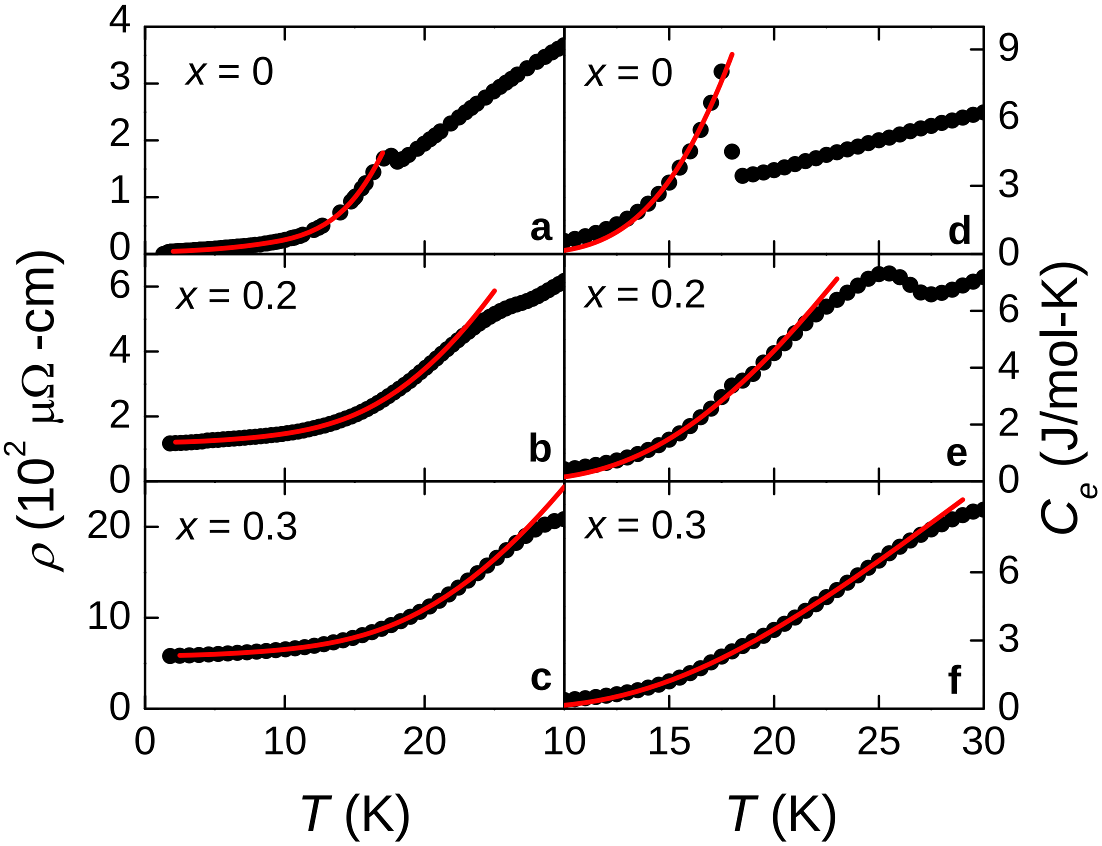

Figure 5.11: Fits of the low temperature electrical resistivity $\rho(T)$ and electronic specific heat $C_e(T)$ to a theoretical model with gapped magnetic excitations (see text) for several Os concentrations x. In the HO phase, the $\rho(T)$ data (a-c) have been fitted using Eq. 4.2 whereas the $C_e(T)$ data (d-f) have been fitted using Eq. 4.3. Black circles represent the data, red solid lines the resulting fits.

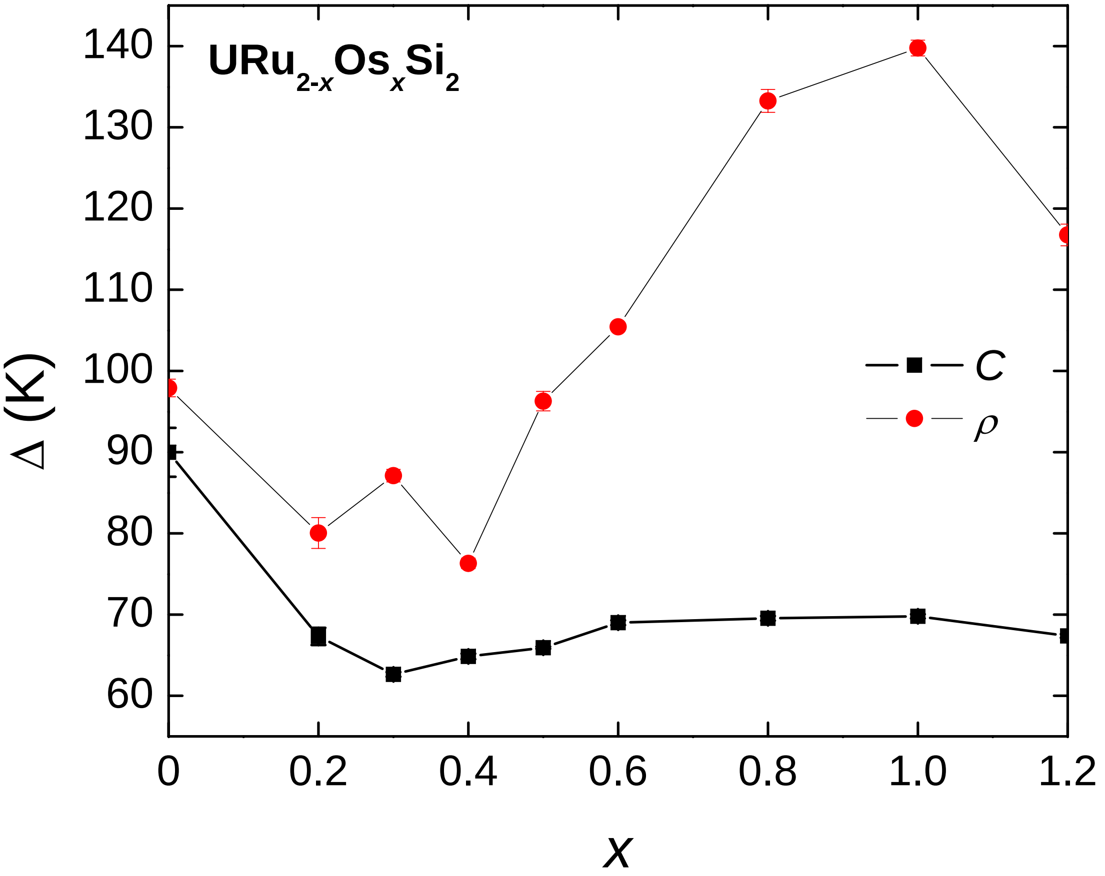

Figure 5.12: Energy gap Δ that opens on the FS due to the onset of the hidden order (HO) phase as determined via fits to the low temperature electrical resistivity $\rho(T)$ (red circles corresponding to a theoretical model with gapped antiferromagnetic excitations; see text) and electronic specific heat $C_e(T)$ (black squares), vs. x (see text and Fig. 5.11).

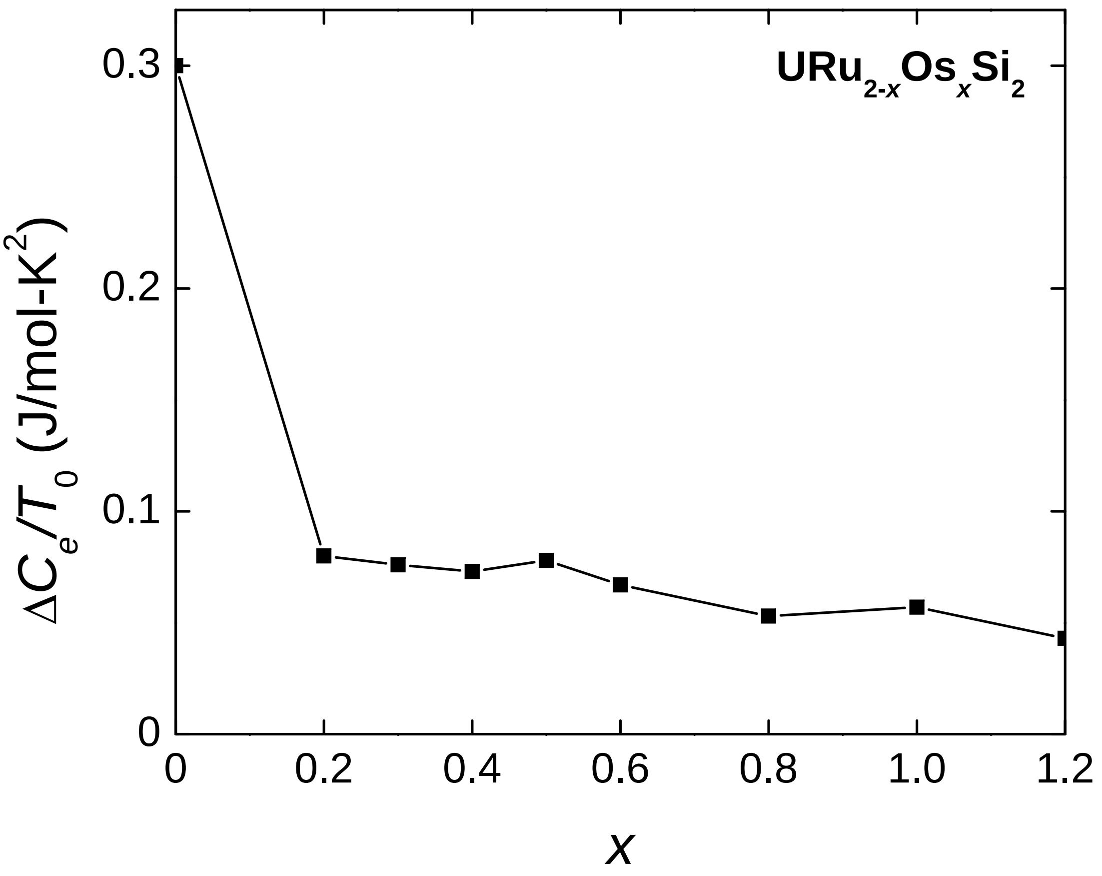

Figure 5.13: Jump in C_e at the transition to the hidden order (HO) phase divided by T_0, $\Delta C_e/T_0$, vs. Os concentration x.

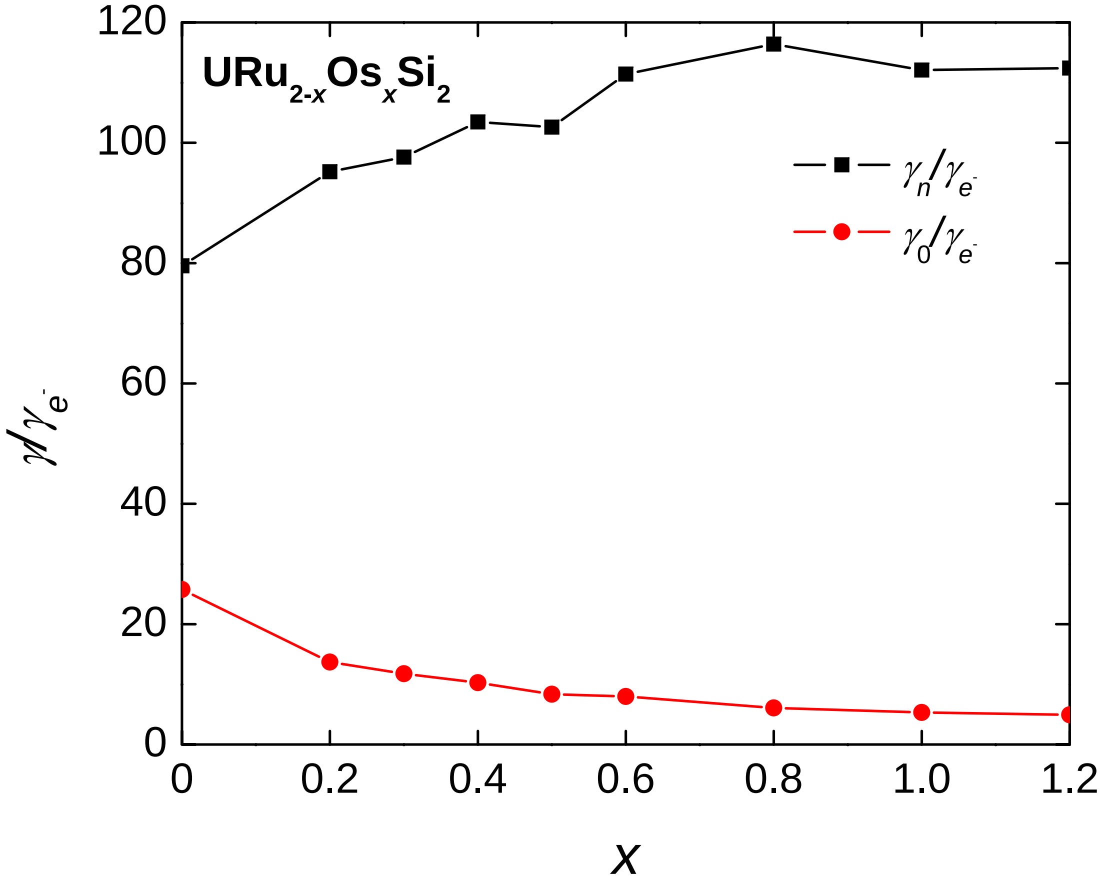

Figure 5.14: Ratio of measured and calculated free electronic specific-heat coefficients γ and γ_{e^-} vs. x for normal phase (γ_n/γ_{e^-}) and hidden order phase (γ_0/γ_{e^-}), respectively.

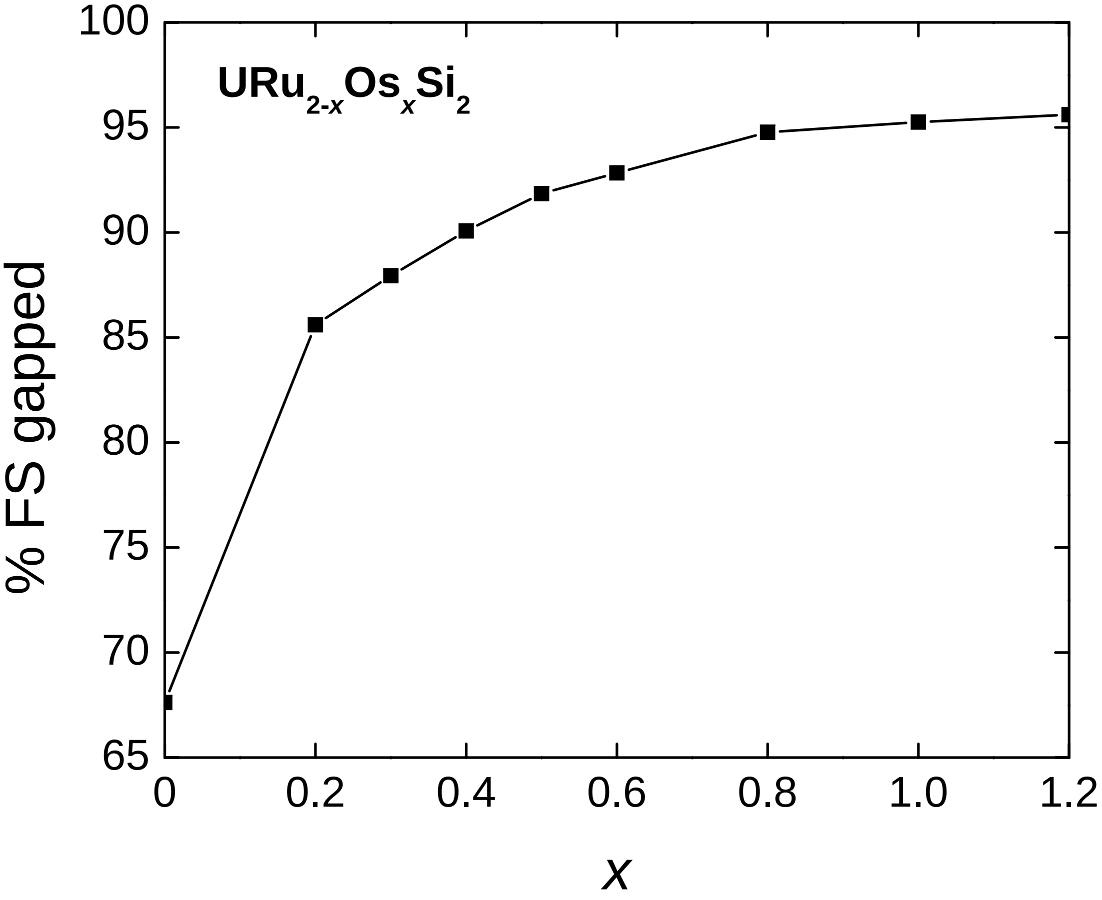

Figure 5.15: Fraction of the FS that is gapped below the HO transition vs. x.

matter. This will require neutron diffraction measurements that are able to determine the magnetic structure and ordered magnetic moment as a function of Os concentration x.

A portion of the text and data presented in this chapter are reprints of material that appears in “Enhancement of hidden order transition temperature in the $URu_{2-x}Os_xSi_2$ system”, N. Kanchanavatee and M. B. Maple in preparation. The dissertation author is the first author of the article.

Bibliography

[1] J. M. Wills and O. Eriksson, *Los Alamos Sci.* **26**, 129 (2000).

[2] A. M. Boring and J. L. Smith, *Los Alamos Sci.* **26**, 90 (2000).

[3] R. C. Albers, *Nature* **410**, 759, 761 (2001).

[4] K. T. Moore and G. v. d. Laan, *Rev. Mod. Phys.* **81**, 235 (2009).

[5] P. Santini, R. Lemanski, and P. Erdos, *Adv. Phys.* **48**, 537 (1999).

[6] J. L. Smith and E. A. Kmetko, *J. Less Common Met.* **90**, 83 (1983).

[7] J. A. Mydosh and P. M. Oppeneer, *Rev. Mod. Phys.* **83**, 1301 (2011).

[8] J. Kondo, *Prog. Theor. Phys.* **32**, 37 (1964).

[9] K. G. Wilson, *Rev. Mod. Phys.* **47**, 773 (1975).

[10] K. Kadowaki and S. B. Woods, *Solid State Commun.* **58**, 507 (1986).

[11] H. K. Onnes, *Electrician* **67**, 657 (1911).

[12] J. File and R. G. Mills, *Phys. Rev. Lett.* **10**, 93 (1963).

[13] D. M. Ginsberg, *Am. J. Phys.* **30**, 433 (1962).

[14] J. Bardeen, L. N. Cooper, and J. R. Schrieffer, *Phys. Rev.* **108**, 1175 (1957).

[15] F. Steglich, J. Aarts, C. D. Bredl, W. Lieke, D. Meschede, W. Franz, and H. Schäfer, *Phys. Rev. Lett.* **43**, 1892 (1979).

[16] C. Pfleiderer, *Rev. Mod. Phys.* **81**, 1551 (2009).

[17] T. T. M. Palstra, A. A. Menovsky, J. V. d. Berg, A. J. Dirkmaat, P. H. Kes, G. J. Nieuwenhuys, and J. A. Mydosh, *Phys. Rev. Lett.* **55**, 2727 (1985).

[18] M. B. MAPLE, J. W. CHEN, Y. DALICHAOUCH, T. KOHARA, C. ROSSEL, M. S. TORIKACHVILI, M. W. MCELFRESH, and J. D. THOMPSON, *Phys. Rev. Lett.* **56**, 185 (1986).

[19] W. SCHLABITZ, J. BAUMANN, B. POLLIT, U. RAUCHSCHWALBE, H. M. MAYER, U. AHLHEIM, and C. D. BREDL, *Z. Phys. B Condens. Matter* **62**, 171 (1986).

[20] C. BROHOLM, J. K. KJEMS, W. J. L. BUYERS, P. MATTHEWS, T. T. M. PALSTRA, A. A. MENOVSKY, and J. A. MYDOSH, *Phys. Rev. Lett.* **58**, 1467 (1987).

[21] P. G. NIKLOWITZ, C. PFLEIDERER, T. KELLER, M. VOJTA, Y. K. HUANG, and J. A. MYDOSH, *Phys. Rev. Lett.* **104**, 106406/1 (2010).

[22] A. D. VISSER, F. E. KAYZEL, A. A. MENOVSKY, J. J. M. FRANSE, J. V. DEN BERG, and G. J. NIEUWENHUYS, *Phys. Rev. B* **34**, 8168 (1986).

[23] H. AMITSUKA, M. SATO, N. METOKI, M. YOKOYAMA, K. KUWAHARA, T. SAKAKIBARA, H. MORIMOTO, S. KAWARAZAKI, Y. MIYAKO, and J. A. MYDOSH, *Phys. Rev. Lett.* **83**, 5114 (1999).

[24] D. A. BONN, J. D. GARRETT, and T. TIMUSK, *Phys. Rev. Lett.* **61**, 1305 (1988).

[25] K. HASSELBACH, J. R. KIRTLEY, and P. LEJAY, *Physica B* **186-188**, 201 (1993).

[26] R. ESCUDERO, F. MORALES, and P. LEJAY, *Phys. Rev. B* **49**, 15271 (1994).

[27] J. G. RODRIGO, F. GUINEA, S. VIEIRA, and F. G. ALIEV, *Phys. Rev. B* **55**, 14318 (1997).

[28] F. MORALES and R. ESCUDERO, *J. Low Temp. Phys.* **154**, 68 (2009).

[29] K. BEHNIA, R. BEL, Y. KASAHARA, Y. NAKAJIMA, H. JIN, H. AUBIN, K. IZAWA, Y. MATSUDA, J. FLOUQUET, Y. HAGA, Y. ONUKI, and P. LEJAY, *Phys. Rev. Lett.* **94**, 156405/1 (2005).

[30] P. A. SHARMA, N. HARRISON, M. JAIME, Y. S. OH, K. H. KIM, C. D. BATISTA, H. AMITSUKA, and J. A. MYDOSH, *Phys. Rev. Lett.* **97**, 156401/1 (2006).

[31] H. OHKUNI, Y. INADA, Y. TOKIWA, K. SAKURA, R. SETTAI, T. HONMA, Y. HAGAS, E. YAMAMOTO, Y. ONUKI, H. YAMAGAMI, S. TAKAHASHI, and T. YANAGISAWA, *Philos. Mag. B* **79**, 1045 (1999).

[32] H. Shishido, K. Hashimoto, T. Shibauchi, T. Sasaki, H. Oizumi, N. Kobayashi, T. Takamasu, K. Takehana, Y. Imanaka, T. D. Matsuda, Y. Haga, Y. Onuki, and Y. Matsuda, *Phys. Rev. Lett.* **102**, 156403/1 (2009).

[33] M. M. Altarawneh, N. Harrison, S. E. Sebastian, L. Balicas, P. H. Tobash, J. D. Thompson, F. Ronning, and E. D. Bauer, *Phys. Rev. Lett.* **106**, 146403 (2011).

[34] H. M. Rietveld, *J. Appl. Crystallogr.* **2**, 65 (1969).

[35] A. Larson and R. V. Dreele, *Los Alamos Natl. Lab. Rep.* , 86 (2000).

[36] W. A. Fertig, D. C. Johnston, L. E. DeLong, R. W. McCallum, M. B. Maple, and B. T. Matthias, *Phys. Rev. Lett.* **38**, 987 (1977).

[37] D. E. Moncton, D. B. McWhan, J. Eckert, G. Shirane, and W. Thomlinson, *Phys. Rev. Lett.* **39**, 1164 (1977).

[38] S. K. Sinha, G. W. Crabtree, D. G. Hinks, and H. Mook, *Phys. Rev. Lett.* **48**, 950 (1982).

[39] M. Ishikawa and . Fischer, *Solid State Commun.* **24**, 747 (1977).

[40] J. W. Lynn, G. Shirane, W. Thomlinson, and R. N. Shelton, *Phys. Rev. Lett.* **46**, 368 (1981).

[41] M. B. Maple, R. E. Baumbach, J. J. Hamlin, D. A. Zocco, B. J. Taylor, N. P. Butch, J. R. Jeffries, S. T. Weir, B. C. Sales, D. Mandrus, M. A. McGuire, A. S. Sefat, R. Jin, Y. K. Vohra, J. H. Chu, and I. R. Fisher, *Physica B* **404**, 2924 (2009).

[42] N. T. Huy, A. Gasparini, D. E. D. Nijs, Y. Huang, J. C. P. Klaasse, T. Gortenmulder, A. D. Visser, A. Hamann, T. Goerlach, and H. V. Loehneysen, *Phys. Rev. Lett.* **99**, 067006/1 (2007).

[43] S. S. Saxena, P. Agarwal, K. Ahilan, F. M. Grosche, R. K. W. Haselwimmer, M. J. Steiner, E. Pugh, I. R. Walker, S. R. Julian, P. Monthoux, G. G. Lonzarich, A. Huxley, I. Sheikin, D. Braithwaite, and J. Flouquet, *Nature* **406**, 587 (2000).

[44] T. Akazawa, H. Hidaka, T. Fujiwara, T. C. Kobayashi, E. Yamamoto, Y. Haga, R. Settai, and Y. Ōnuki, *J. Phys. Condens. Matter* **16**, L29 (2004).

[45] D. Aoki, A. Huxley, E. Ressouche, D. Braithwaite, J. Flouquet, J.-P. Brison, E. Lhotel, and C. Paulsen, *Nature* **413**, 613 (2001).

[46] N. F. Berk and J. R. Schrieffer, *Phys. Rev. Lett.* **17**, 433 (1966).

[47] D. E. D. NIJS, N. T. HUY, and A. D. VISSER, *Phys. Rev. B* **77**, 140506/1 (2008).

[48] N. T. HUY and A. D. VISSER, *Solid State Commun.* **149**, 703 (2009).

[49] E. HASSINGER, D. AOKI, G. KNEBEL, and J. FLOUQUET, *J. Phys. Soc. Jpn.* **77**, 073703/1 (2008).

[50] E. SLOOTEN, T. NAKA, A. GASPARINI, Y. K. HUANG, and A. DE VISSER, *Phys. Rev. Lett.* **103**, 097003/1 (2009).

[51] J. POSPISIL, J. P. VEJPRAVOVA, M. DIVIS, and V. SECHOVSKY, *J. Appl. Phys.* **105**, 07E114/1 (2009).

[52] F. CANEPA, P. MANFRINETTI, M. PANI, and A. PALENZONA, *J. Alloys Compd.* **234**, 225 (1996).

[53] V. SECHOVSKY, L. HAVELA, A. PURWANTO, A. C. LARSON, R. A. ROBINSON, K. PROKES, H. NAKOTTE, E. BRÜCK, F. R. D. BOER, P. SVOBODA, H. MALETTA, and M. WINKELMANN, *J. Alloys Compd.* **213–214**, 536 (1994).

[54] I. H. HAGMUSA, J. C. P. KLAASSE, E. BRUCK, K. PROKES, B. F. R. DE, and H. NAKOTTE, *J. Appl. Phys.* **81**, 4157 (1997).

[55] N. T. HUY, D. E. DE NIJS, Y. K. HUANG, and A. DE VISSER, *Phys. Rev. Lett.* **100**, 077002/1 (2008).

[56] A. ARROTT, *Phys. Rev.* **108**, 1394 (1957).

[57] S. BLUNDELL, Oxford university press, 2007.

[58] P. RHODES and E. P. WOHLFARTH, *Proc. R. Soc. London, Ser. A* **273**, 247 (1963).

[59] E. P. WOHLFARTH, *Physica B+C* **91**, 305 (1977).

[60] M. B. BRODSKY, *Rep. Prog. Phys* **41**, 1547 (1978).

[61] M. B. MAPLE, R. E. BAUMBACH, N. P. BUTCH, J. J. HAMLIN, and M. JANOSCHEK, *J. Low Temp. Phys.* **161**, 4 (2010).

[62] B. LUETHI, B. WOLF, P. THALMEIER, M. GUENTHER, W. SIXL, and G. BRULS, *Phys. Lett. A* **175**, 237 (1993).

[63] Y. DUBI and A. V. BALATSKY, *Phys. Rev. Lett.* **106**, 086401 (2011).

[64] P. CHANDRA, P. COLEMAN, J. A. MYDOSH, and V. TRIPATHI, *Nature* **417**, 831 (2002).

[65] P. SANTINI, *Phys. Rev. B* **57**, 5191 (1998).

[66] T. Kasuya, *J. Phys. Soc. Jpn.* **66**, 3348 (1997).

[67] A. E. Sikkema, W. J. L. Buyers, I. Affleck, and J. Gan, *Phys. Rev. B* **54**, 9322 (1996).

[68] F. Cricchio, F. Bultmark, O. Graanaes, and L. Nordstroem, *Phys. Rev. Lett.* **103**, 107202/1 (2009).

[69] K. Haule and G. Kotliar, *Nat. Phys.* **5**, 796 (2009).

[70] H. Ikeda and Y. Ohashi, *Phys. Rev. Lett.* **81**, 3723 (1998).

[71] C. M. Varma and L. Zhu, *Phys. Rev. Lett.* **96**, 036405/1 (2006).

[72] S. Elgazzar, J. Rusz, M. Amft, P. M. Oppeneer, and J. A. Mydosh, *Nat. Mater.* **8**, 337 (2009).

[73] H. Harima, K. Miyake, and J. Flouquet, *J. Phys. Soc. Jpn.* **79**, 033705/1 (2010).

[74] A. V. Balatsky, A. Chantis, H. P. Dahal, D. Parker, and J. X. Zhu, *Phys. Rev. B* **79**, 214413/1 (2009).

[75] A. F. Santander-Syro, M. Klein, F. L. Boariu, A. Nuber, P. Lejay, and F. Reinert, *Nat. Phys.* **5**, 637 (2009).

[76] A. R. Schmidt, M. H. Hamidian, P. Wahl, F. Meier, A. V. Balatsky, J. D. Garrett, T. J. Williams, G. M. Luke, and J. C. Davis, *Nature* **465**, 570 (2010).

[77] P. Aynajian, E. H. d. S. Neto, C. V. Parker, Y. Huang, A. Pasupathy, J. A. Mydosh, and A. Yazdani, *Proc. Natl. Acad. Sci. U. S. A.* **107**, 10383 (2010).

[78] C. Pépin, M. R. Norman, S. Burdin, and A. Ferraz, *Phys. Rev. Lett.* **106**, 106601 (2011).

[79] G. Motoyama, N. Yokoyama, A. Sumiyama, and Y. Oda, *J. Phys. Soc. Jpn.* **77**, 123710/1 (2008).

[80] R. Okazaki, M. Shimozawa, H. Shishido, M. Konczykowski, Y. Haga, T. D. Matsuda, E. Yamamoto, Y. Onuki, Y. Yanase, T. Shibauchi, and Y. Matsuda, *J. Phys. Soc. Jpn.* **79**, 084705/1 (2010).

[81] K. H. Kim, N. Harrison, M. Jaime, G. S. Boebinger, and J. A. Mydosh, *Phys. Rev. Lett.* **91**, 256401/1 (2003).

[82] Y. Dalichaouch, M. B. Maple, J. W. Chen, T. Kohara, C. Rossel, M. S. Torikachvili, and A. L. Giorgi, *Phys. Rev. B* **41**, 1829 (1990).

[83] M. Yokoyama, H. Amitsuka, S. Itoh, I. Kawasaki, K. Tenya, and H. Yoshizawa, *J. Phys. Soc. Jpn.* **73**, 545 (2004).

[84] Y. Dalichaouch, M. B. Maple, M. S. Torikachvili, and A. L. Giorgi, *Phys. Rev. B* **39**, 2423 (1989).

[85] Y. Dalichaouch, M. B. Maple, R. P. Guertin, M. V. Kuric, M. S. Torikachvili, and A. L. Giorgi, *Physica B* **163**, 113 (1990).

[86] E. D. Bauer, V. S. Zapf, P.-C. Ho, N. P. Butch, E. J. Freeman, C. Sirvent, and M. B. Maple, *Phys. Rev. Lett.* **94**, 046401 (2005).

[87] N. P. Butch and M. B. Maple, *Phys. Rev. Lett.* **103**, 076404 (2009).

[88] A. Szytula, M. Slaski, B. Dunlap, Z. Sungaila, and A. Umezawa, *J. Magn. Magn. Mater.* **75**, 71 (1988).

[89] N. P. Butch, J. R. Jeffries, S. Chi, J. B. L. ao, J. W. Lynn, and M. B. Maple, *Phys. Rev. B* **82**, 060408/1 (2010).

[90] K. Kuwahara, H. Sagayama, K. Iwasa, M. Kohgi, S. Miyazaki, J. Nozaki, J. Nogami, M. Yokoyama, H. Amitsuka, H. Nakao, and Y. Murakami, *Acta Phys. Pol., B* **34**, 4307 (2003).

[91] H. Luo, S. Dabos, U. Benedict, and J. C. Spirlet, *J. Less Common Met.* **142**, L23 (1988).

[92] B. Wolf, W. Sixl, R. Graf, D. Finsterbusch, G. Bruls, B. Luthi, E. A. Knetsch, A. A. Menovsky, and J. A. Mydosh, *J. Low Temp. Phys.* **94**, 307 (1994).

[93] K. Iki, G. Oomi, Y. Uwatoko, H. Takahashi, N. Mori, Y. Onuki, and T. Komatsubara, *J. Alloys Compd.* **181**, 71 (1992).

[94] R. Jaramillo, Y. Feng, J. Wang, and T. F. Rosenbaum, *Proc. Natl. Acad. Sci. U. S. A.* **107**, 13631 (2010).

[95] T. T. M. Palstra, A. A. Menovsky, and J. A. Mydosh, *Phys. Rev. B* **33**, 6527 (1986).

[96] E. Louis, A. D. Visser, A. Menovsky, and J. J. M. Franse, *Physica B+C* **144**, 48 (1986).

[97] J. G. Park and B. R. Coles, *J. Phys. Condens. Matter* **6**, 1425 (1994).

[98] N. H. Andersen and H. Smith, *Phys. Rev. B* **19**, 384 (1979).

[99] M. B. Fontes, J. C. Trochez, B. Giordanengo, S. L. Bud'ko, D. R. Sanchez, E. M. Baggio-Saitovitch, and M. A. Continentino, *Phys. Rev. B* **60**, 6781 (1999).

[100] M. Yokoyama, H. Amitsuka, K. Tenya, K. Watanabe, S. Kawarazaki, H. Yoshizawa, and J. A. Mydosh, *Phys. Rev. B* **72**, 214419/1 (2005).

[101] N. Kanchanavatee, M. Janoschek, R. E. Baumbach, J. J. Hamlin, D. A. Zocco, K. Huang, and M. B. Maple, *Phys. Rev. B* **84**, 245122 (2011).

[102] T. T. M. Palstra, A. A. Menovsky, G. J. Nieuwenhuys, and J. A. Mydosh, *J. Magn. Magn. Mater.* **54-57**, 435 (1986).

[103] S. K. Dhar, R. J. Begum, P. Raj, P. Suryanarayana, L. C. Gupta, and R. Vijayaraghavan, *Solid State Commun.* **83**, 965 (1992).